

**Berichte**  
zur Polarforschung

???  
1999

**Reports**  
on Polar Research



**Arctic Radiation and Turbulence Interaction Study**  
*(ARTIST)*

---

**Jörg Hartmann, Frank Albers, Stefania Argentini,  
Axel Bochert, Ubaldo Bonafé, Wolfgang Cohrs,  
Alessandro Conidi, Dietmar Freese,  
Teodoro Georgiadis, Alessandro Ippoliti,  
Lars Kaleschke, Christof Lüpkes, Uwe Maixner,  
Giangiuseppe Mastrantonio, Fabrizio Ravegnani,  
Andreas Reuter, Giuliano Trivellone, Angelo Viola**

Axel Bochert  
Wolfgang Cohrs  
Dietmar Freese  
Jörg Hartmann  
Christof Lüpkes  
Alfred-Wegener-Institut für Polar- und Meeresforschung  
Columbusstraße  
D-27570 Bremerhaven

Frank Albers  
Uwe Maixner  
Andreas Reuter  
GKSS Forschungszentrum Geesthacht GmbH  
Max-Planck-Straße D-21502 Geestacht

Lars Kaleschke  
Institut für Umweltphysik  
Universität Bremen

Stefania Argentini  
Alessandro Conidi  
Giangiuseppe Mastrantonio  
Angelo Viola  
Istituto di Fisica dell' Atmosfera  
Area di Ricerca di Tor Vergata  
Via Fosso del Cavaliere, 100  
00033 Roma-Italy

Alessandro Ippoliti  
Istituto di Struttura della Materia  
Area di Ricerca di Tor Vergata  
Via Fosso del Cavaliere, 100  
00033 Roma-Italy

Ubaldo Bonafé  
Teodoro Georgiadis  
Fabrizio Ravegnani  
Giuliano Trivellone  
Istituto per lo Studio della Fisica e della Chimica della Bassa ed Alta Atmosfera  
Via Gobetti, 101  
40129 Bologna-Italy

# Contents

<b>Abstract</b>	<b>iii</b>
<b>1 Scientific Objectives</b>	<b>1</b>
1.1 Convection over polar ocean surfaces . . . . .	1
1.2 Stratus and stratocumulus clouds over sea ice . . . . .	1
1.3 Turbulent fluxes over rough sea ice . . . . .	2
1.4 Boundary layer measurements at Ny-Ålesund . . . . .	2
1.5 Remote sensing of sea ice . . . . .	3
<b>2 Instrumentation and Observational Procedures</b>	<b>4</b>
2.1 Aircraft instruments . . . . .	4
2.2 Equipment for microphysical measurements . . . . .	5
2.3 Nevzorov LWC/TWC probe . . . . .	5
2.4 Ozone analysers . . . . .	6
2.5 Microwave radiometers . . . . .	6
2.6 Color Line Scanner on Polar2 . . . . .	7
2.7 Line Scanners on Polar 4 . . . . .	7
2.8 Aircraft mission types . . . . .	8
2.9 Site and instrumentation at Ny-Ålesund . . . . .	9
2.10 Sodar . . . . .	9
2.11 Tethersonde . . . . .	11
2.12 Surface radiation sensors . . . . .	12
2.13 Surface turbulence equipment . . . . .	12
2.14 Drifting buoys . . . . .	12

<b>3</b>	<b>Measurement Inventory</b>	<b>13</b>
3.1	Satellite data . . . . .	13
3.2	Airborne missions . . . . .	15
3.3	Ground based measurements at Ny-Ålesund . . . . .	50
<b>4</b>	<b>Examples of Measurements and Preliminary Results</b>	<b>53</b>
4.1	Surface pressure and temperature from drifting buoys . . . . .	53
4.2	Validation of radiation measurements . . . . .	57
4.3	Convective cell structure, 8 April 1998 . . . . .	59
4.4	Cold air outbreak, 4 April 1998 . . . . .	60
4.5	Cloud particles, 4 April 1998 . . . . .	63
4.6	On-ice flow, 27 March 1998 . . . . .	67
4.7	Microwave remote sensing of sea ice, 30 March 1998 . . . . .	71
4.8	Low-level atmospheric structure and surface radiation at Ny-Ålesund	74
<b>5</b>	<b>References</b>	<b>80</b>
<b>6</b>	<b>Acknowledgements</b>	<b>81</b>

## Abstract

The joint research project ARTIST (Arctic Radiation and Turbulence Interaction Study) is conducted by the Alfred Wegener Institute for Polar and Marine Research, the GKSS Research Centre (GKSS), the Institute for Environmental Physics at the University of Bremen (IUP), the Finnish Institute of Marine Research (FIMR), the University of Helsinki, the Istituto di Fisica dell'Atmosfera (IFA) and the Istituto per lo Studio della Fisica e Chimica della Bassa ed Alta Atmosfera (FISBAT). The study is supported by funds of the participating institutions and of the "Environment and Climate" programme of the European Commission.

An extensive field programme was conducted in March and April 1998 with ground based and airborne measurements in the Arctic area around Svalbard. Airborne measurements were performed with the research aircraft (Polar 2 and Polar 4) of AWI. Ground based measurements were conducted in Ny-Ålesund. Satellite data (AVHRR, passive and active microwave data) have been acquired to derive the cloud cover, sea ice extent and concentration and the surface radiation balance for the Atlantic sector of the Arctic Ocean.

The campaign provides measurements to investigate the effect of clouds and sea ice on the thermodynamic and kinematic structure of the atmospheric boundary layer and on the exchange processes at the marine and terrestrial Earth surfaces.

This report outlines the scientific objectives and presents a catalogue of the measurements and some examples of the observational results.



## 1. Scientific Objectives

Low level clouds and Arctic Haze have a significant impact on the energy balance at the Earth's surface and on the thermodynamic structure of the atmospheric boundary layer. This cloud influence is strongly dependent on the radiative conditions of the Earth's Surface, which differ remarkably for water, sea ice or bare soil. Therefore, a comprehensive study of the cloud effects must be accompanied by measurements of the radiative, thermal and dynamic surface processes, and the atmospheric turbulent fluxes besides detailed observations of cloud variables.

Measurements and numerical modelling will be carried out to determine the development of the atmospheric boundary layer for different mean atmospheric flow and lower boundary conditions. The aim is to satisfactorily parameterise the surface exchanges and the vertical fluxes of radiation, sensible and latent heat, as well as horizontal momentum in the lower atmosphere, with particular attention to the influence of clouds.

### 1.1. Convection over polar ocean surfaces

When cold polar air, formed over the interior sea ice, flows southwards over the open ocean it is strongly heated and moistened from below. The large input of water vapour leads to the formation of predominately stratocumulus clouds. The accompanying latent heat release enhances the vertical mixing, and thus the growth of the atmospheric boundary layer. Subsequently a substantial cloud layer forms downstream of the ice edge, which interacts with the radiative fluxes and alters the subscale vertical heat, water mass and momentum fluxes.

First attempts to parameterise these fluxes have already been made based on the REFLEX studies. However, those measurements did not cover all relevant flow conditions so that the ARTIST data will be used to fill the existing gaps.

Furthermore, new approaches are made to quantify the interaction between radiation, turbulence and the cloud particle distribution. Of special interest is the investigation of glaciation processes within the clouds as a function of lifetime and fetch.

### 1.2. Stratus and stratocumulus clouds over sea ice

The total extinction in the short wave range caused by a cloud layer mainly depends on the cloud thickness, the type and size distribution of cloud particles and on the albedo of the ice or water surfaces.

Therefore, flight patterns consisted of synchronuous flights of both aircraft above and below clouds, of cloud traverses to record the vertical structure of temperature,

moisture and cloud particle properties, and of horizontal flights inside clouds to determine horizontal inhomogeneities.

This procedure enabled us to measure all quantities required for improvements of radiation transfer concepts for the Arctic atmosphere over open water, snow and sea ice.

### **1.3. Turbulent fluxes over rough sea ice**

Turbulence measurements over the marginal ice zone with relatively small roughness elements are now sufficiently available. But only little information exists from areas with very large roughness. Therefore, two flights were carried out in the east of Svalbard where ridged ice was predominant. During these flights the momentum transfer was measured with the turbulence equipment, and a laser altimeter was used to detect the surface topography with high spatial resolution.

### **1.4. Boundary layer measurements at Ny-Ålesund**

During cold air outbreaks in the Fram Strait region it is often observed that the flow, initially oriented from north to south, turns clockwise over and in the immediate lee of Spitsbergen. This phenomenon may be due to large scale effects, but partially it can be explained by a mesoscale pressure gradient between the cold air over the Spitsbergen area and the warmer air over Fram Strait. The flow field over Spitsbergen is strongly influenced by the complex topography of the Spitsbergen mountains.

To get more insight into the characteristic modification of the flow by the terrain, aircraft and ground based measurements have been carried out in the Kongsfjord region at the western coast of Spitsbergen. The ground based measurements near Ny-Ålesund consisted of measurements of the turbulent fluxes with sonic anemometers and of the radiation balance. Additionally, a Sodar system was used more or less continuously to visualise the density stratification of the atmosphere and the 3-dimensional wind field up to a height of 1000 m. A tether sonde system provided profiles of wind, temperature and humidity, which can be used in conjunction with the Sodar data to get more insight into the structure of the atmospheric flow within the valley. The tether sonde profiles are also helpful for the interpretation of the Sodar data, to identify the inversion height, to understand the stability characteristics of the boundary layer and to compute heat flux profiles.

The radiation balance surface measurements will be used to study the surface partitioning of the incoming solar radiation in the short- and long-wave range. The determination of the different energy amounts in these two bands will be used to characterise the role of cloud types in modulating the energy received at the surface.

The polar aircraft were used to observe the 3-dimensional wind, temperature and humidity field, as well as turbulent fluxes within the valley of Ny-Ålesund and its environment. The data will be used for the initialisation and the validation of mesoscale model studies of the flow, which in turn can be used to generalise the observations for different large scale conditions.

The results of the ARTIST programme in the Ny-Ålesund area will be helpful for numerous other scientific programs carried out in that region. Knowledge of the influence of the orography on the wind and temperature field is especially important for observations of chemical substances.

### **1.5. Remote sensing of sea ice**

For the compilation of sea ice maps, an almost complete coverage of the polar regions with a coarse spatial resolution of about 25 km is provided by the measurements of the Special Sensor Microwave/Imager (SSM/I) on polar orbiting satellites. To test and improve evaluation algorithms of the SSM/I images, we have conducted passive microwave measurements together with line scanner observations in the visible and infrared spectral range on low level flights. Microwave radiometers at 19.35 GHz and 37 GHz were operated in combination with line scanners on Polar 4. The line scanner data are used to determine the concentration, distribution and type of sea ice.

In addition to the passive microwave studies, the aircraft remote sensing data serve also as reference for measurements of the synthetic aperture radar (SAR) onboard the European Remote-Sensing Satellite ERS-2. With the swath limited to 100 km the SAR can be used to analyse test areas, while sensors like SSM/I are more appropriate for large area coverage. The interpretation of the signals measured by both sensors is still difficult due to the sparse ground truth data available so far. The surface data obtained from airborne passive microwave measurements will be used for a better understanding of the signals measured by SSM/I and SAR.

During the campaign, the Danish Center for Remote Sensing conducted 2 airborne missions with a fully polarimetric and interferometric SAR over the sea ice region around Svalbard. The opportunity was taken to arrange our remote sensing missions to coincide with the Danish missions.

## 2. Instrumentation and Observational Procedures

### 2.1. Aircraft instruments

The aircraft were instrumented with well proven devices that have been used successfully in previous campaigns, and with new systems which were operated for the first time during ARTIST. Since the established instrumentation is described in detail elsewhere (User Handbook for the polar aircraft, Kottmeier (ed.), 1996) only a brief listing is given here in Tables 2.1–2.3. The new instrumentation is described in the following.

**Table 2.1:** Instrumentation on **both aircraft**. These instruments have been operated on all flights.

<i>measurement</i>	<i>instrument</i>
temperature	Pt100
humidity	Vaisala Humicap
pressure	Rosemount absolute pressure transducer
airspeed	Rosemount differential pressure transducer
position	GPS and INS
short wave radiation	Eppley pyranometer (up and down)
long wave radiation	Eppley pyrgeometer (up and down)
height	radar altimeter
cloud water content	Nevzorov Probe

**Table 2.2:** Additional instrumentation on **Polar 2**. These instruments have been operated on all flights.

<i>measurement</i>	<i>instrument</i>
turbulence	Meteopod turbulence probe (5-hole probe)
wind vector	Meteopod, GPS, INS
humidity	Lyman-alpha, dew point mirror
sea ice topography	laser altimeter
surface temperature	KT4 radiation thermometer
sea ice concentration	color line scanner

**Table 2.3:** Additional instrumentation on **Polar 4**. Only one set of these instruments has been operated at a time.

<i>measurement</i>	<i>instrument</i>
cloud particles, entrainment, ozone	PMS probes Ozone analysers
microwave radiation, sea ice structure	microwave radiometers visible and infrared line scanners
aerosol	sun photometer

## 2.2. Equipment for microphysical measurements

The investigation of interactions between clouds and radiation constitute an important part of the ARTIST project. For this purpose, intensive microphysical measurements have been made. The GKSS Research Center operated probes and sensors on both aircraft. For the determination of cloud particle properties of the entire size range from 0.1 to 6400  $\mu\text{m}$ , PMS (Particle Measuring Systems INC., Boulder, CO, USA) probes were mounted on Polar 4 as listed in Table 2.4. Nevzorov LWC/TWC probes (SkyTech Research INC., Toronto, CN) had been used

**Table 2.4:** Probes and sensors for particle properties operated by GKSS on Polar 4.

<i>instrument</i>	<i>purpose</i>	<i>size range in <math>\mu\text{m}</math></i>
PMS PCASP-100X	aerosol	0.1–3.0
PMS FSSP-100	cloud particles	2.0–47
OAP-2D-GA2	cloud particles	10–640
OAP-2D2-C	cloud particles	25–800
OAP-2D2-P	precipitation particles	200–6400

for an integral measurement of the liquid water content (LWC) and total water content (TWC) on both aircraft. The ice water content (IWC) can be derived by subtracting the LWC from the TWC. Since ozone concentrations usually have a significant gradient at the top of the boundary layer, two ozone analysers on Polar 4 provided reasonable information on the exchange of cloud and environmental air in the upper cloud layer. The PMS OAP-2D-GA2 (2D-Greyprobe) was supplied by the University of Hamburg (Germany), one of the Nevzorov LWC/TWC probes was supplied by the Max-Planck-Institute for Meteorology (Hamburg, Germany) and the two ozone probes were supplied by the Forschungszentrum Karlsruhe (Karlsruhe, Germany).

## 2.3. Nevzorov LWC/TWC probe

The Nevzorov LWC/TWC probe (IVO-2a), manufactured by SkyTech Research INC (Toronto, CN), is a constant temperature hot wire probe, designed for aircraft use. The probe consists of two separate sensors for measuring the LWC and TWC (liquid plus ice water content) of clouds and fog in the range between 0.003  $\text{gm}^{-3}$  and 3  $\text{gm}^{-3}$ . Both sensors are mounted on a common head aligned parallel to the airflow. Within an airspeed range between 10 m/s and 180 m/s, the errors of the probe are less than 10%. This has been proven by extensive tests in a high speed wind tunnel (Korolev et al., 1998).

The principle of operation is based on the determination of the heat loss of the sensors by evaporation of cloud water and by convective heat losses. Each sensor consists of a collector and a reference winding. The reference winding is shielded

from impacts of cloud particles and therefore allows the direct calculation of the convective heat loss. This is a major improvement compared to other constant temperature hot wire instruments, like the King LWC probe, where assumptions on the convective heat loss of the sensors have to be made during data analysis. The LWC and TWC sensors consist of close single-layer windings of enamel-covered nickel wires. For the TWC sensor, the collector winding is cemented to the hollow cone of a textolite cylinder while the reference sensor is wound within a shallow groove cut into the same cylinder. For the LWC sensor, both windings are wound on solid copper rods and cemented to opposite edges of a flat textolite plate. Because of this design, the LWC collector sensor is only responding to water drops since ice crystals are reflected. Due to its conical shape, the TWC collector sensor responds to water drops and ice crystals. Both sensors are operated separately by control boxes inside the fuselage, maintaining a fixed temperature of the collector windings and determining the power that is necessary to keep the temperature constant at the defined level. They output an analog signal between 0 V and 10 V.

#### **2.4. Ozone analysers**

Onboard Polar 4, two different ozone analysers had been used for ozone concentration measurements. One was an Ansyco (Karlsruhe, Germany) model O<sub>3</sub>41M, which uses UV absorption at 254 nm by ozone. It allows the selection of different measurement ranges between 0.1 ppm and 1 ppm with an accuracy of 1 ppb. Due to its function principle, the Ansyco O<sub>3</sub>41M delivers concentration values every 30 s and was therefore used as a slow-responding instrument for the precise determination of average ozone concentrations. For the investigation of mixing processes, it was necessary to have ozone concentration values at a high temporal resolution available. Therefore, a second probe was used that works according to chemoluminescence triggered by Coumarin-47. This probe, developed at Forschungszentrum Karlsruhe, allows the determination of ozone fluctuations at a rate of 50 Hz.

#### **2.5. Microwave radiometers**

In order to measure the microwave signatures of different types of sea ice, two non-imaging microwave radiometers have been designed in cooperation with the DLR (Deutsche Forschungsanstalt für Luft- und Raumfahrt, Institut für Hochfrequenztechnik). The radiometers operate at 19.35 GHz and 37 GHz with a bandwidth of 0.48 GHz and 1.8 GHz, respectively. The integration time was fixed at 20 ms. Both radiometers distinguish horizontal and vertical polarisation at an angle of view of 10°. The systems have an angle of incidence of 53°, looking at the sea surface behind the aircraft. By this configuration the same area was detected with both, the line scanners and the microwave radiometers.

## 2.6. Color Line Scanner on Polar 2

A high resolution Color Line Scanner (CLS) was mounted on Polar 2 to record the sea ice characteristics. The system consists of a cross-track scanner to measure the intensity of surface signals perpendicular to the flight track.

The Color Line Scanner discriminates simultaneously red ( $0.58\ \mu\text{m}$  to  $1.00\ \mu\text{m}$ ), green ( $0.48\ \mu\text{m}$  to  $0.58\ \mu\text{m}$ ), and blue ( $0.40\ \mu\text{m}$  to  $0.48\ \mu\text{m}$ ) colours. It has a field of view of  $90^\circ$ , and resolves each line in 1024 pixels. The altitude of the aircraft determines the width and the cross-track sample distance of the images. The scanner has a maximum sampling rate of 50 lines per second. The along-track sample distance is determined by the aircraft ground speed (typically 70 m/s, corresponding to 1.5 m). The image data are stored on tape, enabling four hours of acquisition time.

## 2.7. Line Scanners on Polar 4

Two different line scanner systems, sensitive in the visible (VLS) and thermal infrared (IRLS) spectral range (Bochert and Wamser, 1994) were mounted on Polar 4. Both devices consist of cross-track scanners which measure the intensity of surface signals perpendicular to the flight track. The swath angle of  $90^\circ$  is covered by 512 pixels. The altitude of the aircraft determines the width and the cross-track sample distance of the images. With a typical speed of 70 m/s the along-track sample distance is 1.5 m. The image lines are digitised during the measurement and stored on tape.

The Visible Line Scanner (VLS) measures solar radiation reflected by the ground surface in the spectral range from  $0.4\ \mu\text{m}$  to  $1.1\ \mu\text{m}$ . A linear CCD-array (Charge Coupled Device) is used as a detector. The Infrared Line Scanner (IRLS) detects the surface temperature in a spectral range between  $8\ \mu\text{m}$  and  $12\ \mu\text{m}$ . The detector, a single element semiconductor, is cooled to  $-190^\circ\text{C}$  by a Stirling-cooler in order to improve the signal-to-noise ratio. Scanning is carried out by a fast rotating tetragon-mirror. Radiation of two temperature controlled plates is measured as a reference, in order to achieve an absolute accuracy of about 1 K with a resolution of 0.1 K.

## 2.8. Aircraft mission types

The aircraft missions during ARTIST can be characterised as follows:

- **Convection:** Both aircraft flew coordinately in the developing boundary layer near the ice edge. Polar 2 operated mainly in the northern part over ice and water, Polar 4 mainly further south over water. Both aircraft flew vertical soundings, saw-tooth patterns and stacks of horizontal flight legs at different heights and several positions within the developing BL. On some days only one aircraft conducted a convection mission.
- **On-Ice Flow:** Both aircraft flew coordinately horizontal legs and saw-tooth patterns in a cloudy stratus layer during on-ice flow.
- **Arctic Haze:** For aerosol measurements, a ladder-type flight pattern was flown with horizontal legs at an angle of 80° to the direction of the sun. Measurements in the almucantar plane of the sun were performed on a half circle track towards both directions without banking angle.
- **Ice Roughness:** Horizontal flight sections of 50 to 100 km length were flown by Polar 2 in low level over rough sea ice. For this mission the Meteopod, laser altimeter, line scanner and surface thermometer were used.
- **Ny-Ålesund:** On two days the airflow in the valley of the Kongsfjord region was extensively measured by repeated traverses parallel and across the main fjord axis. On 4 additional days a pass through the fjord was flown.
- **Remote Sensing:** Polar 4 flew traverses at a constant height, arranged to optimise coverage of an area where ERS-2 satellite data are available. One of these flights has been arranged to coincide in time and location with a Danish airborne remote sensing mission. One further mission, also coordinated with a Danish flight, covered a large area of pancake ice, but no ERS-2 data are available.

In Table 2.5 a summary of the number of flights for each mission type is given.

**Table 2.5:** Summary of the number of flights per mission type.

mission	objective	Polar 2	Polar 4
1	convection	8	6
2	on-ice/stratus	3	3
3	arctic haze		1
4	ice roughness	2	
5	Ny-Ålesund	2 (+4)	
6	remote sensing		5

## 2.9. Site and instrumentation at Ny-Ålesund

The experimental site was located at the shore of Kongsfjord at the settlement of Ny-Ålesund (Figure 2.1) on the island of Spitsbergen (78.933°N, 11.933°W, 11 m a.s.l.). The instrumentation employed consisted of: a *three-axis Doppler Sodar* (Sound Detection and Ranging), a *tethersonde*, a *sonic anemometer*, a *fast response hygrometer*, and *upward and downward looking pyranometers and pyrgeometers*. The *sub-soil temperature* was measured by two thermocouples buried in the snow, at the depths of 8 cm and 17.5 cm. The Sodar was located at the coast of Kongsfjord in the Zeppelin Bay (site S in Figure 2.1) to avoid noise of the village of Ny-Ålesund. The tethered balloon was installed at the foot of a small coal hill at about 20 m above sea level (site T of Figure 2.1) in order to avoid interference with the Sodar system. An ISO 20 container was used to protect the balloon during strong wind episodes. The flight control and the data acquisition were located at the Italian Base (site IB in Figure 2.1). The sonic anemometer and the net radiometers were installed between the Sodar and the tethersonde (site R of Figure 2.1). In Figure 2.2 a picture of the instrumentation in the field is given.

## 2.10. Sodar

The Sodar, similar to that used in previous campaigns in Antarctica (Argentini et al., 1992, Argentini and Mastrantonio, 1994) was a monostatic three-axis Doppler system with 1.2 m diameter antennas, simultaneously emitting three acoustic signals at 1750, 2000, and 2250 Hz. Two of the antennas were tilted 20° off the vertical, while the third one pointed vertically. The length of the acoustic pulse was 100 ms, and the harmonic analysis of the signal to retrieve the radial wind was made with 0.16 s samples, corresponding to a height interval (range gates) of approximately 27 m: the first range gate being at 50 m.

A cross-beam configuration was chosen. The tilted antennas were located at the acute vertex of a rectangular triangle and they were oriented towards the vertically adjusted antenna. With the distance between the antennas being 27 m and the tilting angle 20° the beams were crossing at 67 m. To have the minimum cross-section of the antennas against the strongest wind flow, an angle of 30° between Y axis and Magnetic North was chosen, that is 26° with respect to the geographic North. By the harmonic analysis of the received signal, it is possible to derive the wind profile, and to visualise the dynamic evolution of the airflow crossing the antenna beams. The spectral analysis to retrieve the Doppler shift and the backscatter intensity of each channel is carried out by a two-step procedure (Mastrantonio and Fiocco, 1982): The spectrum of the echo is first localised, then the first moment determined refers to the expected signal bandwidth rather than to the full channel spectrum. For each channel antenna, the processing of the returned signal provides the profiles of the radial wind velocity and the echo intensity. The data are accepted when the signal-to-noise ratio S/N exceeds a given threshold (Mastrantonio and Fiocco, 1982).

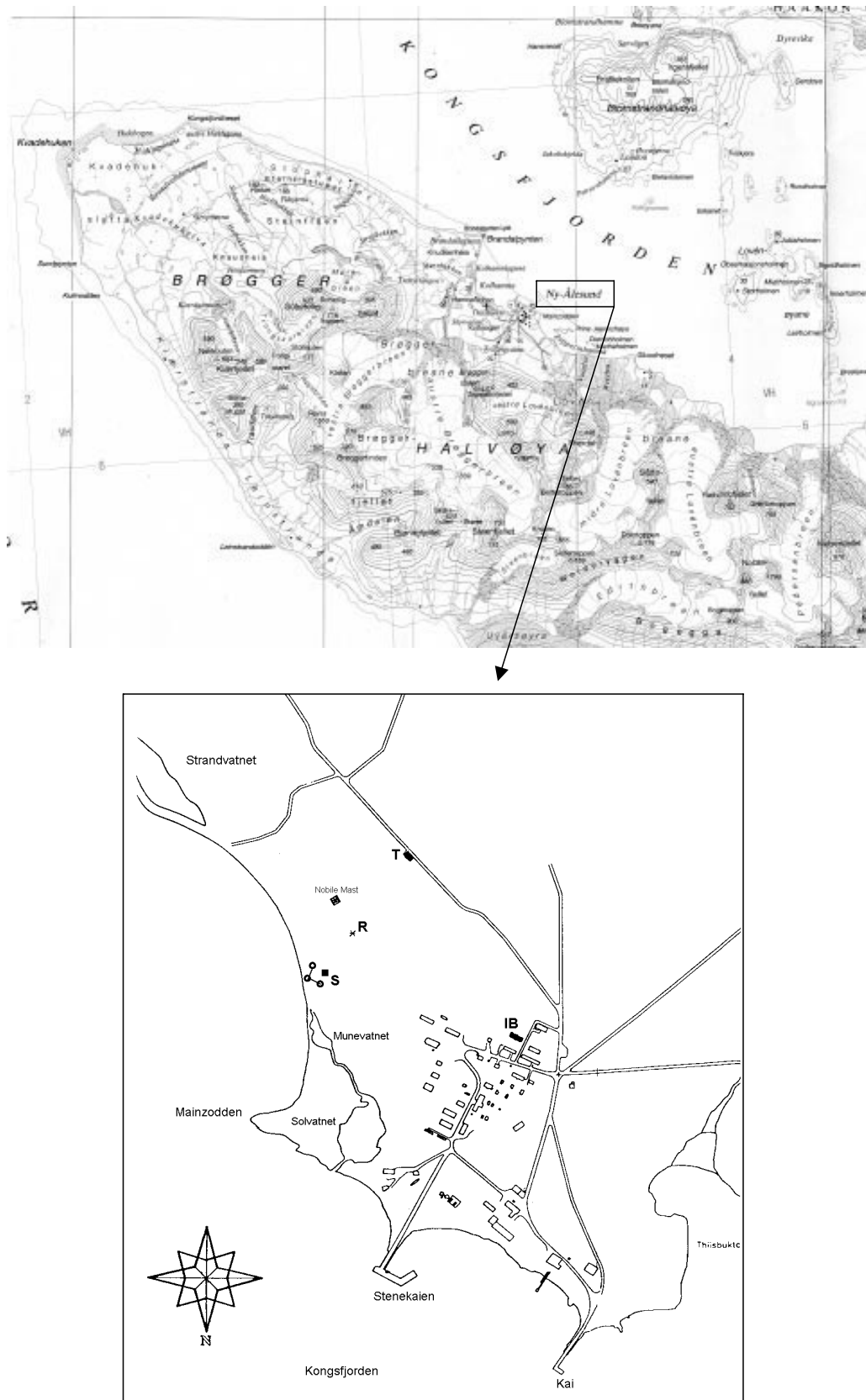


**Figure 2.1:** Map showing Ny-Ålesund in the island of Spitsbergen (top figure) and location of the experiment site at Ny-Ålesund: Sodar system (S), Radiation and fast response sensors (R), Italian Base (IB), Tethersonde location (T) (bottom figure).



**Figure 2.2:** Three-axis Sodar, fast-response sensor and radiation station during the field work in Ny-Ålesund.

### 2.11. Tethersonde

The tethersonde system used during the field experiment consisted of a ground station, a meteorological sonde, a 5 m<sup>3</sup> volume balloon and a winch with 1000 m of tetherline for the suspension of the balloon. The balloon is shaped in order to facilitate the orientation upwind. The tethersonde package, suspended about 2 m below the balloon includes: dry and wet bulb thermometers, an aneroid pressure sensor, an anemometer, a magnetic compass and a 403.5 MHz transmitter.

The temperature sensors have an accuracy of  $\pm 0.5^{\circ}\text{C}$ , the wind speed is measured to  $\pm 0.5\text{ m/s}$ . The direction measurement relies on the orientation of the balloon and has an accuracy of  $\pm 5^{\circ}$ . An aneroid barometer gives pressure to an accuracy of 1 hpa. The altitude of the sensor package above the surface is derived from the pressure and temperature profile.

During the flight the electronics of the sonde scanned the sensors sequentially and transmitted the raw data to the ground station every 6 seconds. The data were then processed to give the profiles of the potential temperature, relative humidity, wind speed and direction. The balloon could only be operated for wind speeds less than 6 m/s.

Before the launch a preflight control was done by measuring the temperature and pressure with ground sensors. During the flight the correct functioning of the system (including battery check) and the data quality were checked on-line to allow real time modification of the fly plans.

## 2.12. Surface radiation sensors

A radiometer model CNR1 (Kipp and Zonen) was used for the determination of the solar radiation balance. The short- and long-wave incoming and outgoing radiation components were measured separately to derive the net radiation ( $R_n$ ) at the Earth surface. Solar radiation was measured by two pyranometers (CM3), one for the incoming radiation from the sky ( $E_{s\downarrow}$ ), and the other facing downward measured the radiation reflected from the snow ( $E_{s\uparrow}$ ). Two pyrgeometers (CG3) measured the far infrared radiation ( $E$ ) from the sky ( $E_{l\downarrow}$ ) and from the snow surface ( $E_{l\uparrow}$ ). The self-heating of the instruments was estimated by a Pt-100 (platinum-wire thermistor) incorporated in the CNR's body. The net radiation  $R_n$  results as

$$R_n = E_{s\downarrow} + E_{l\downarrow} - E_{s\uparrow} - E_{l\uparrow}$$

## 2.13. Surface turbulence equipment

A sonic anemometer model USA-1 (Metek) was used for turbulence measurements. It was aligned to the North with a precision of  $15^\circ$ . The sonic anemometer height above the ground was 3.40 m in order to avoid ground effects. Moreover, it was located in a flat zone with little obstruction nearby. The vertical alignment of the sonic anemometer was assured by two optical levels to a precision of  $1^\circ$ .

A Krypton hygrometer model KH20 (Campbell Scientific) was located on the same mast to measure the latent heat flux by means of the eddy-covariance technique. The humidity signal was collected at a frequency of 10 Hz. The raw data were collected by a MeteoFlux computer system performing real-time measurements of the 3 wind components and the sonic temperature. From these data the turbulence variables as well as the sensible and the latent heat fluxes were derived.

## 2.14. Drifting buoys

The airborne measurements over Fram Strait are complemented by continuous recordings from buoys on the sea ice in the north of the area of study. One buoy was deployed by airdrop at the beginning of the campaign at  $82^\circ\text{N } 12^\circ\text{E}$ . Another 4 buoys had arrived in the area after following the transpolar ice drift from their deployment positions during the previous year(s).

The buoys measure atmospheric pressure, air temperature and GPS-position at hourly intervals. The data are transmitted by satellite via the ARGOS system, and entered into the global transmission system for weather data (GTS). Detailed information on the instrumentation and capabilities of the buoy systems are described by Kottmeier and Lüdemann (1996).

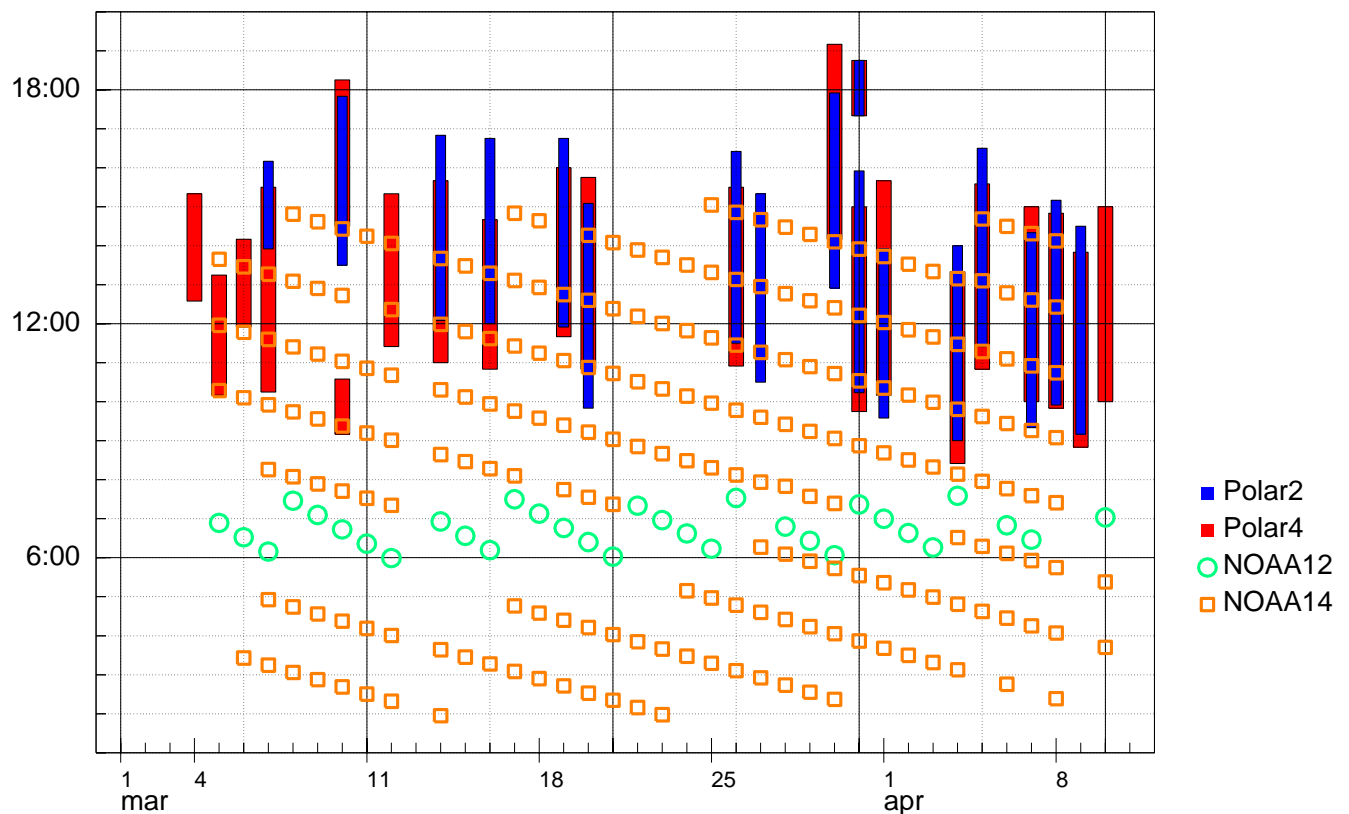


**Figure 3.1:** Timetable of aircraft flights and NOAA satellite passes during the field campaign. This ordinate shows UTC time. On each day consecutive satellite passes moved over Svalbard from east to west.

### 3. Measurement Inventory

This section contains an inventory of the various data sets collected during the campaign. First, a timetable of satellite data (NOAA and ERS 2 SAR) is presented, followed by a catalogue of the flight missions and listings of the Ny-Ålesund ground based data.

#### 3.1. Satellite data

Data from the NOAA satellites have been obtained from the Tromsø Satellite Station. The satellite passes and aircraft flights are marked in Figure 3.1.

ERS-2 SAR frames have been obtained for days with remote sensing missions. A listing of the available frames with time and corner coordinates is given in Table 3.1.

**Table 3.1:** Inventory of ERS-2 SAR frames.

Date 1998	Time UTC	orbit frame	Corner Coordinates of ERS-2 SAR Frames							
			N	E	N	E	N	E	N	E
12 Mar	12:18	15122 1917	81.647	12.853	81.043	17.132	81.661	21.613	82.312	17.326
	12:18	15122 1935	80.952	9.095	80.390	13.291	81.053	17.196	81.657	12.915
	12:18	15122 1943	80.632	7.596	80.088	11.740	80.768	15.419	81.359	11.168
	18:56	15126 1656	80.268	13.486	80.824	17.667	81.535	13.949	80.938	9.674
	18:56	15126 1665	80.603	11.674	81.179	15.907	81.872	11.887	81.253	7.590
	18:57	15126 1683	81.243	7.665	81.862	11.952	82.512	7.245	81.845	2.974
15 Mar	12:23	15165 1917	81.648	11.409	81.044	15.689	81.663	20.170	82.313	15.883
	12:24	15165 1935	80.953	7.646	80.391	11.843	81.054	15.750	81.658	11.469
	12:24	15165 1943	80.633	6.151	80.089	10.295	80.768	13.972	81.354	9.721
18 Mar	12:29	15208 1917	81.648	9.960	81.044	14.240	81.663	18.721	82.313	14.433
	12:29	15208 1935	80.953	6.200	80.391	10.397	81.054	14.303	81.658	10.022
19 Mar	18:37	15226 1674	80.930	14.772	81.527	19.047	82.200	14.698	81.558	10.399
	18:37	15226 1683	81.245	12.695	81.864	16.993	82.514	12.283	81.847	8.012
21 Mar	12:35	15251 1917	81.649	8.523	81.045	12.804	81.664	17.285	82.314	12.996
	12:35	15251 1935	80.953	4.762	80.391	8.959	81.054	12.866	81.659	8.585
24 Mar	12:41	15294 1917	81.648	7.087	81.045	11.367	81.663	15.847	82.313	11.560
	12:41	15294 1935	80.953	3.324	80.391	7.521	81.054	11.428	81.658	7.147
27 Mar	12:46	15337 1917	81.649	5.648	81.045	9.928	81.664	14.409	82.314	10.122
	12:47	15337 1953	80.227	1.343	79.705	2.726	80.402	6.137	80.964	1.939
30 Mar	12:52	15380 1917	81.649	4.201	81.046	8.482	81.664	12.962	82.314	8.673
	12:52	15380 1935	80.953	0.440	80.392	4.637	81.055	8.543	81.659	4.262
	19:31	15384 1647	79.929	6.578	80.465	10.696	81.193	7.250	80.617	3.014
	19:31	15384 1665	80.611	3.049	81.187	7.283	81.880	3.262	81.261	1.036
6 Apr	12:32	15480 1917	81.650	9.241	81.046	13.522	81.665	18.003	82.315	13.714
	12:32	15480 1935	80.954	5.480	80.393	9.677	81.056	13.584	81.660	9.302
	12:32	15480 1953	80.227	2.248	79.703	6.317	80.402	9.729	80.965	5.530
9 Apr	12:37	15523 1899	82.305	12.201	81.656	16.490	82.220	21.626	82.919	17.451
	12:38	15523 1917	81.649	7.800	81.046	12.081	81.665	16.561	82.315	12.272
	12:38	15523 1935	80.954	4.041	80.393	8.238	81.056	12.144	81.660	7.862
10 Apr	12:06	15537 1898	82.304	20.105	81.655	24.395	82.219	29.529	82.918	25.352
	12:06	15537 1917	81.649	15.704	81.045	19.986	81.664	24.466	82.314	20.177
	12:06	15537 1935	80.953	11.945	80.392	16.142	81.055	20.049	81.659	15.767

### 3.2. Airborne missions

All flights of Polar 2 and Polar 4 during ARTIST are listed in Table 3.2. The tracks of the flights, a satellite picture and a short description of the weather and flight details are shown on the following pages.

**Table 3.2:** Flight missions of Polar 2 and Polar 4 during the ARTIST field campaign. A bold aircraft type in column 3 and 4 indicates a coordinated mission of both aircraft in the same region. The buoydrop flights at the beginning of the campaign have been conducted without data acquisition system. Bold type setting in column 5 indicates the availability of measured data.

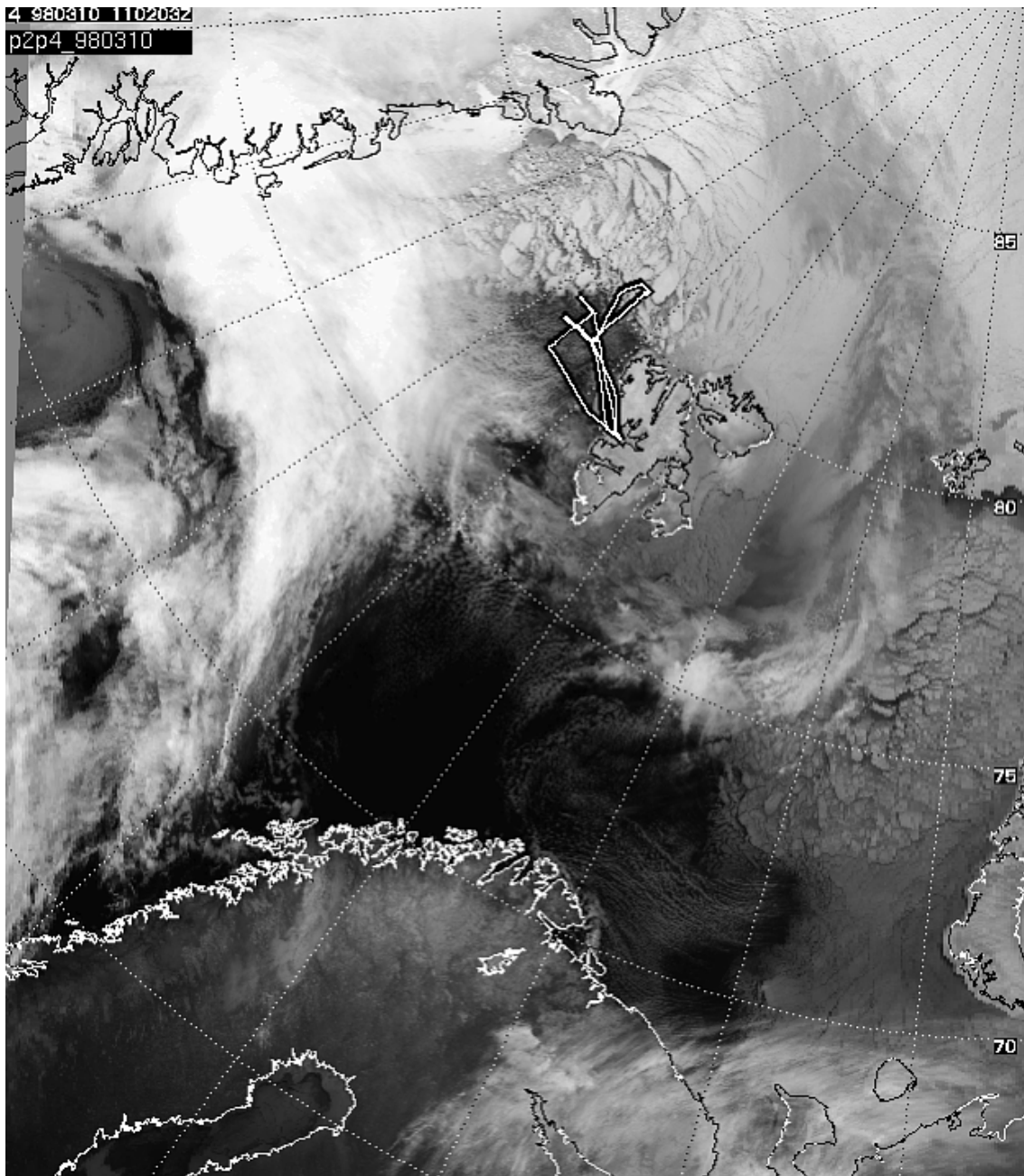
<i>date</i>	<i>day</i>			<i>mission</i>	
04 March	a		P4	buoydrop	
05 March	b		P4	buoydrop	
06 March	c		P4	testflight	
07 March	d	P2	P4	testflight convection	no data
10 March	e	<b>P2</b>	<b>P4</b>	<b>convection</b>	boundary layer development
12 March	f		P4	<b>remote sensing</b>	ERS-2, DMSP
14 March	g	<b>P2</b>	<b>P4</b>	<b>on ice</b>	Storfjord
16 March	9	P2	P4	<b>on ice</b> <b>photometer</b>	Storfjord, 6000 m
19 March	i	P2	P4	<b>convection</b> <b>remote sensing</b>	Fram Strait Danish cooperation, north
20 March	j	P2	P4	<b>convection</b> <b>remote sensing</b>	ice on Meteopod, Ny-Ålesund Danish cooperation, south
26 March	k	<b>P2</b>	<b>P4</b>	<b>stratus</b>	
27 March	l	P2		<b>ice roughness</b>	on ice flow
30 March	m	P2	P4	<b>convection</b> <b>remote sensing</b>	cross wind legs only ERS-2, DMSP
31 March	n	<b>P2</b> <b>P2</b>	<b>P4</b> <b>P4</b>	<b>convection</b> comparison flight	on ice flow, Ny-Ålesund
1 April	o	P2	P4	<b>Ny-Ålesund</b> <b>remote sensing</b>	pancake ice
4 April	p	<b>P2</b>	<b>P4</b>	<b>cold air outbreak</b>	
5 April	q	<b>P2</b>	<b>P4</b>	<b>cold air outbreak</b>	Ny-Ålesund
7 April	r	P2	P4	<b>Ny-Ålesund</b> <b>remote sensing</b>	radiation calibration ERS-2, DMSP
8 April	s	<b>P2</b>	<b>P4</b>	<b>convection cells</b>	tomography pattern
9 April	t	<b>P2</b>	<b>P4</b>	<b>cold air outbreak</b>	
10 April	u		P4	<b>remote sensing</b>	ERS-2, DMSP
11 April	v		P4	calibration	particle probes calibration

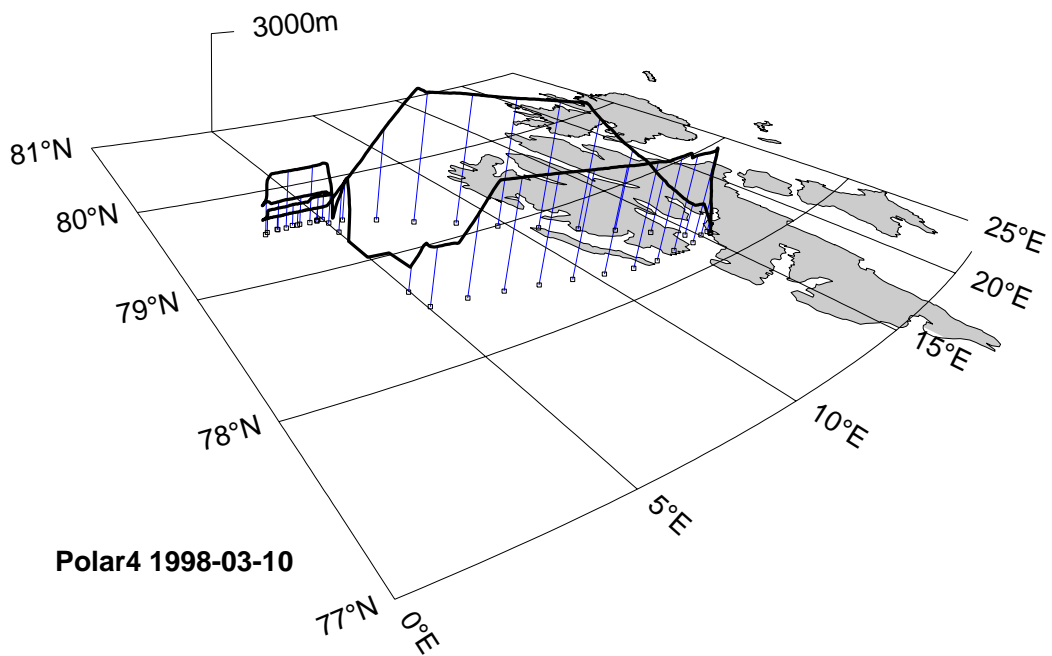
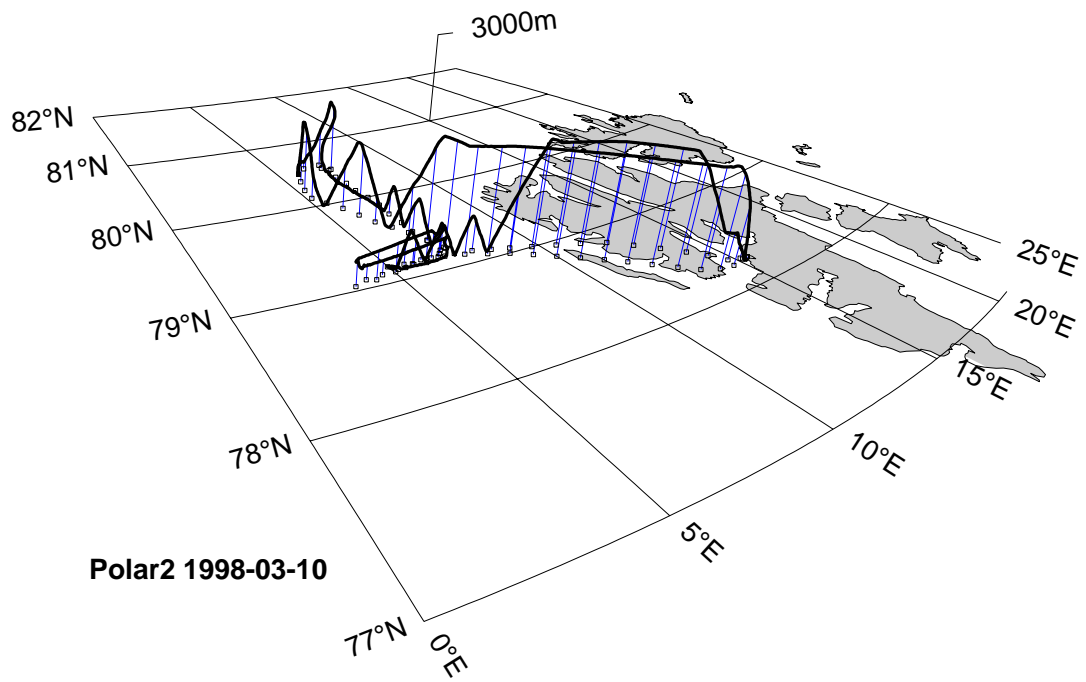
**10 March 1998**

Between high pressure over Greenland and low pressure over Svalbard and north of the islands, cold air was flowing off the ice into the Fram Strait region. Cloud streets with an orientation of  $210^{\circ}/30^{\circ}$  developed over the open water. The tops of the convective clouds ranged from 700 to 1000 m.

**Polar 2:** Ascent and descent over the ice, southbound saw-tooth pattern in the boundary layer, 4 cross-flow legs at  $79^{\circ}\text{N}$  over water.

**Polar 4:** 4 cross-legs at about 100 km south of the ice edge.



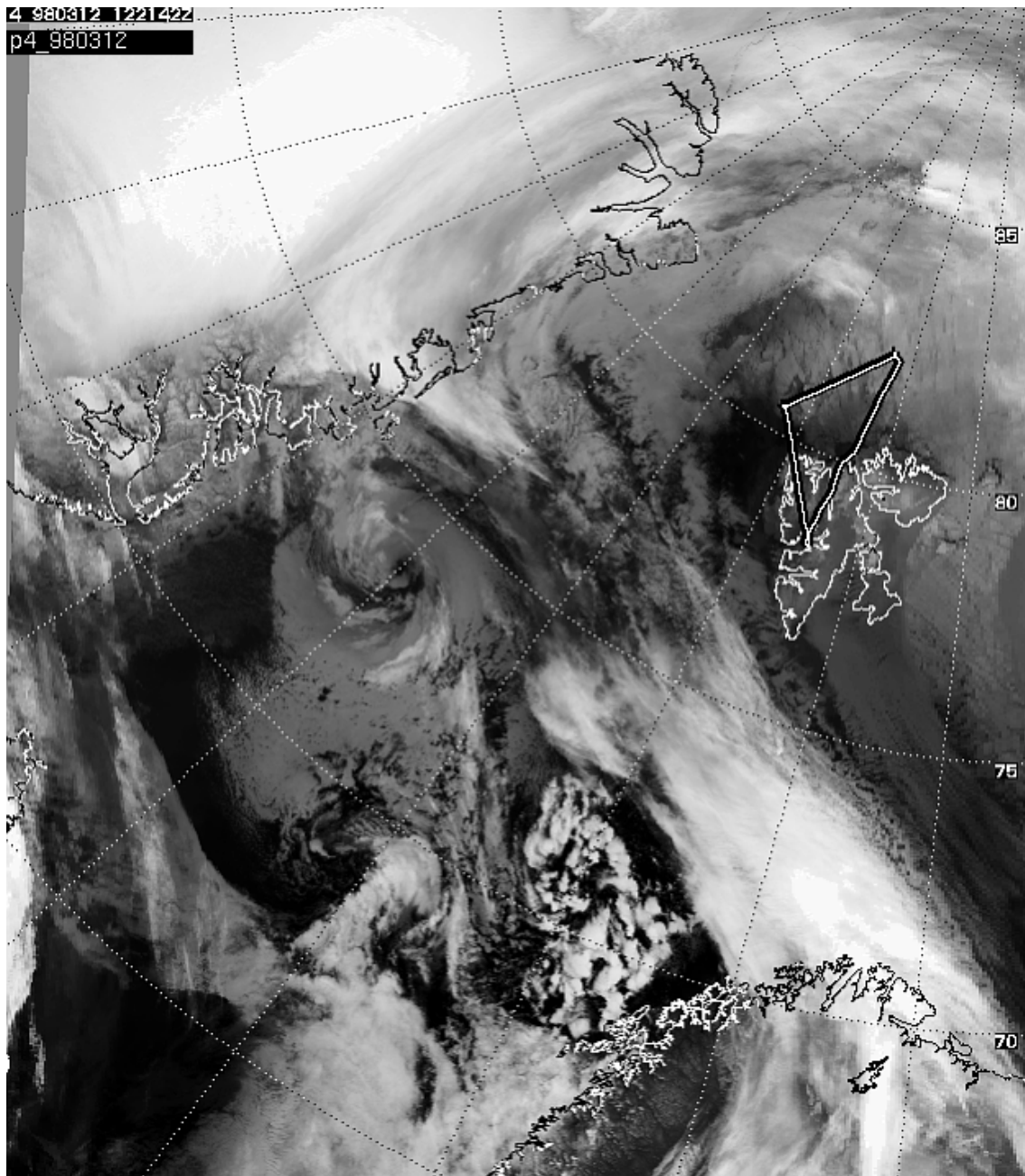


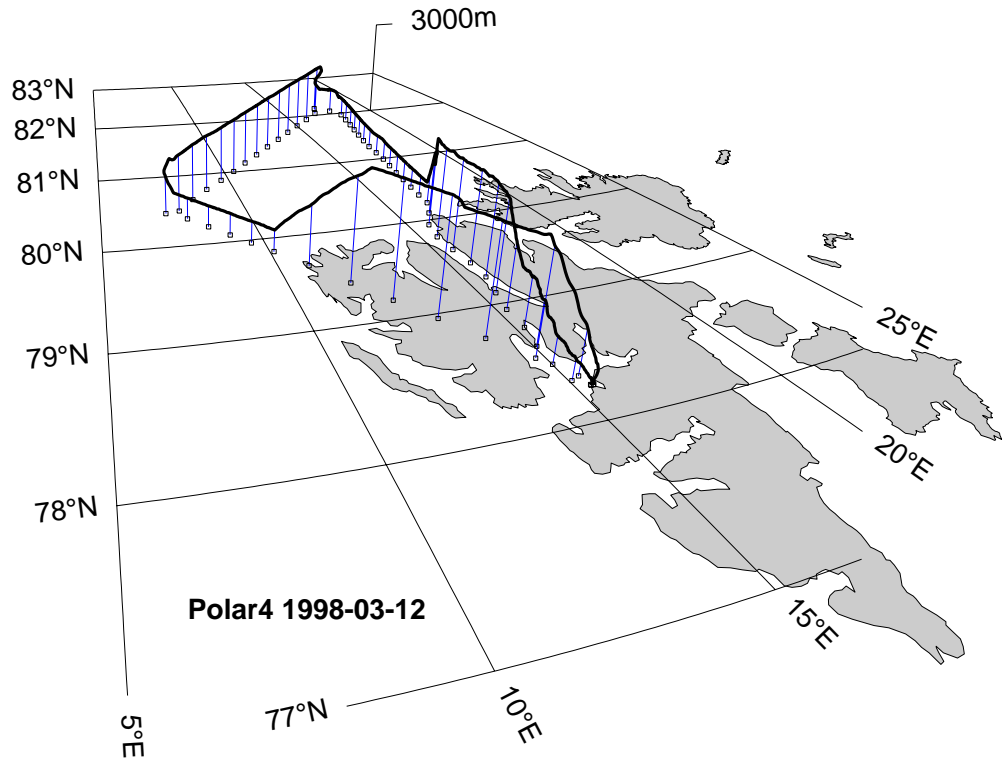
**12 March 1998**

High pressure east of Svalbard and low pressure in the Greenland Sea led to warm air advection over Svalbard and the sea ice north of it. Apart from few high cirrus clouds the sea ice north of Svalbard was cloud free. Some low level clouds appeared at the northern coast of the island. Due to the continuous on-ice flow during the previous days the ice edge was situated at  $80^{\circ}16'N$  north of Svalbard.

**Polar 2:** No flight.

**Polar 4:** Long legs at 1 500 ft over the ice north of Svalbard for remote sensing.



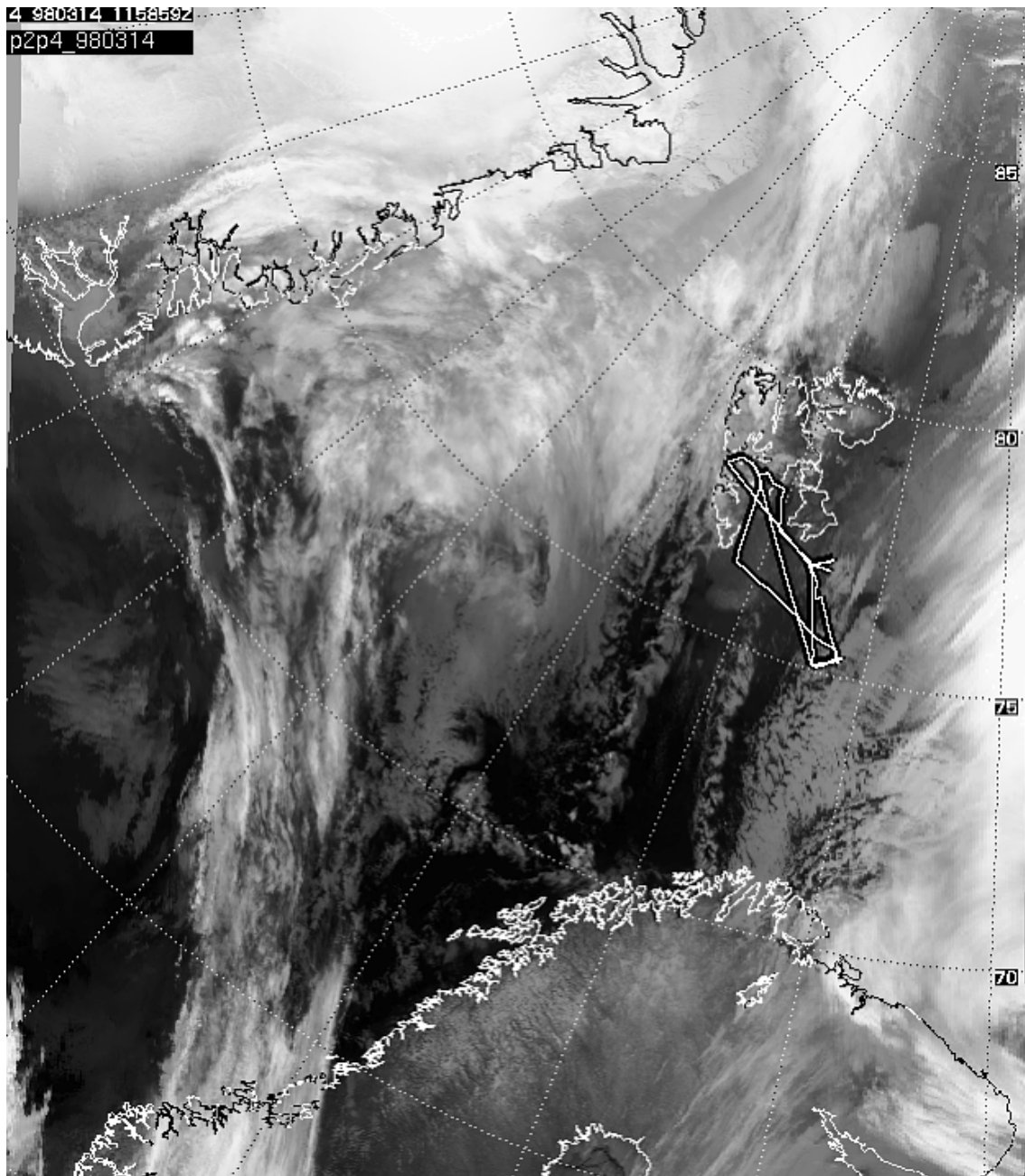


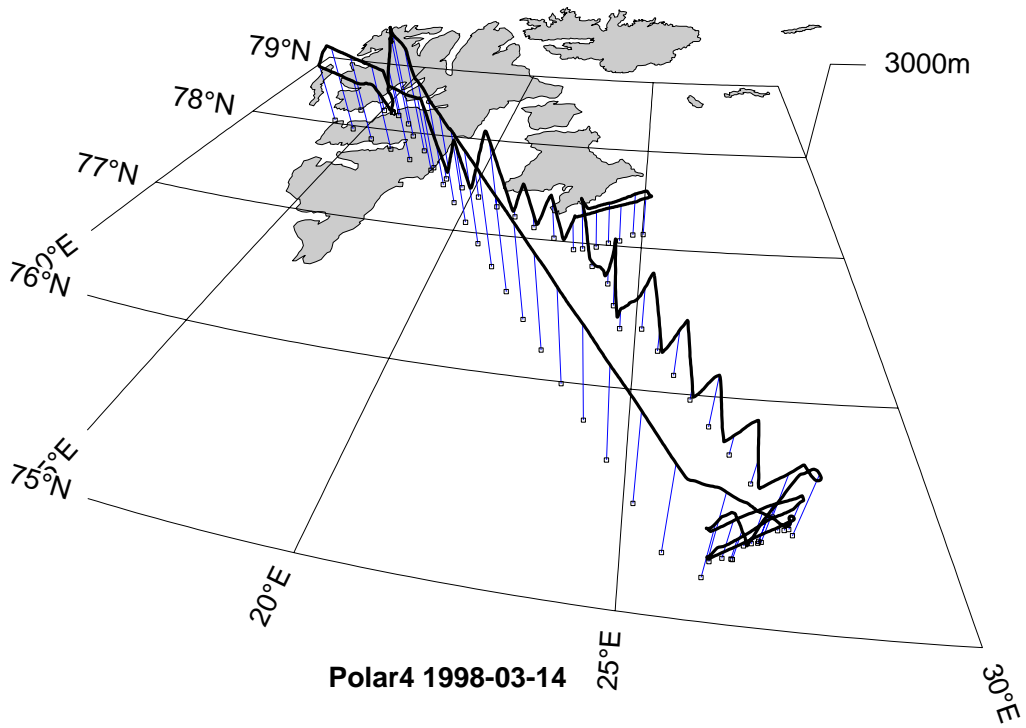
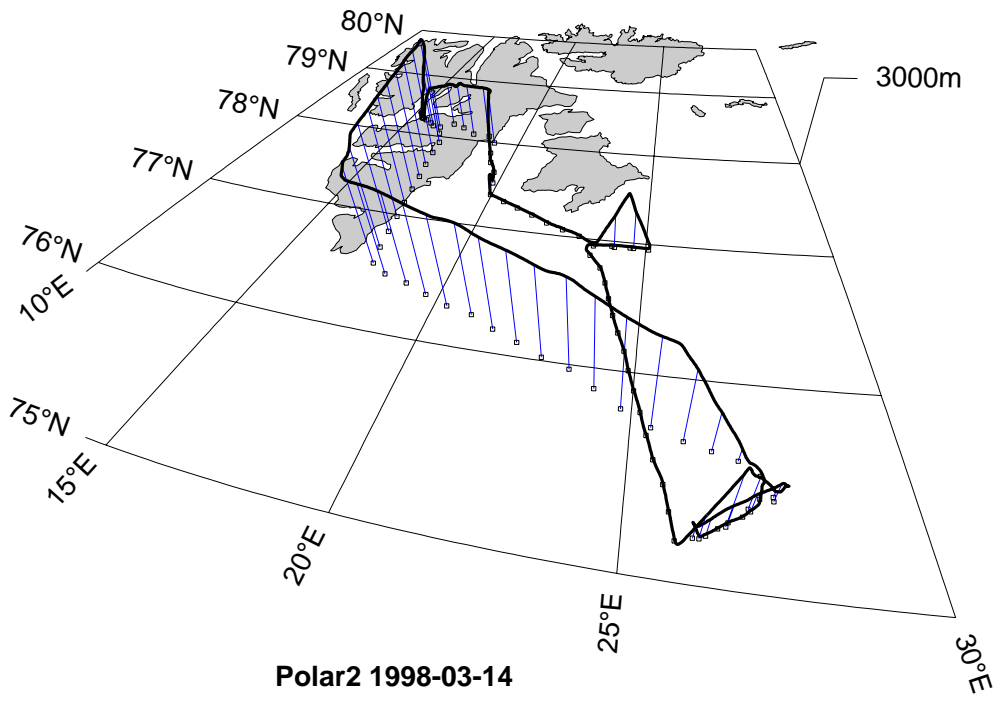
**14 March 1998**

At the western flank of a high pressure cell over Novaya Zemlya cool air originating from Siberia was flowing over the Barents Sea towards Svalbard. Convective clouds developed in the south-east of Spitsbergen over the water.

**Polar 2:** One stack of cross flow legs over the water at 75°N 27°E and one over the ice in Storfjord.

**Polar 4:** Stacks of cross flow legs at approximately the same location as Polar 2.



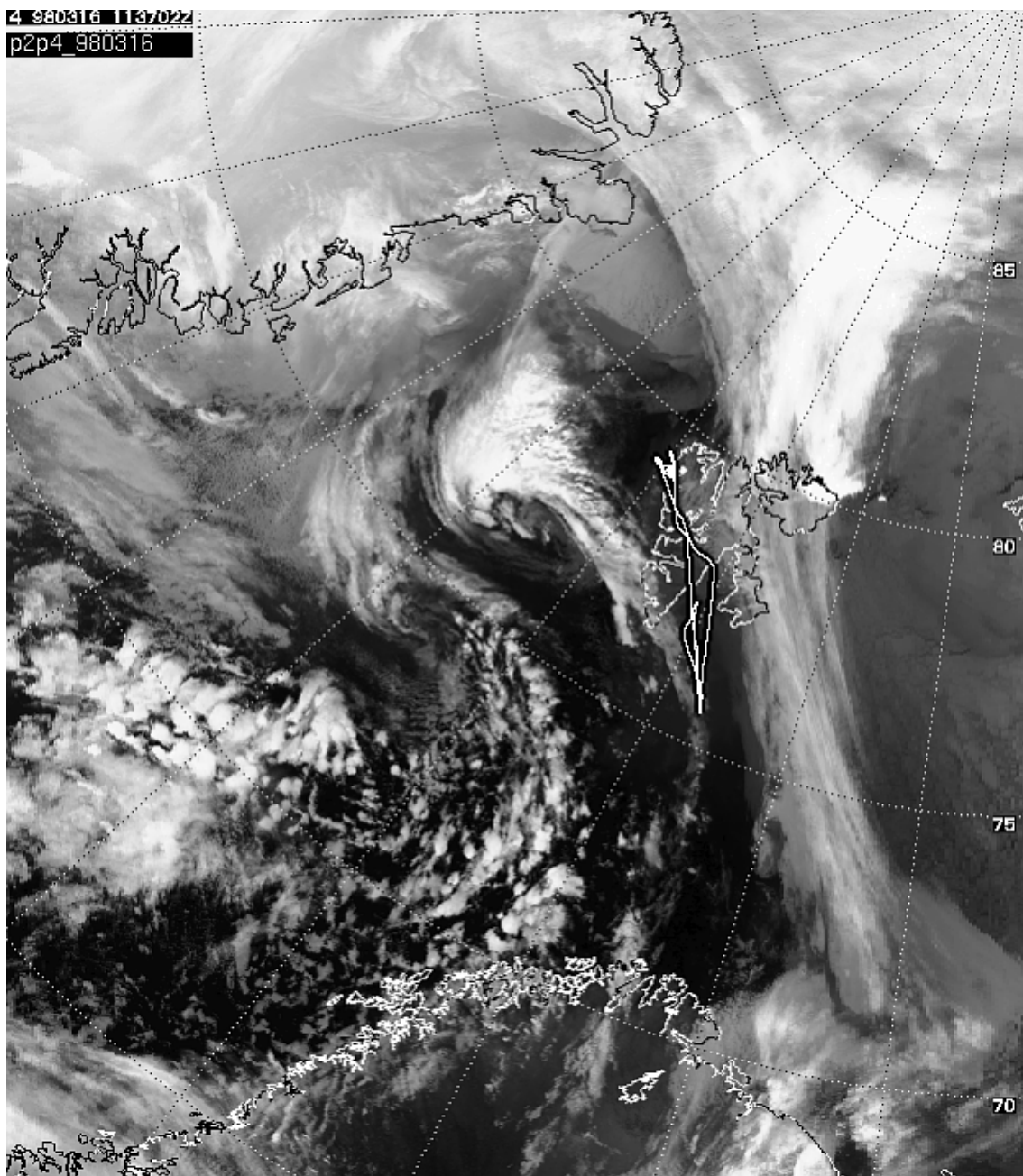


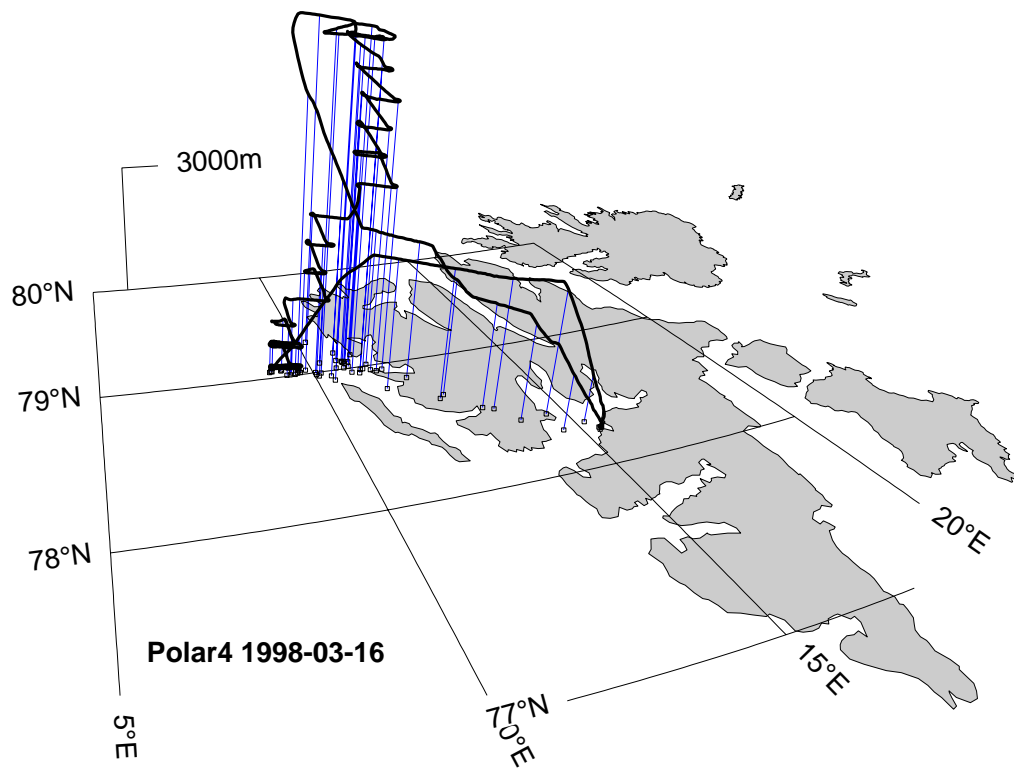
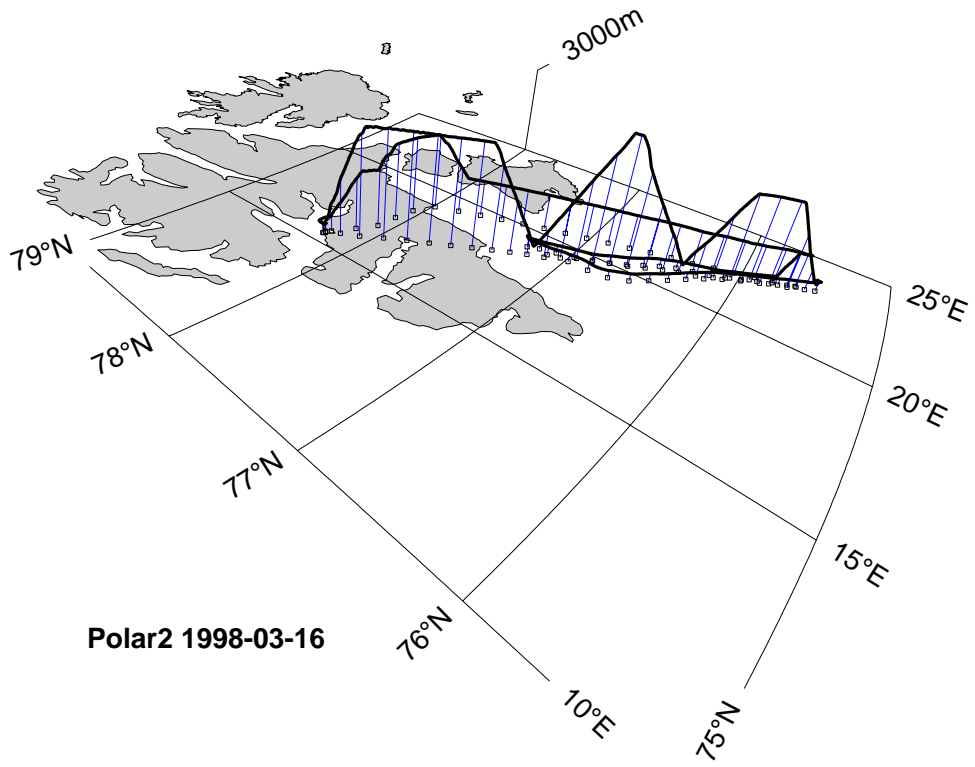
**16 March 1998**

A small low-pressure system east of Greenland moved towards Svalbard. Ahead of this low warm air was advected onto the pack ice region from the south east. Clear sky conditions prevailed in the western and northern part of Svalbard.

**Polar 2:** Turbulence measurements over the ice during low-level legs parallel to the mean wind direction in the on-ice flow over the Storfjord.

**Polar 4:** Photometer measurements: ladder-pattern in the cloud-free region over and west of Ny-Ålesund. The flight reached a level of 7300 m.



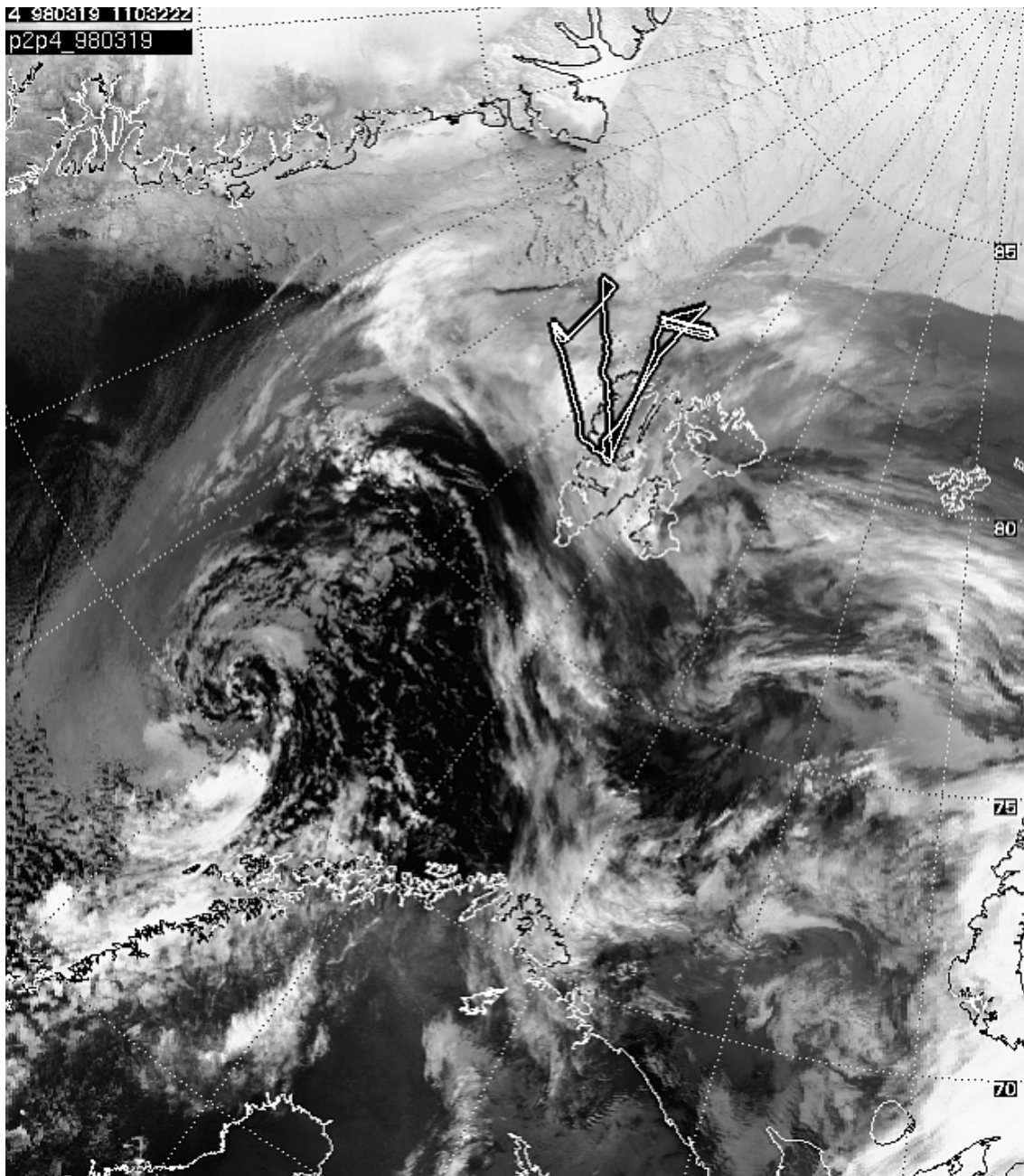


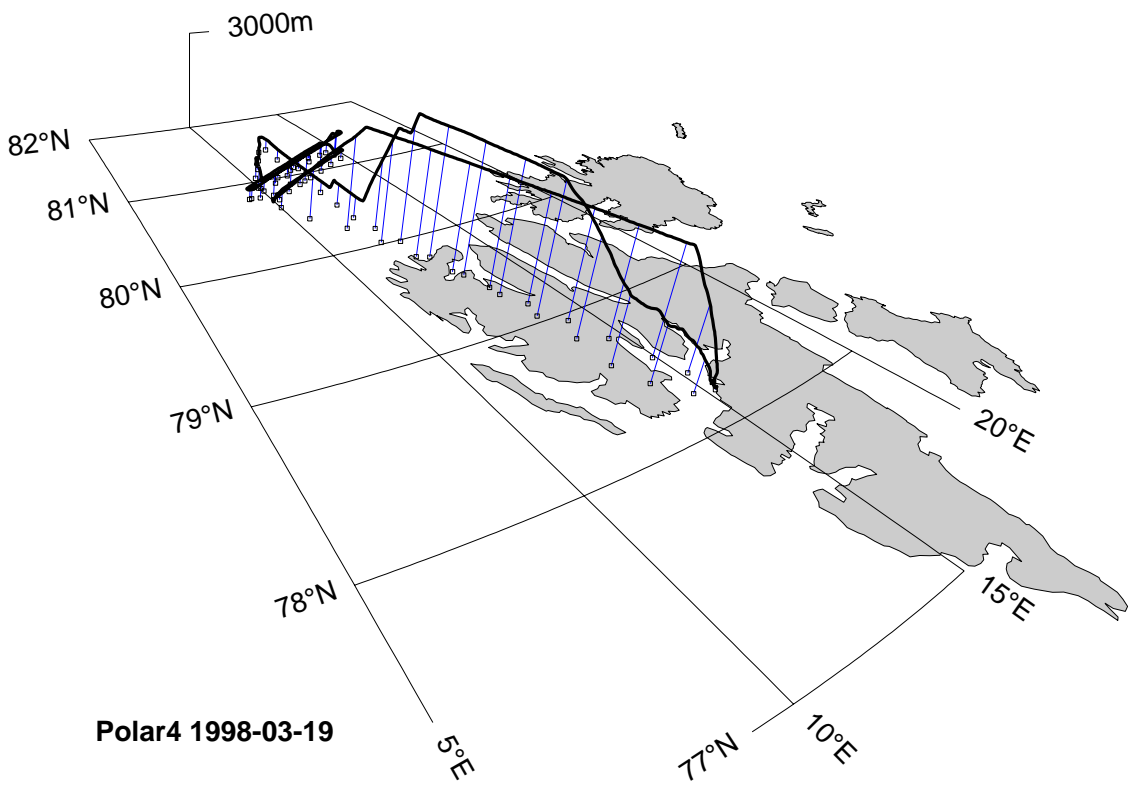
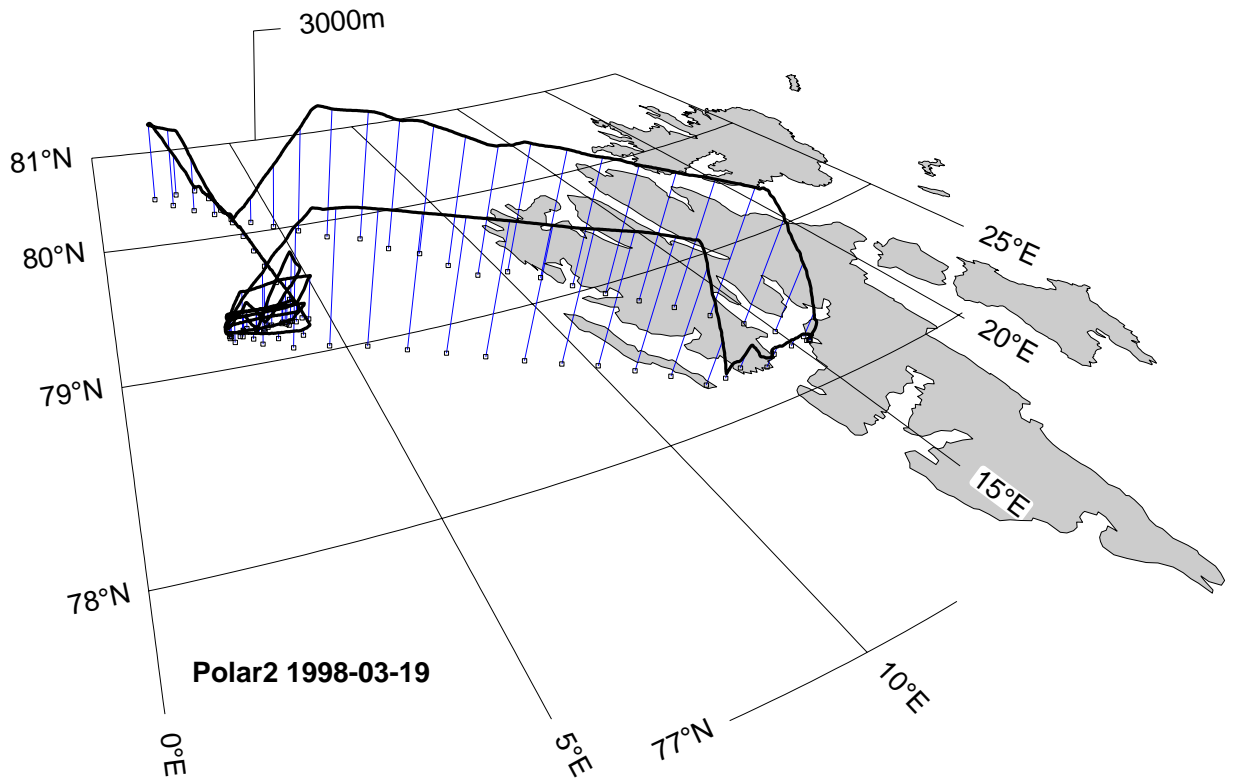
**19 March 1998**

A low-pressure system over the Norwegian Sea led to northerly winds in the Fram Strait region. A shallow stable boundary layer with a minimum air temperature of  $-30^{\circ}\text{C}$  covered the pack ice. Convection developed over the open water, but due to the strong wind no cloud street organisation occurred.

**Polar 2:** Cross-flow legs in the convective boundary layer at 100 km south of the ice edge in the Fram Strait.

**Polar 4:** Remote sensing mission to the north of Spitsbergen at  $81^{\circ}\text{N } 12^{\circ}\text{E}$  at heights of 300 m and 600 m. This flight was coordinated with the Danish airborne EMISAR operation of Danish Center for Remote Sensing.



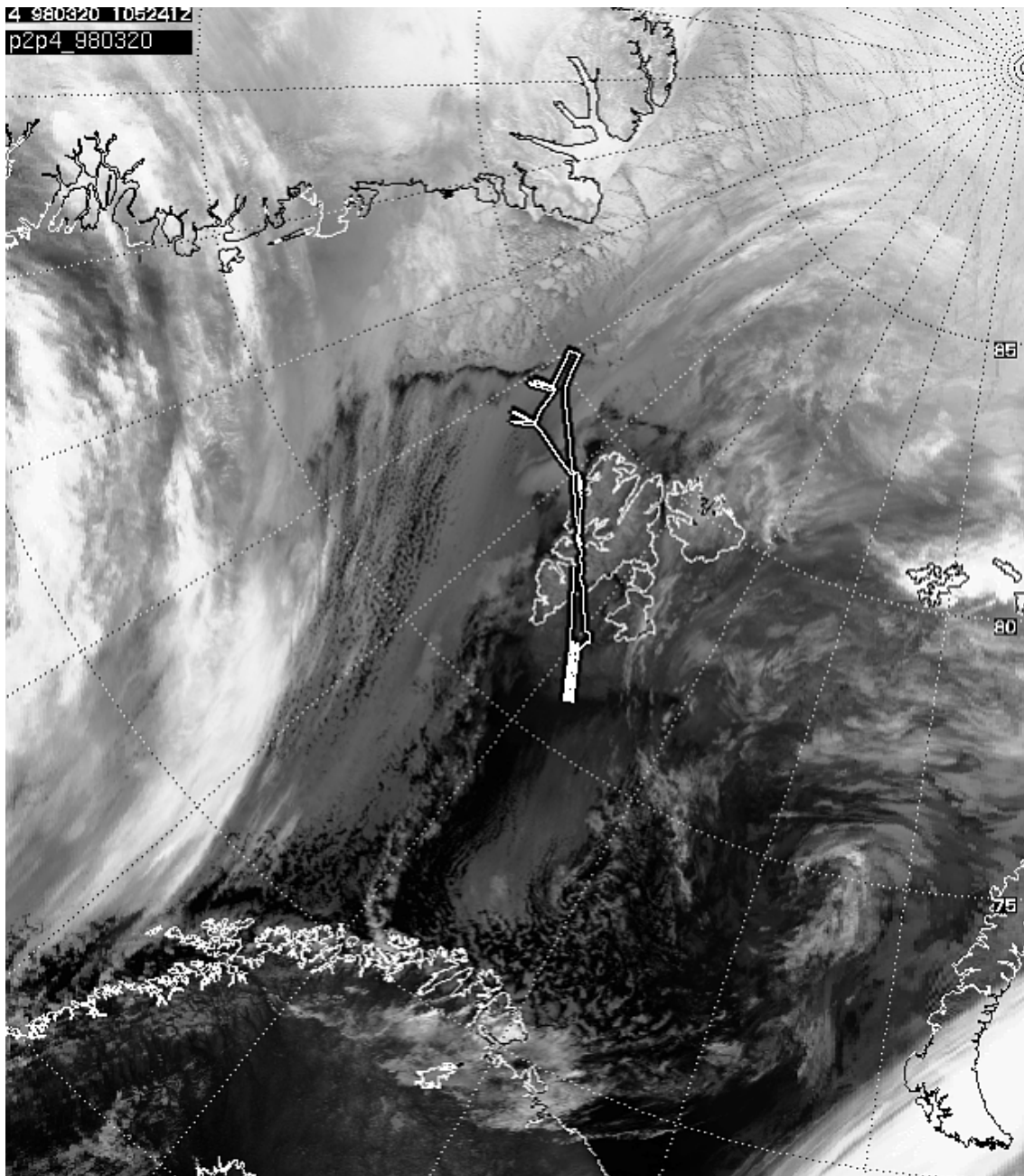


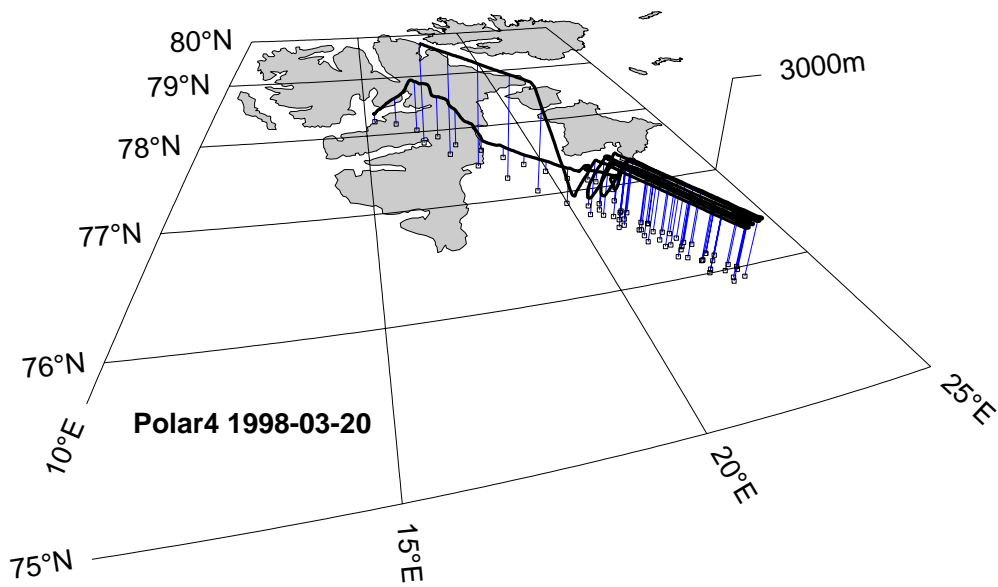
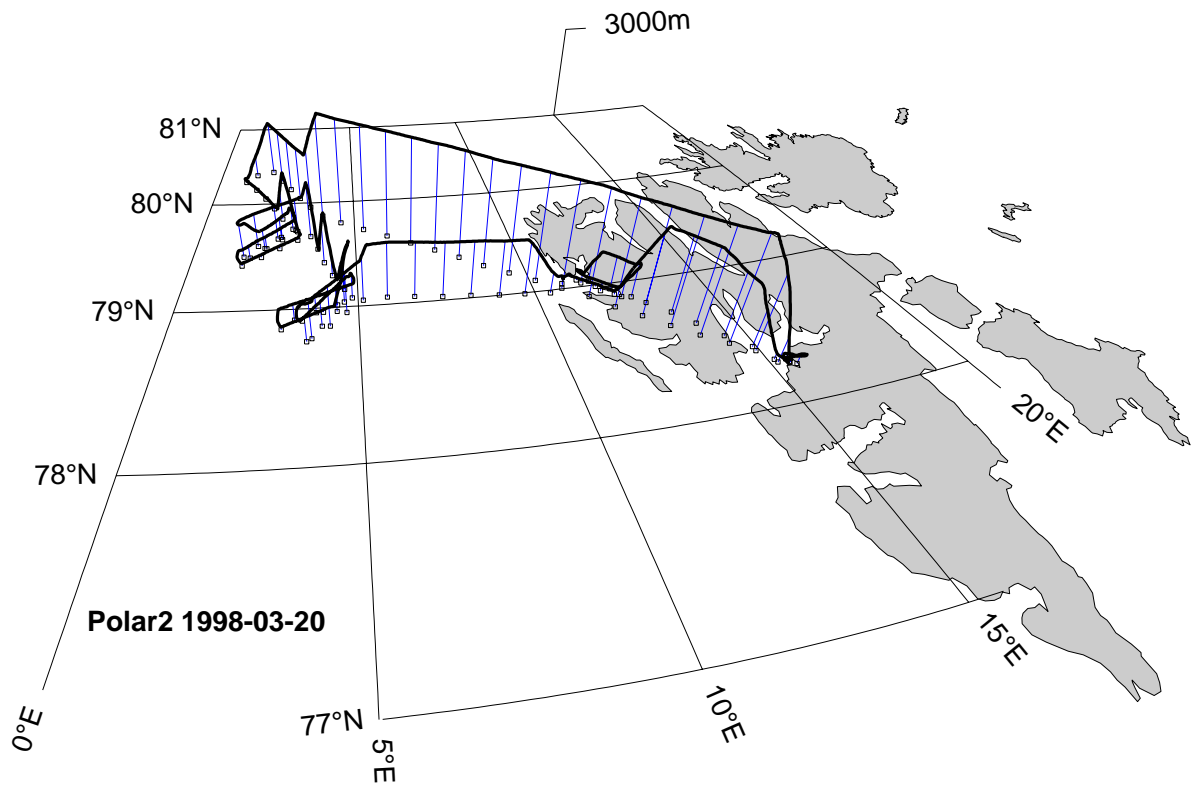
**20 March 1998**

The weather in the Fram Strait region was controlled by a low pressure system between Svalbard and Novaya Zemlya. Cold air was flowing off the ice from a north-westerly direction. The open water was covered by 7/8 to 8/8 stratocumulus. The sea ice and Svalbard was nearly free of clouds.

**Polar 2:** Mission to study the development of the convective boundary layer. Stacks of cross legs were flown at two distances from the ice edge in the Fram Strait.

**Polar 4:** Remote sensing mission south of the Storfjord at 1.5 km height. As on the previous day this flight was coordinated with the Danish mission.

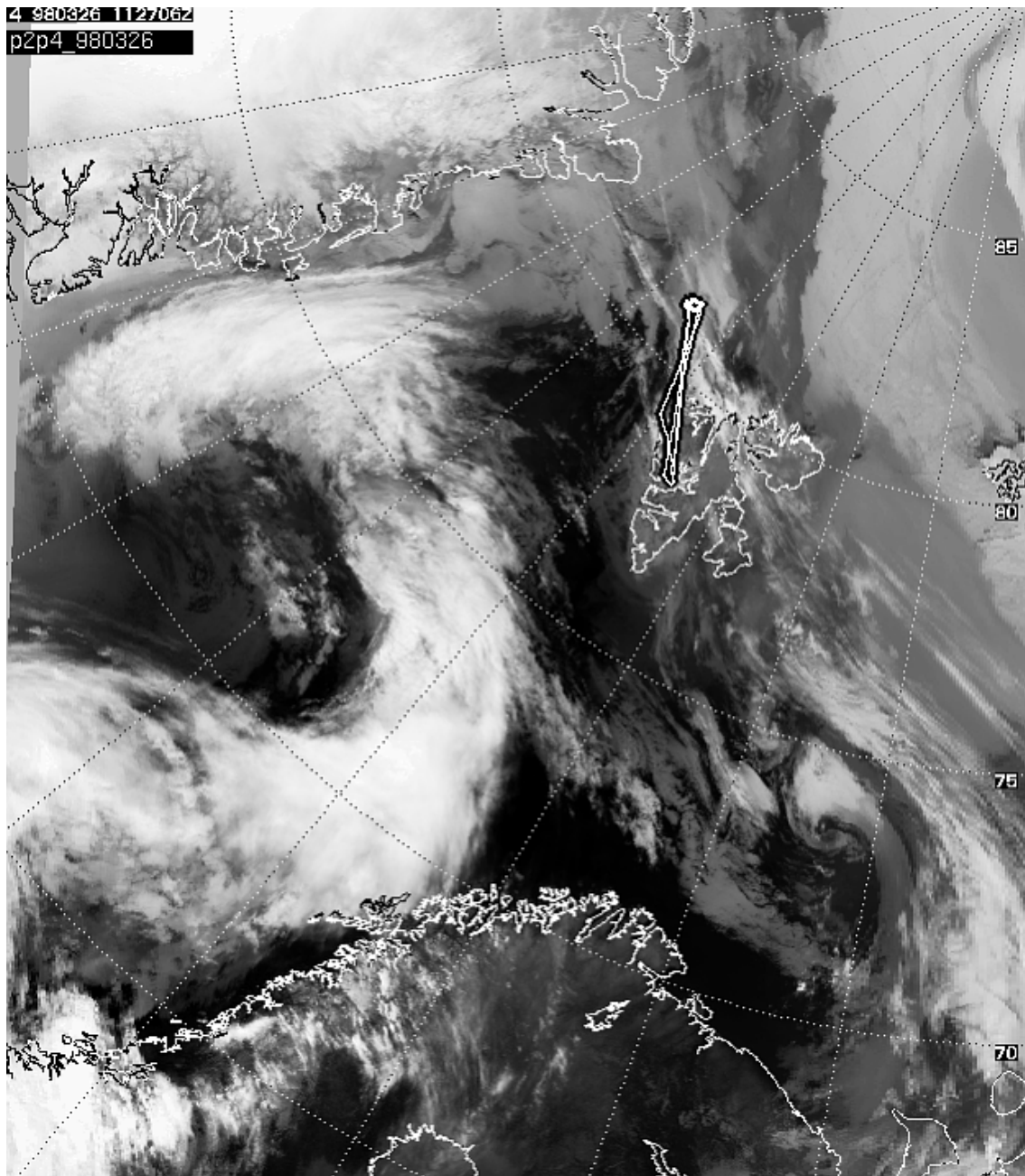


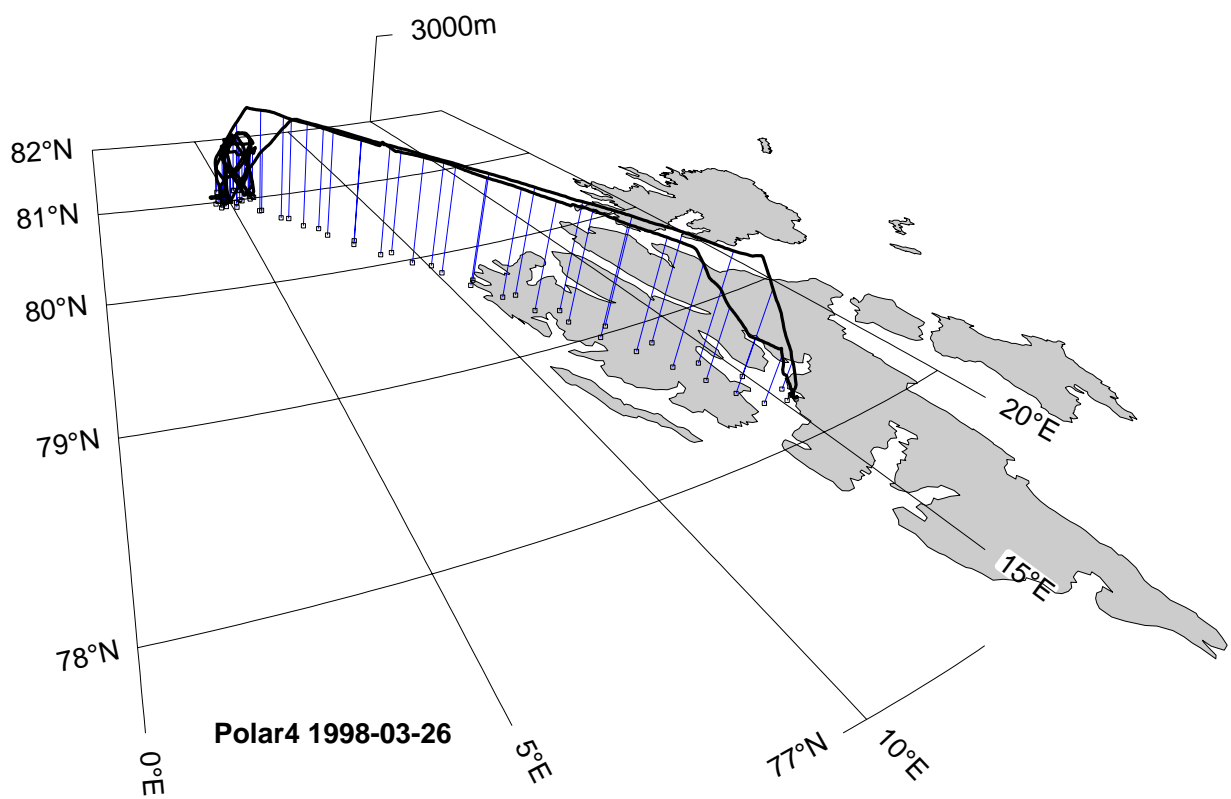
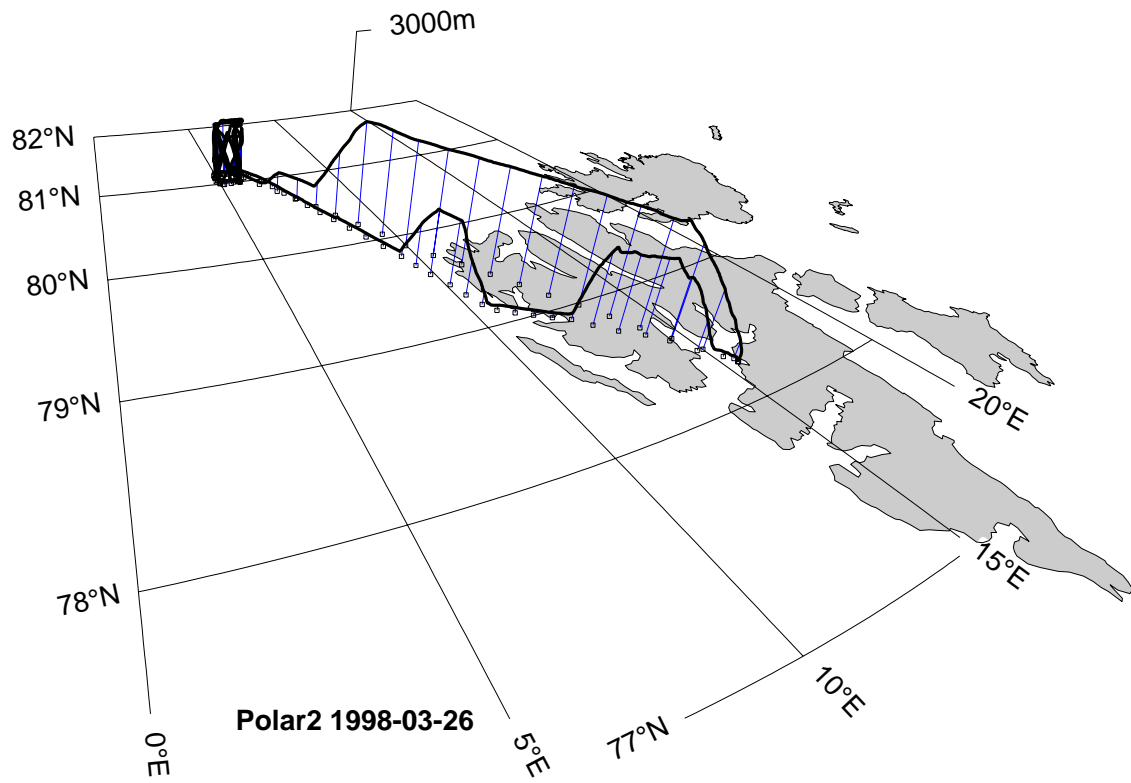


**26 March 1998**

A strong and intensifying high pressure cell over the central Arctic and a low at Jan Mayen produced an on-ice flow over Fram Strait. Warm and moist air was advected over Svalbard towards the northern end of Greenland. The sea ice and part of the open ocean were covered by low stratus clouds.

Both aircraft flew a coordinated mission at 81°N 5°E within a stratus cloud deck over the sea ice. A square of 8 by 8 NM was circled six times in heights between 50 m and 2000 m.



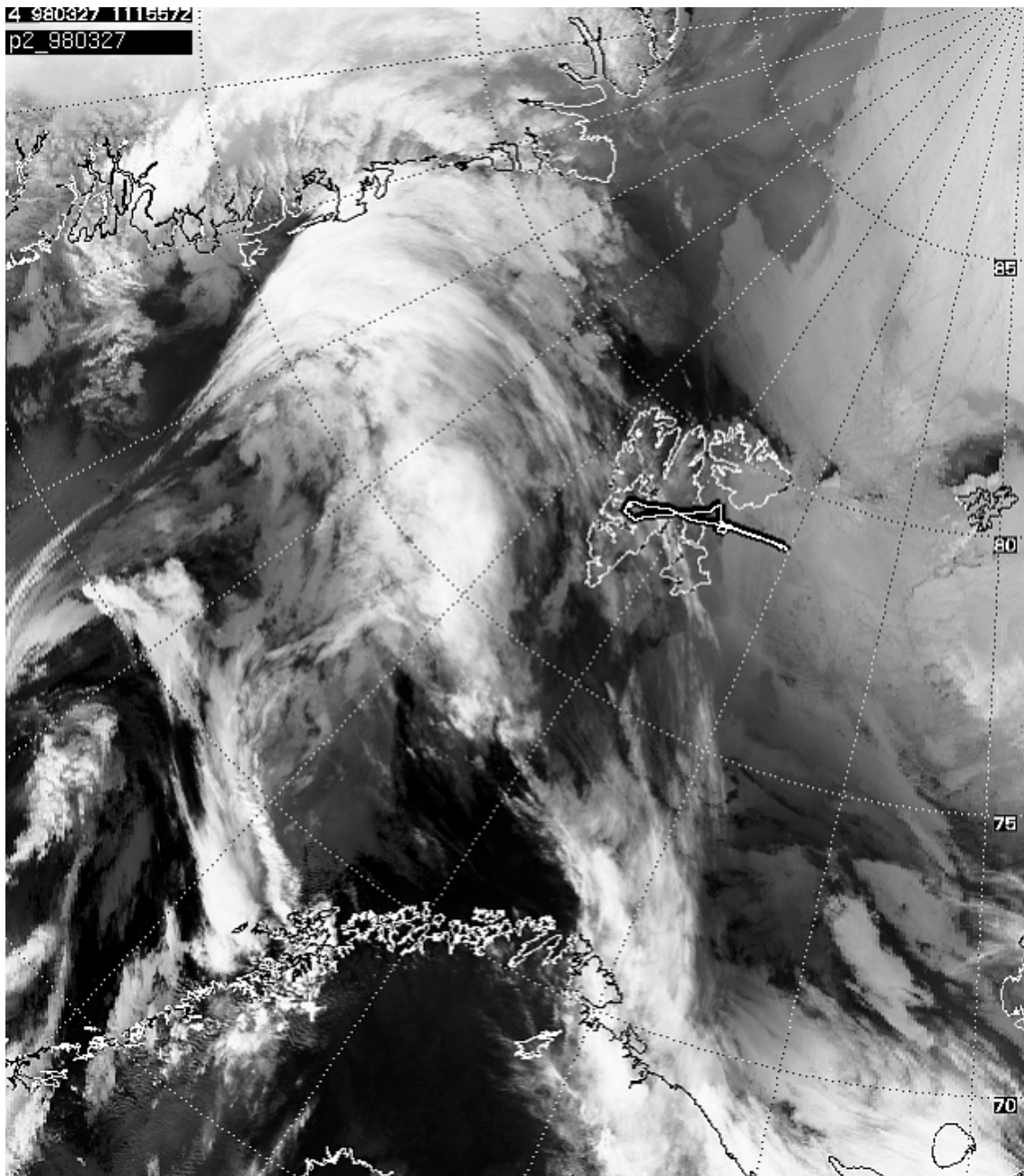


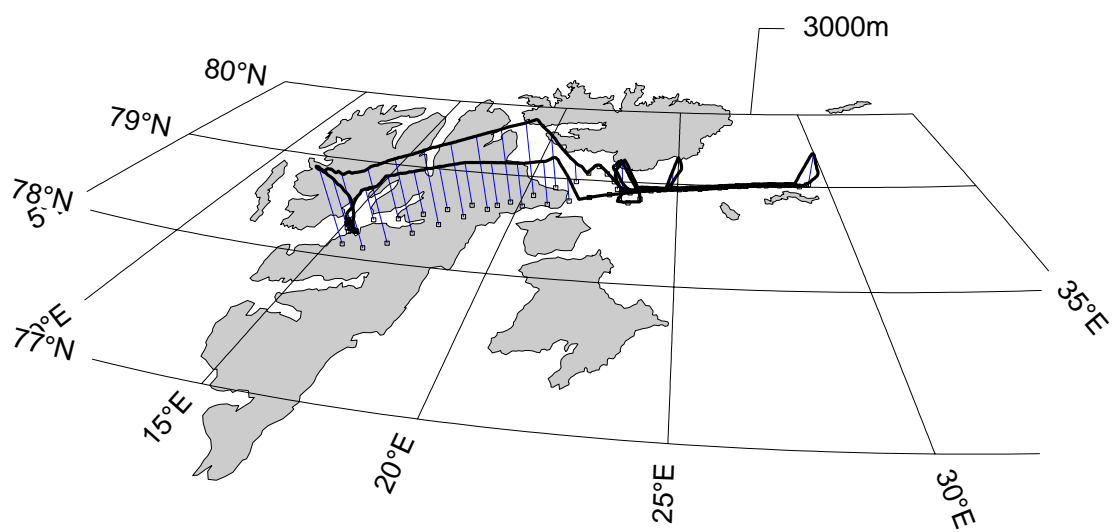
**27 March 1998**

On the north-eastern side of a low pressure system Svalbard was situated in the warm air sector with strong easterly to south-easterly winds prevailing. The strong wind was due to further increasing high pressure north-east of the island. Altocumulus lenticularis were visible over Spitsbergen during the day.

**Polar 2:** Polar 2 flew in the east of Spitsbergen between Kong Karls Land and Nordaustlandet over reasonable rough ice several times a 100 km long flight leg at very low altitude. The leg was oriented parallel to the wind direction.

**Polar 4:** No flight.





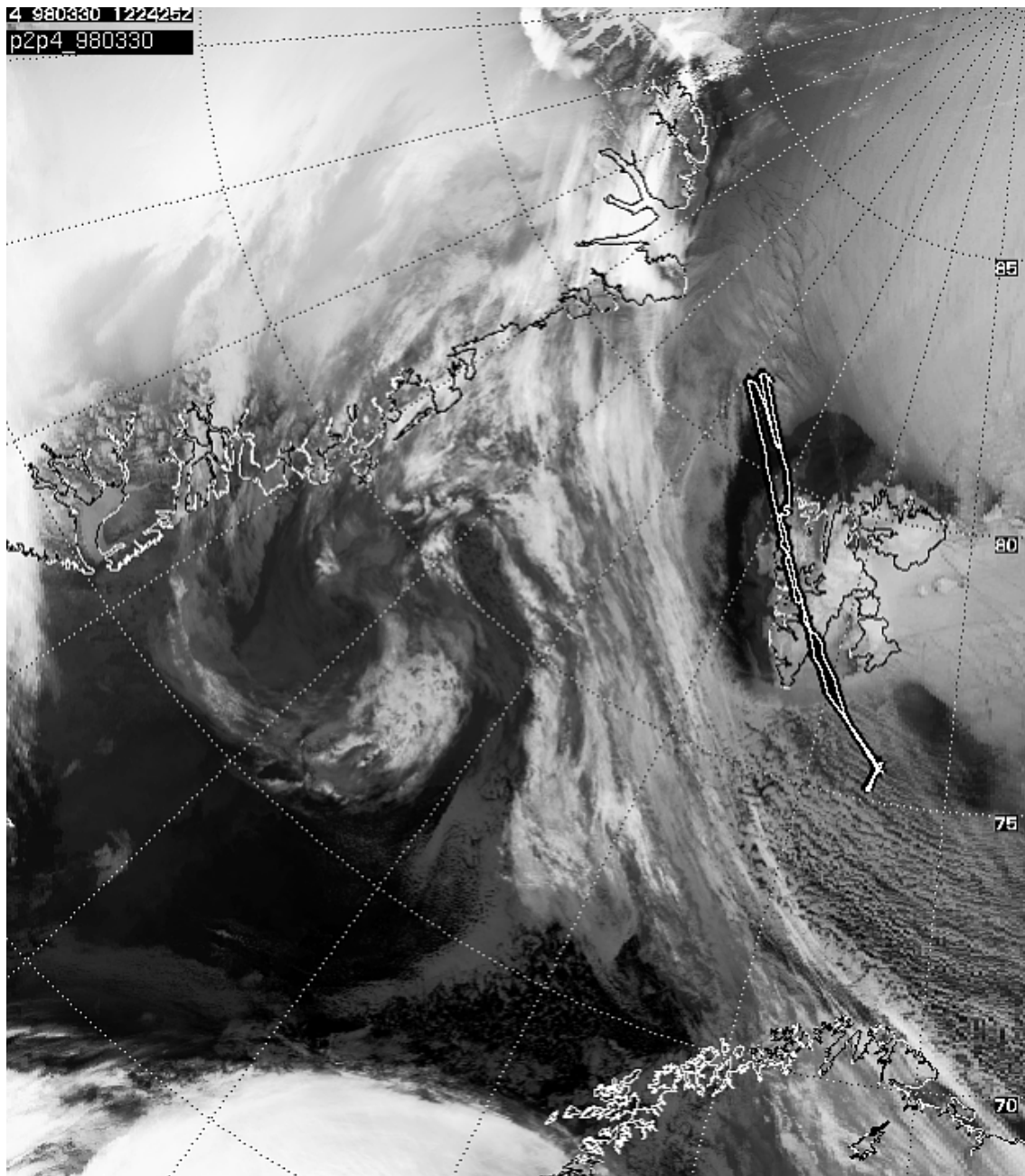
Polar2 1998-03-27

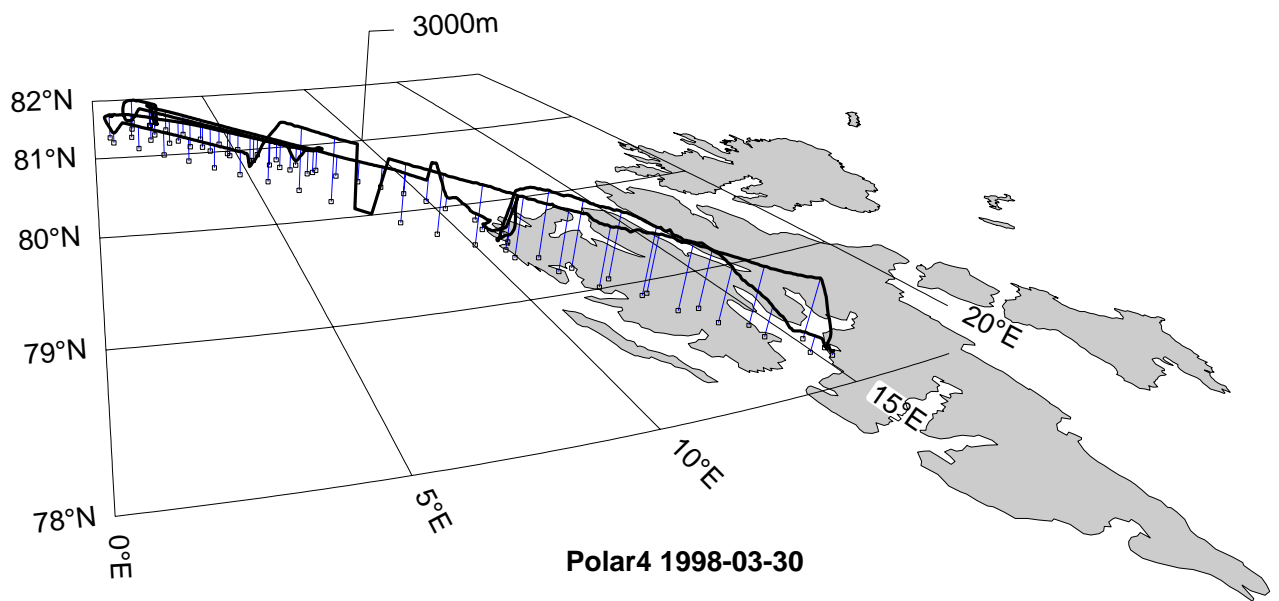
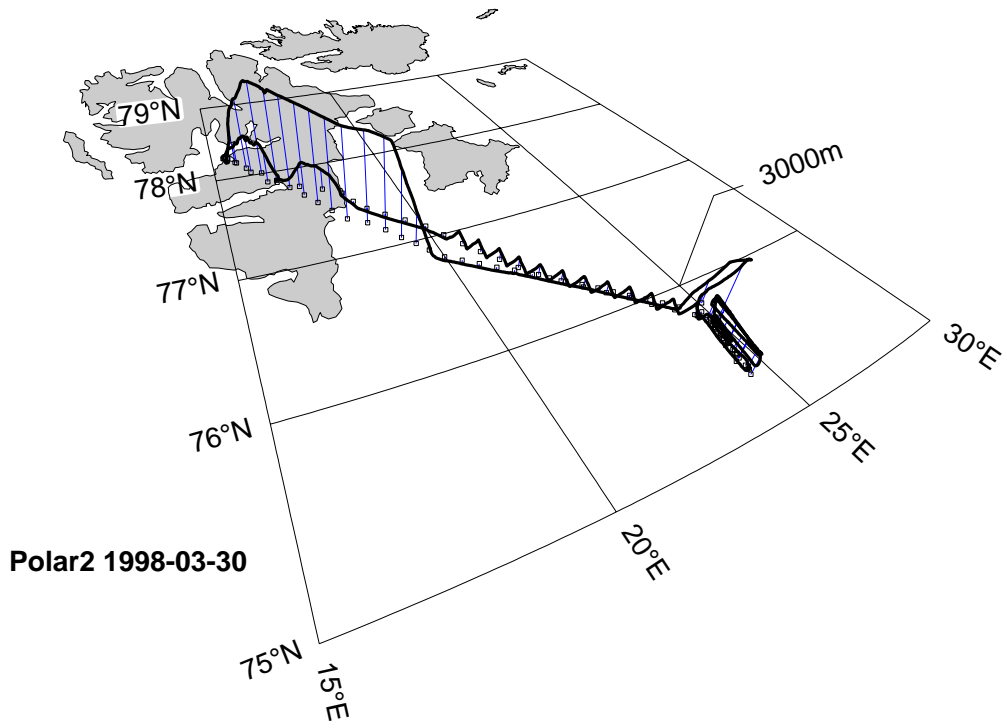
**30 March 1998**

The high-pressure cell in the north east of Svalbard was now centred over Franz-Josef-Land and had a core pressure of 1044 hPa. The low-pressure system in the Greenland Sea was situated north of Jan Mayen with a core pressure of 995 hPa. This led to a strong south-easterly wind south of Svalbard and to moderate southerly winds north of the islands. Similar to the situation on March 14 cold air was blowing over the Barents Sea towards Svalbard. Cloud streets developed with an east-west orientation.

**Polar 2:** Flux profile measurements in convection. Polar 2 flew a stack of 7 cross-flow legs of 25 NM length south of Spitsbergen.

**Polar 4:** Remote sensing mission north-west of Svalbard, centred at 81°N 4°E: descent, ascent, 4 parallel legs of 100 km length at 500 m height.





### 31 March 1998

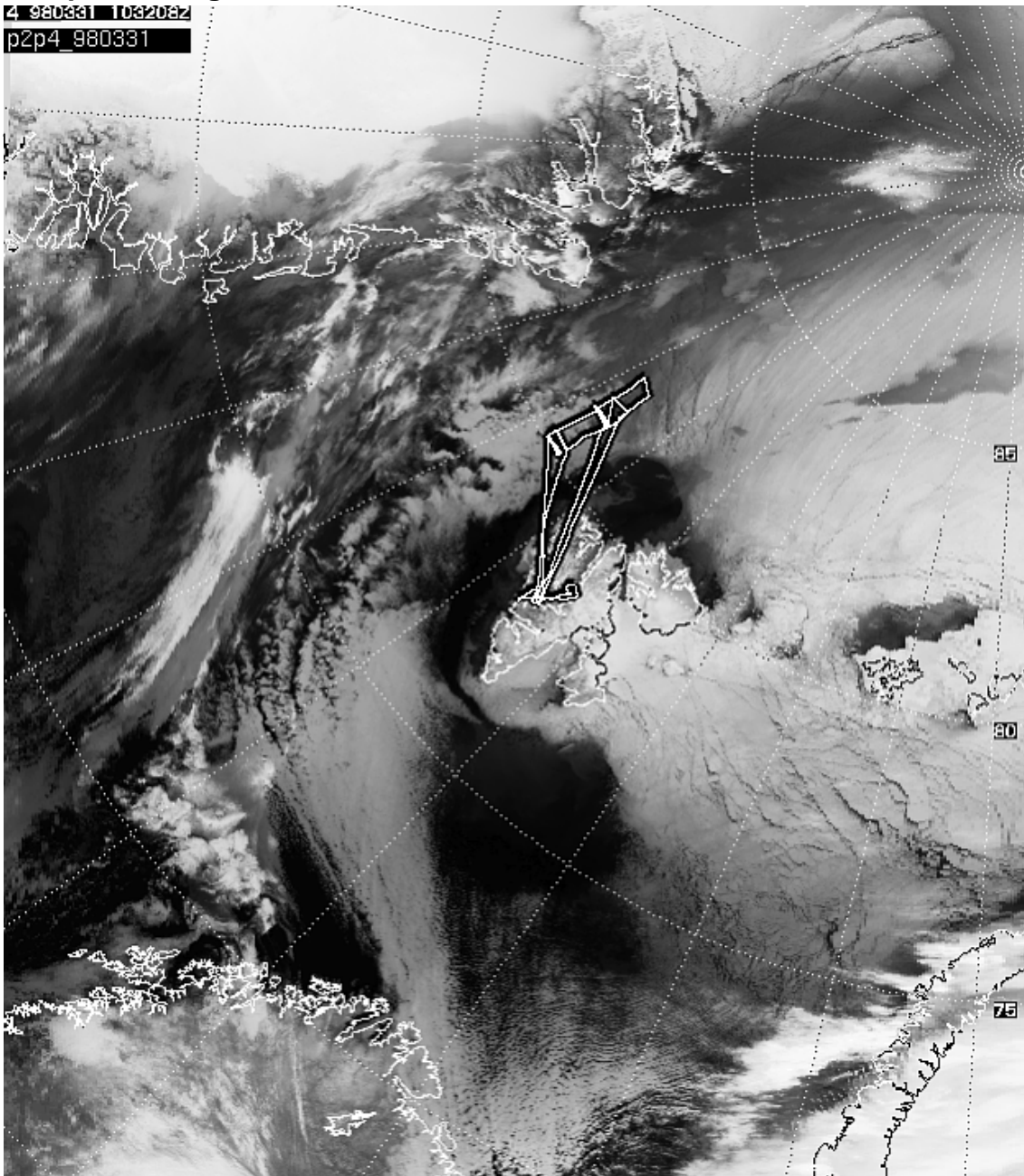
The high-pressure cell over Franz-Josef-Land remained stationary but its core pressure decreased to 1035 hpa. With a weak low north of Greenland a southerly wind resulted in an on-ice flow in the Fram Strait. Both aircraft flew in a coordinated mission stacks of cross-flow legs at various distances from the ice edge.

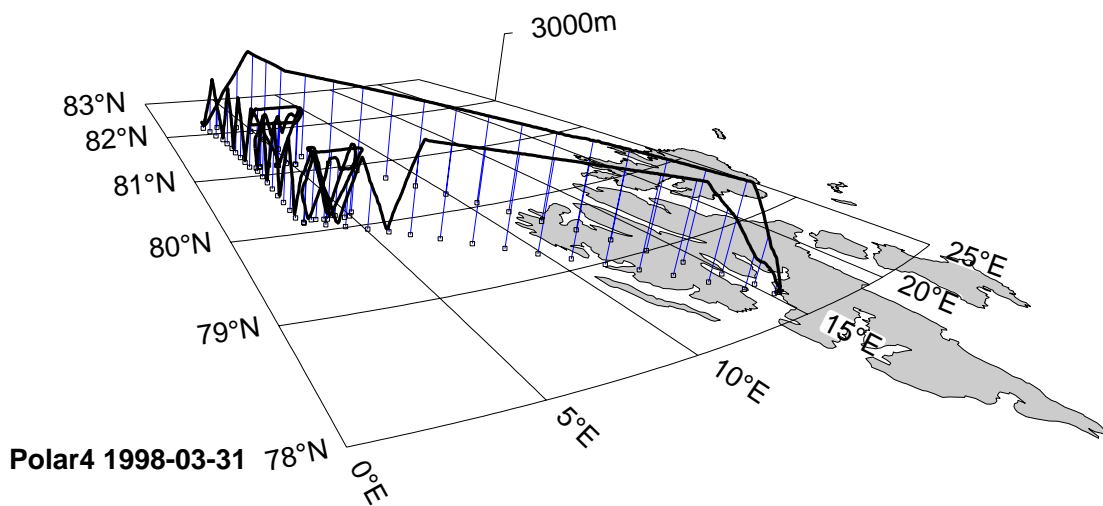
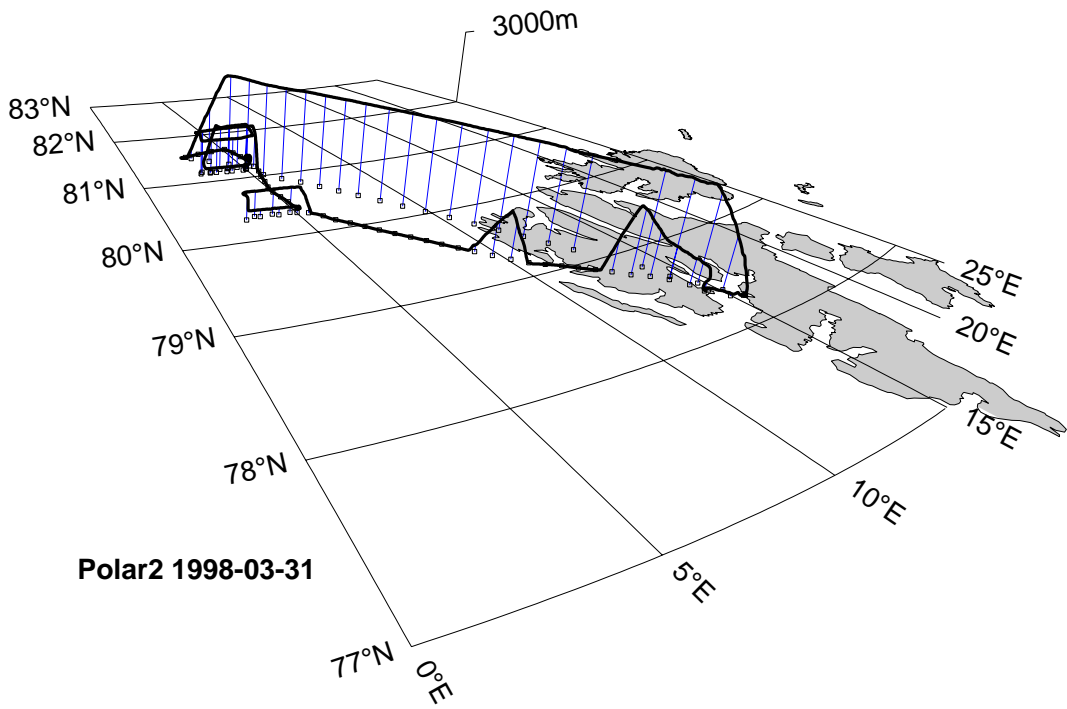
**Polar 2** Descent over the ice, low southbound flight, stack of 4 legs at 50 km north of the ice edge, stack of 2 legs at 50 km south of the ice edge, flight trough Kongsfjord.

**Polar 4:** As Polar 2, but 4 legs in the southern stack and passing of Ny-Ålesund at 3000 m.

### Comparison flight

4 980331 103208Z  
p2p4\_980331



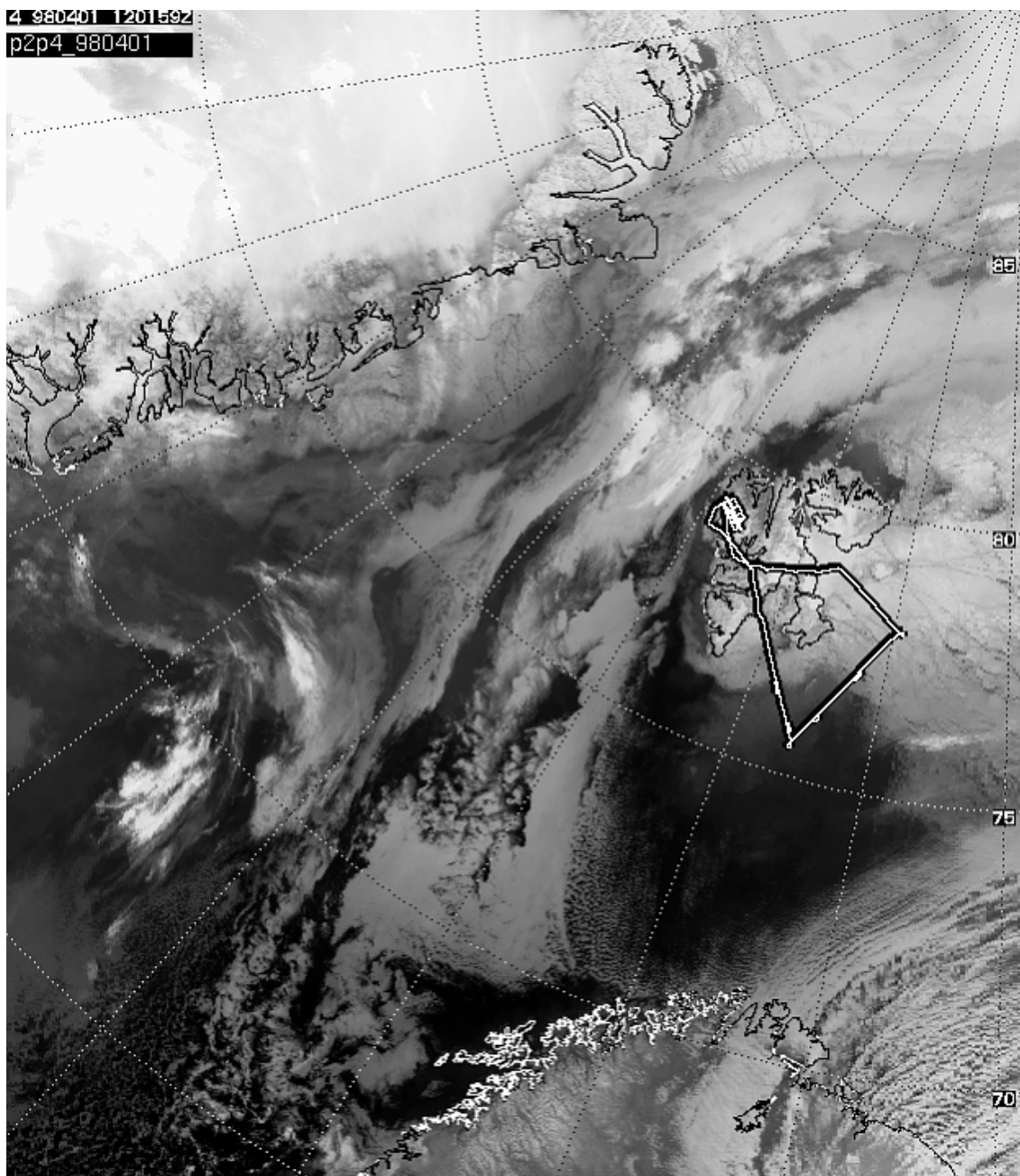


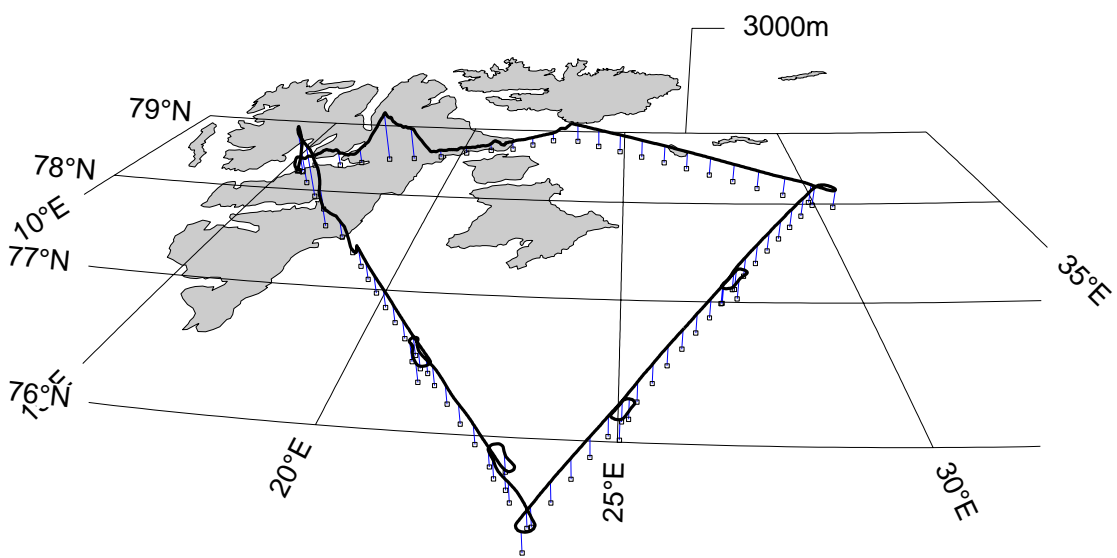
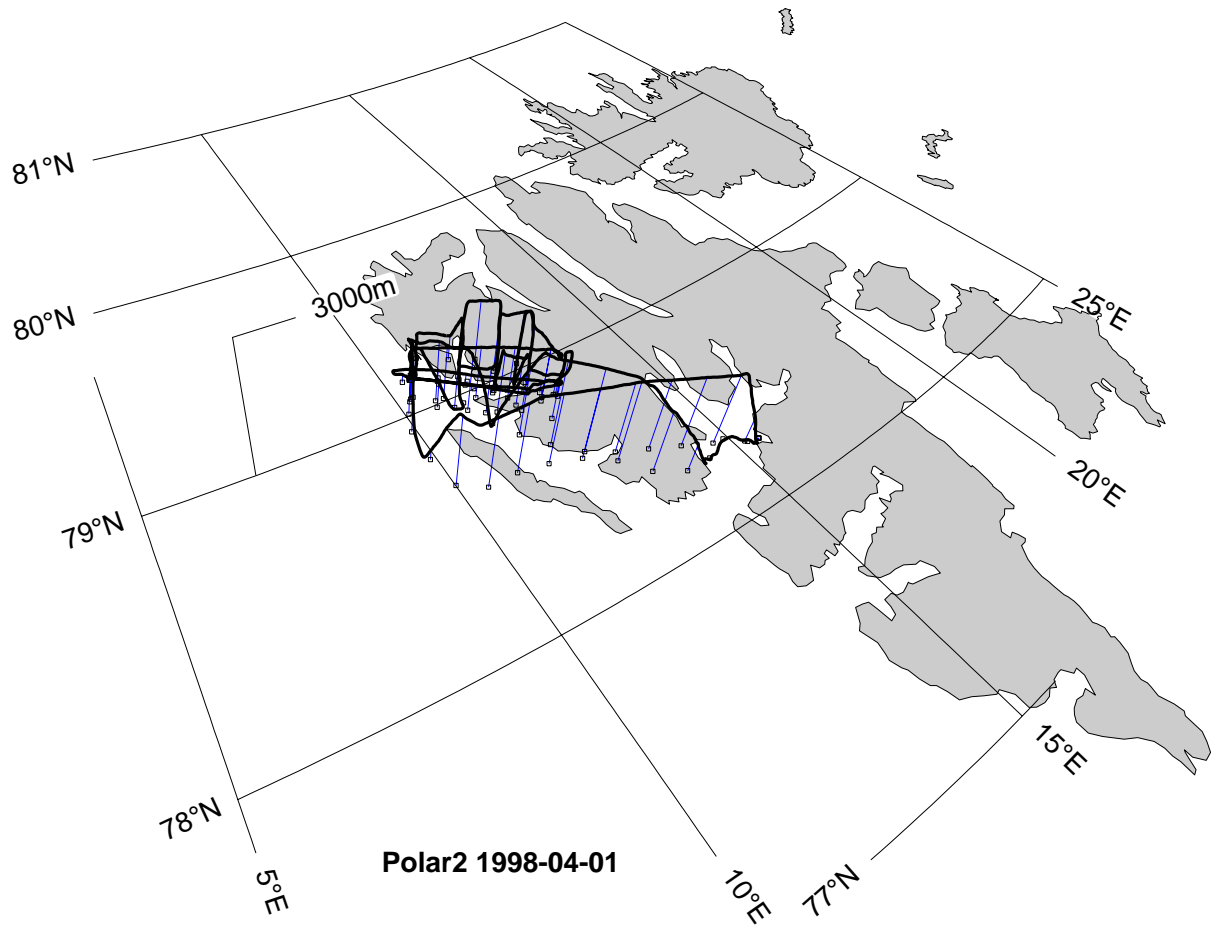
**1 April 1998**

The on-ice flow situation over Fram Strait continued, but the pressure further gradient decreased. A weak front approached Svalbard from the south-west and brought some snowfall in Ny-Ålesund in the evening.

**Polar 2:** The entire flight was used to measure the flow pattern in Kongsfjord in Ny-Ålesund.

**Polar 4:** Polar 4 used the cloud free situation in the south-east of Svalbard to fly long legs across extended areas of pancake ice for remote sensing.





**Polar4 1998-04-01**

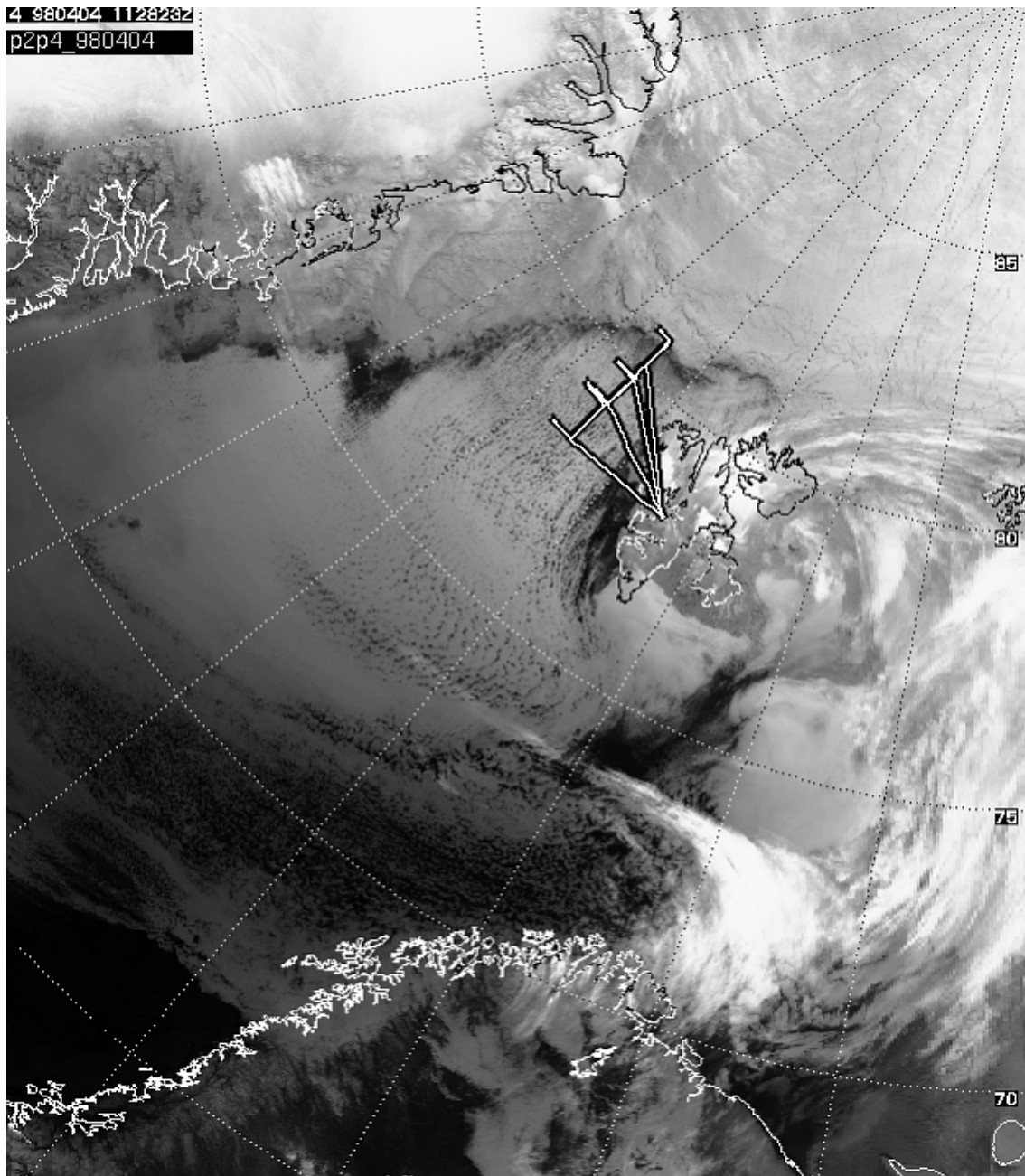
#### 4 April 1998

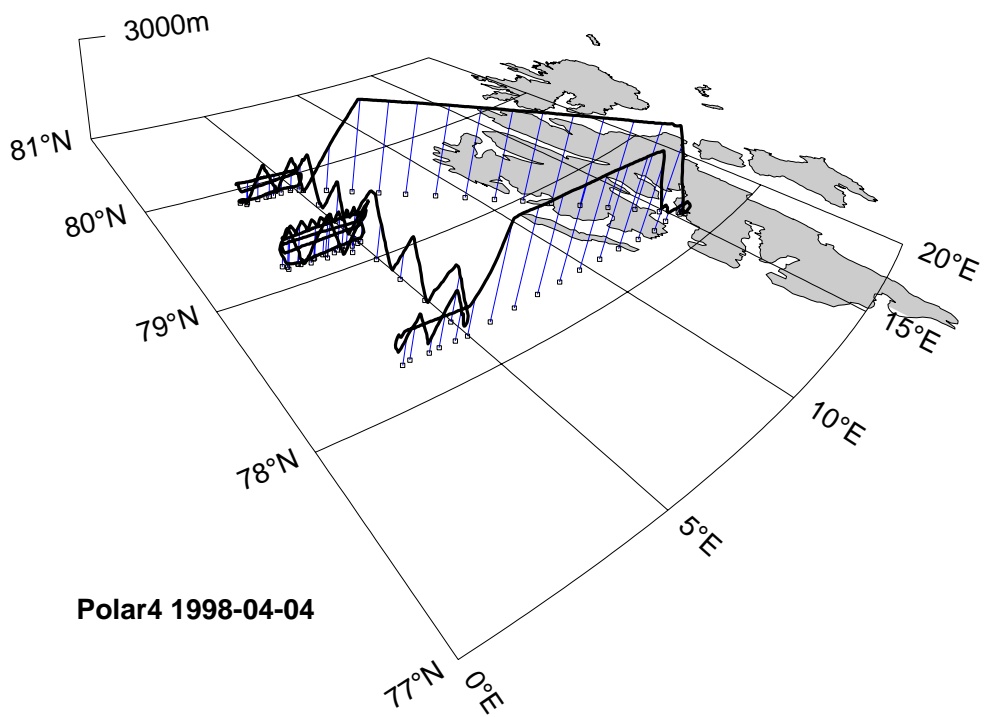
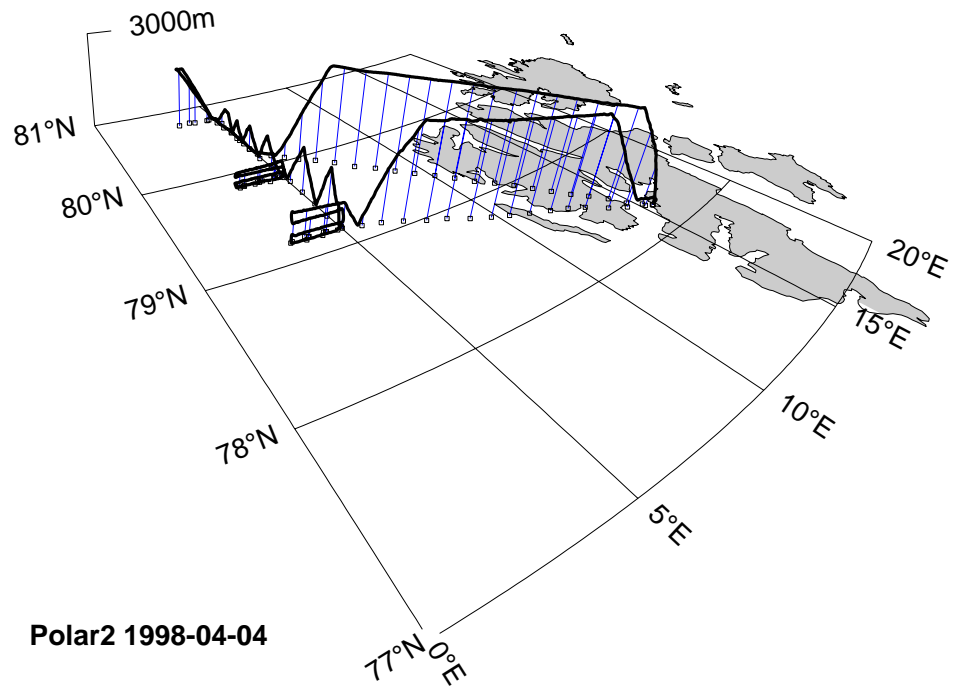
A low pressure system east of Svalbard and high pressure over Greenland resulted in a typical cold air outbreak situation over Fram Strait. The surface wind speed was 15 to 17 m/s.

Both aircraft flew a coordinated mission along the 5<sup>th</sup> meridian in the developing boundary layer. Stacks of cross-flow legs and saw-tooth pattern along the wind direction were flown.

**Polar 2:** Ascent and descent over the ice, low southbound flight over the ice, 2 stacks of 4 legs each over the water.

**Polar 4:** 3 stacks with 4, 6 and 2 legs, some legs as saw-tooth pattern.





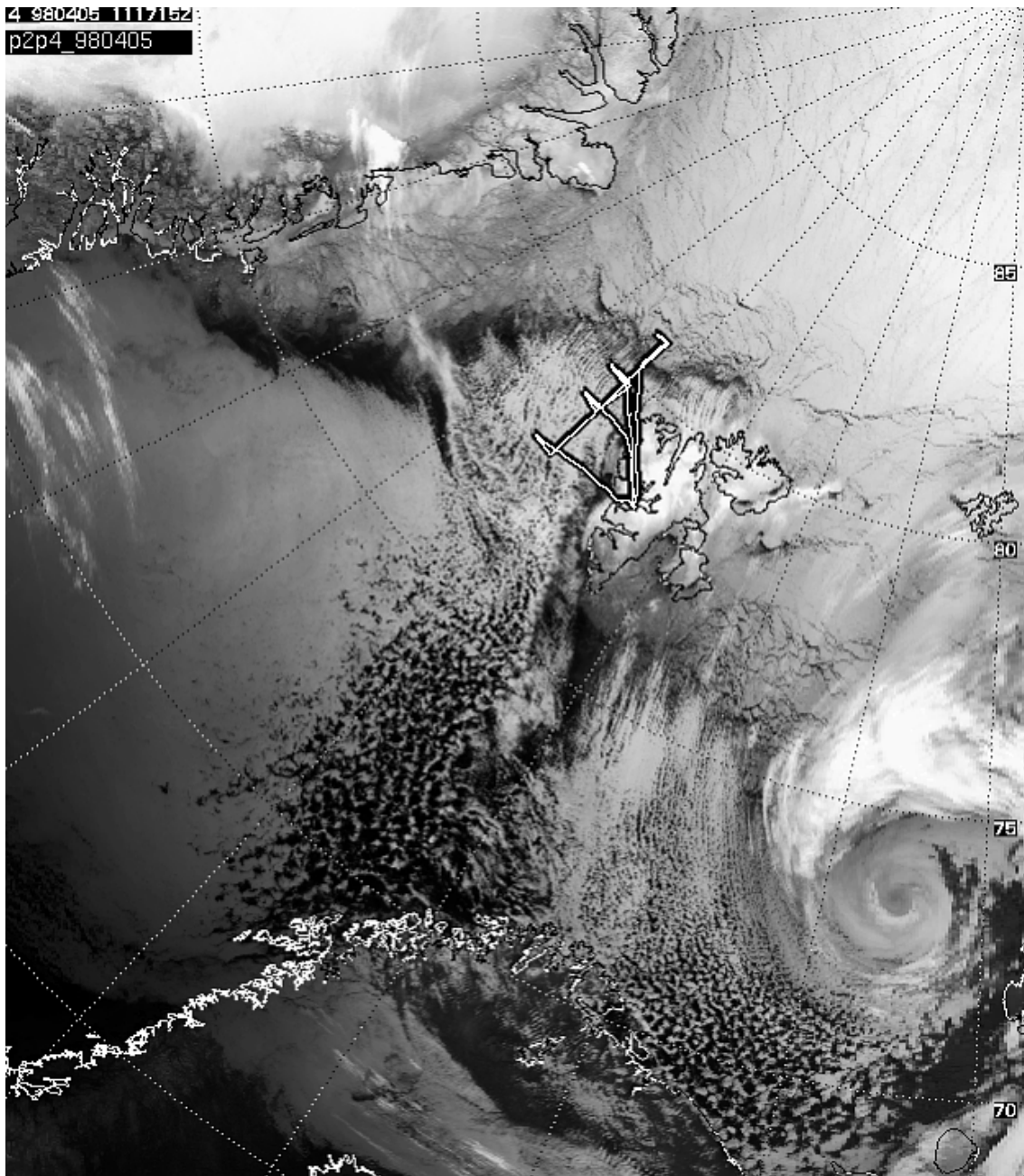
## 5 April 1998

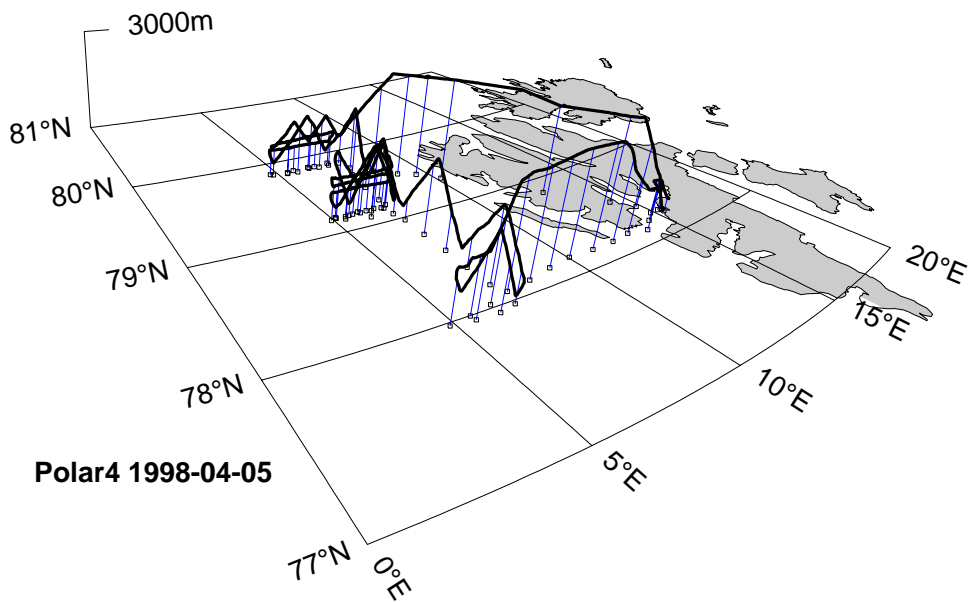
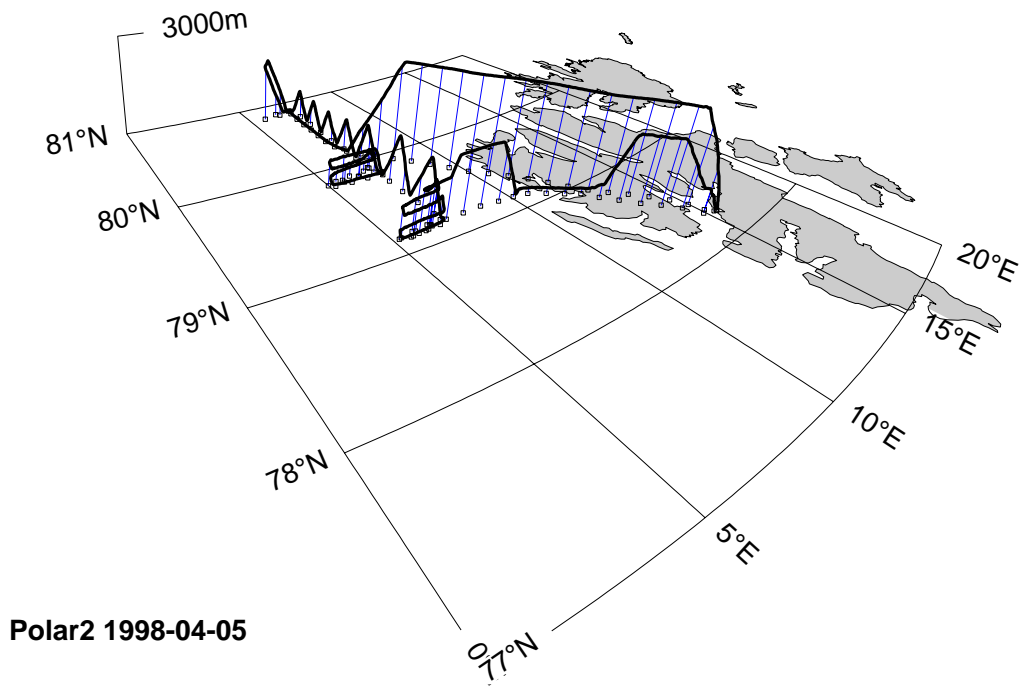
The cold air outbreak continued with little change in the synoptic situation.

Again both aircraft flew a coordinated mission, this time oriented along the 7<sup>th</sup> meridian.

**Polar 2:** Ascent and descent over the ice, low southbound flight over the ice, 2 stacks of 4 legs each over the water at 50 km and 100 km south of the ice edge.

**Polar 4:** 3 stacks with 4, 5 and 2 legs, some legs as saw-tooth pattern, at 50 km, 100km and 200 km south of the ice edge.



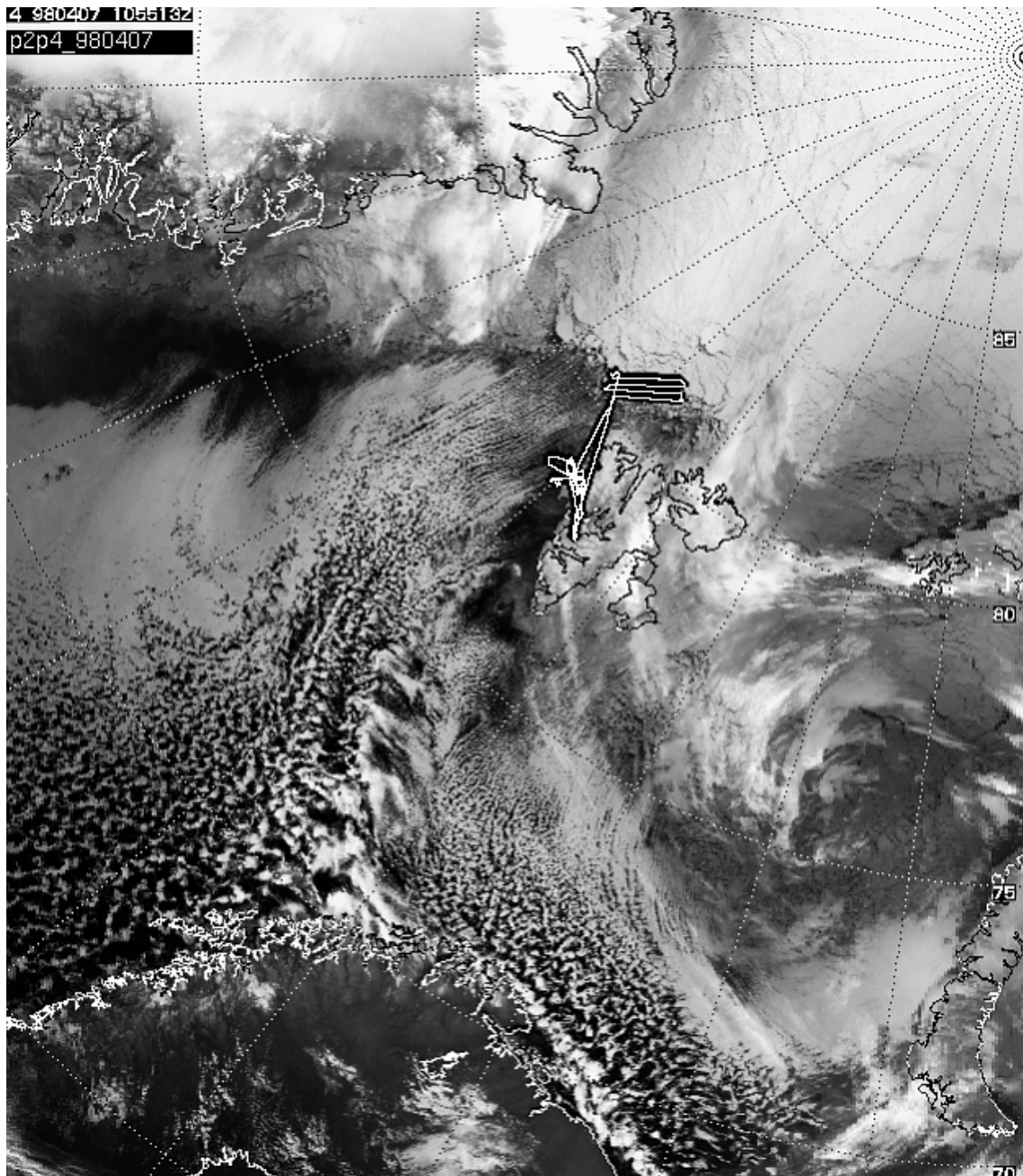


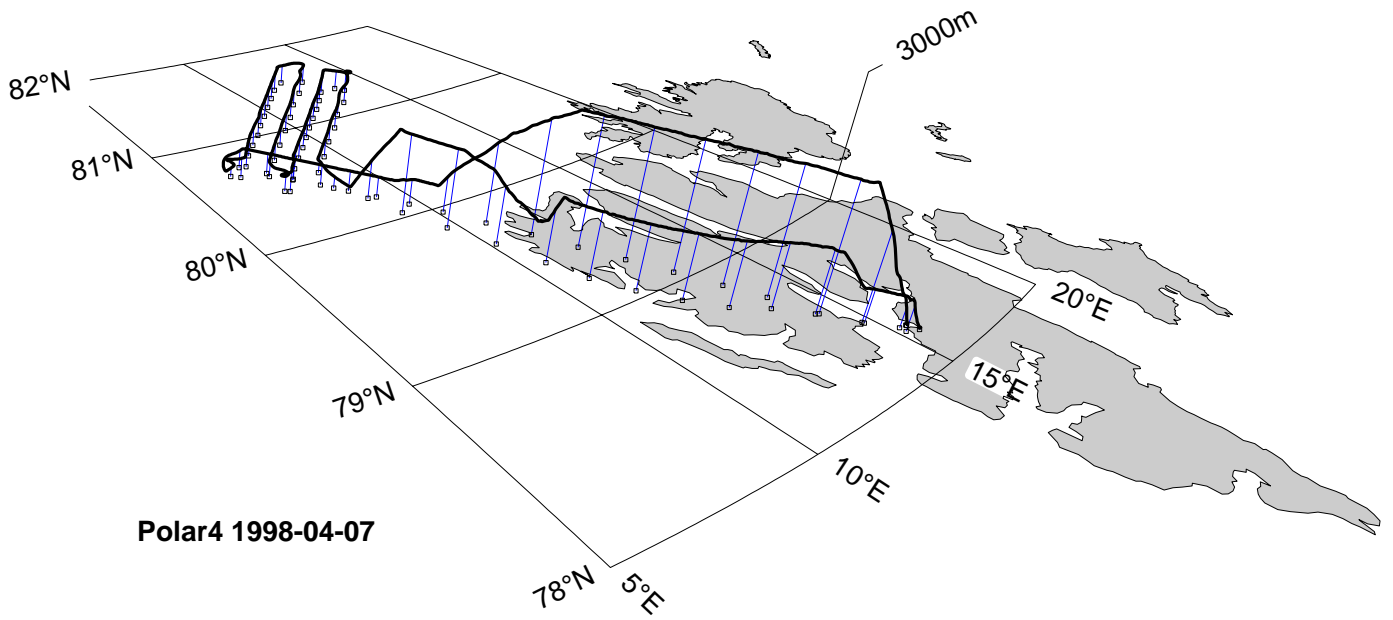
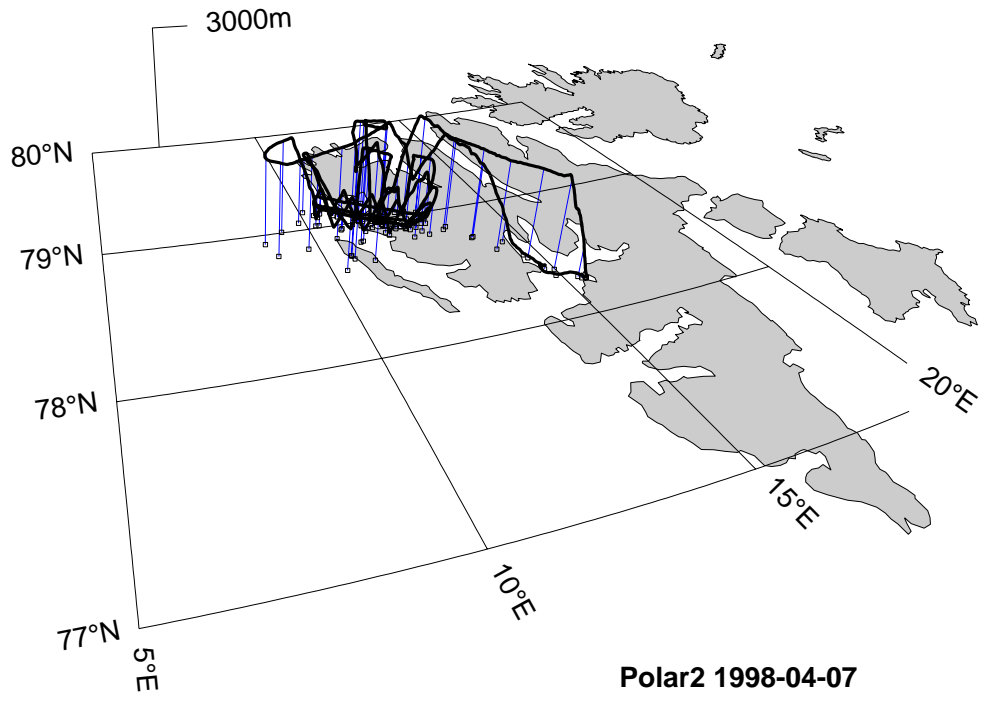
**7 April 1998**

The northerly airstream continued, but with an increasing easterly component.

**Polar 2:** Various legs over Kongsfjord to measure the flow pattern around Ny-Ålesund.

**Polar 4:** Remote sensing in the north west of Svalbard. 4 parallel legs of 115 km length were flown at 500 m height near 81°N, 10°E.



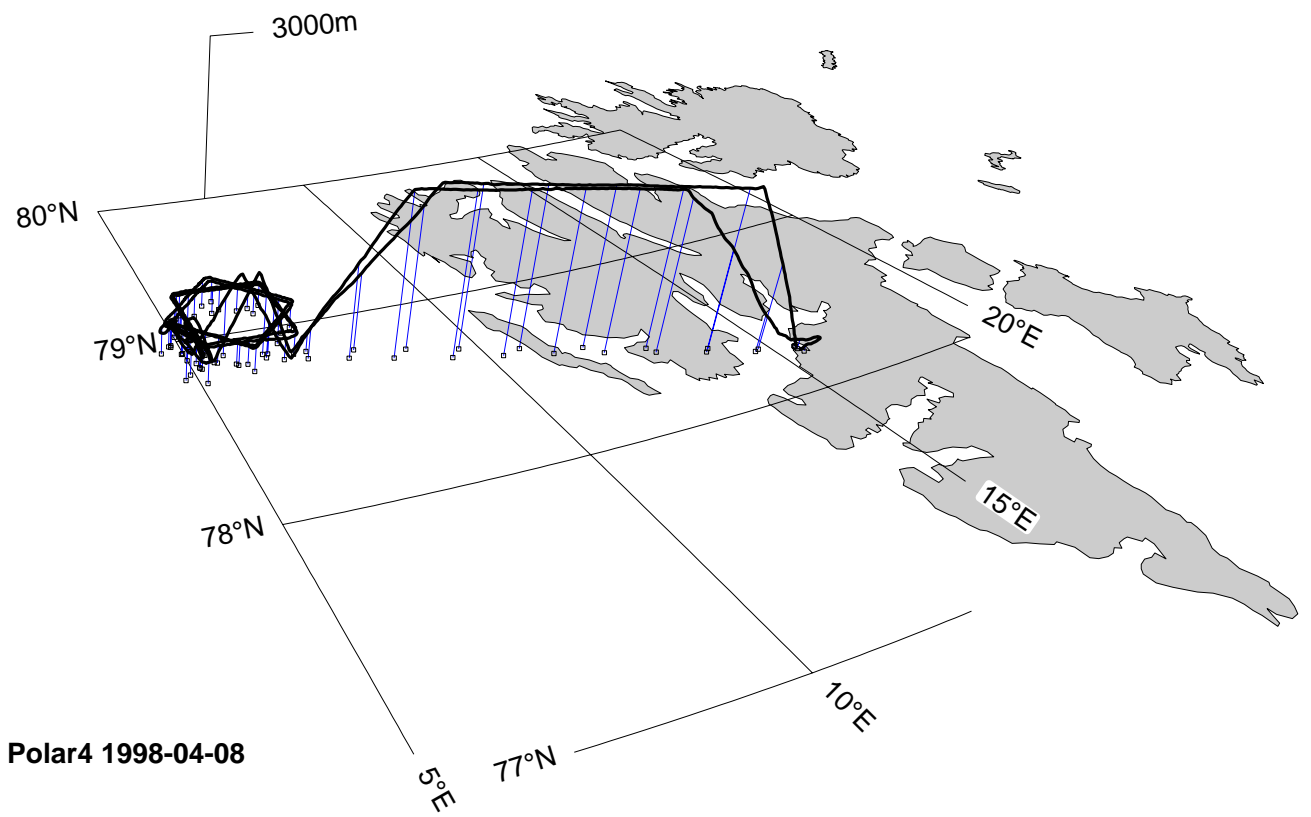
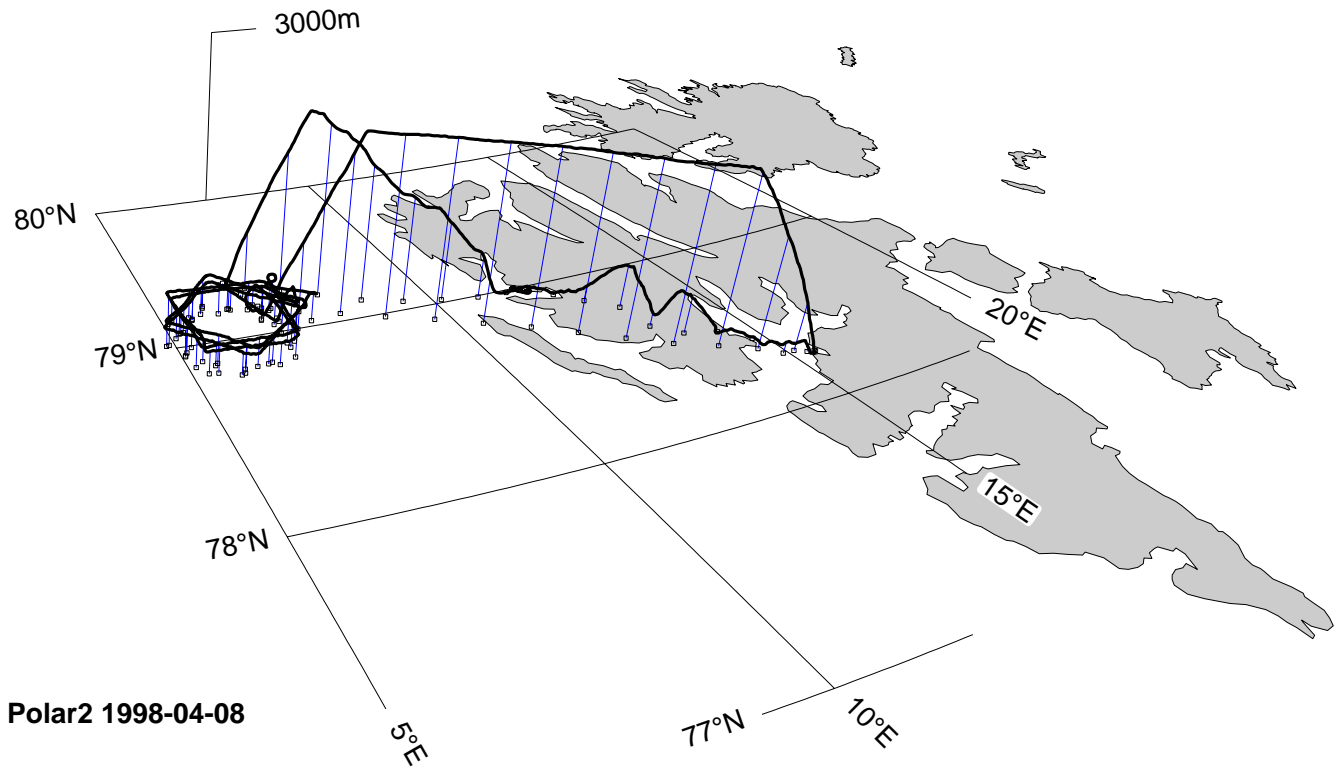


**8 April 1998**

The northerly airflow with a convective boundary layer over the Greenland Sea still continued.

Both aircraft flew vertical soundings and circled a square pattern of 20 NM by 20 NM size at two heights (400 m and 500 m) and two orientations. The square was centred at 79°N, 6°E. The first flight level was in the lower third of the cloud, the second level in the upper third. The cloud coverage was 6/8. Polar 4 circled the pattern 180° ahead of Polar 2.





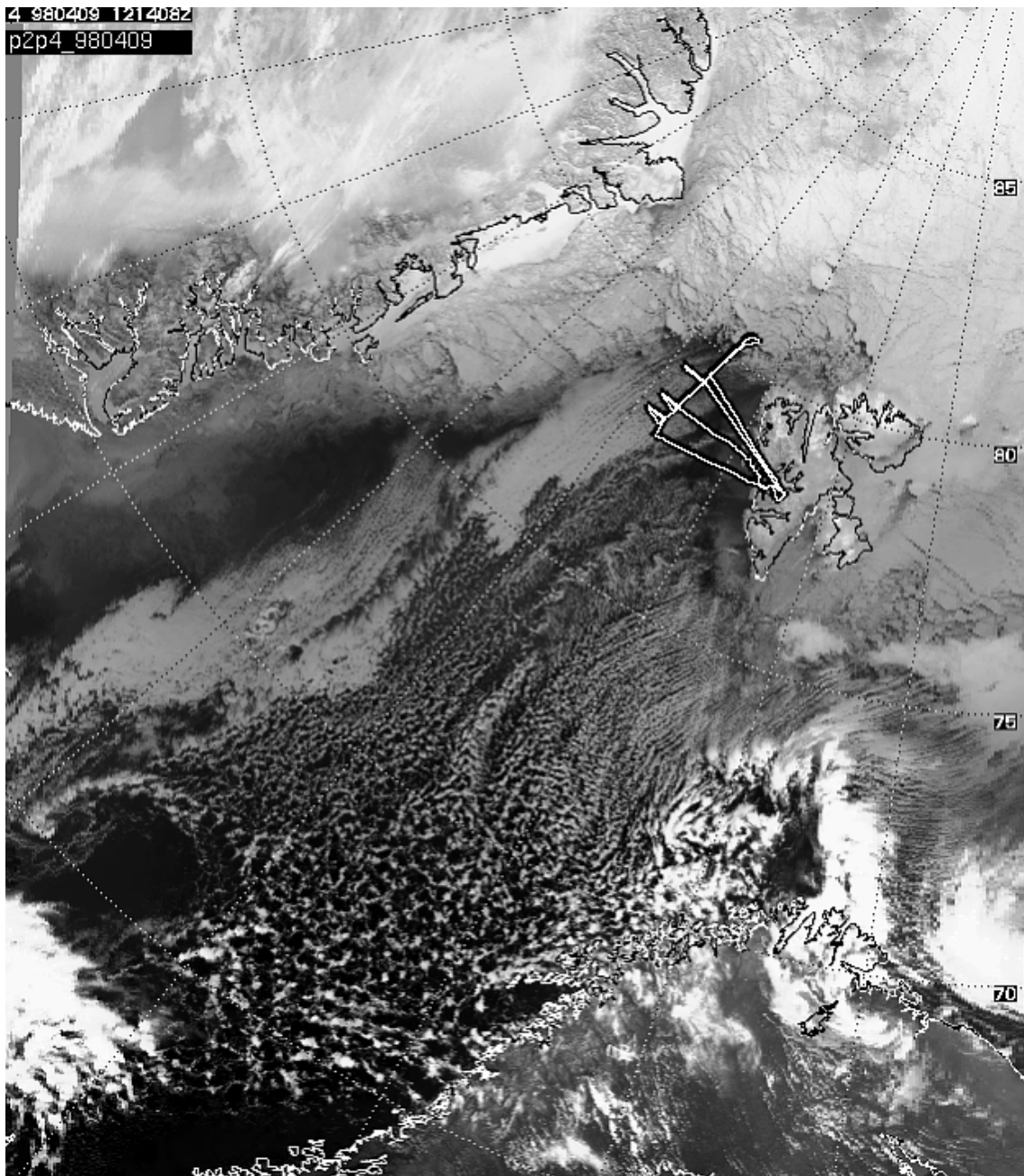
**9 April 1998**

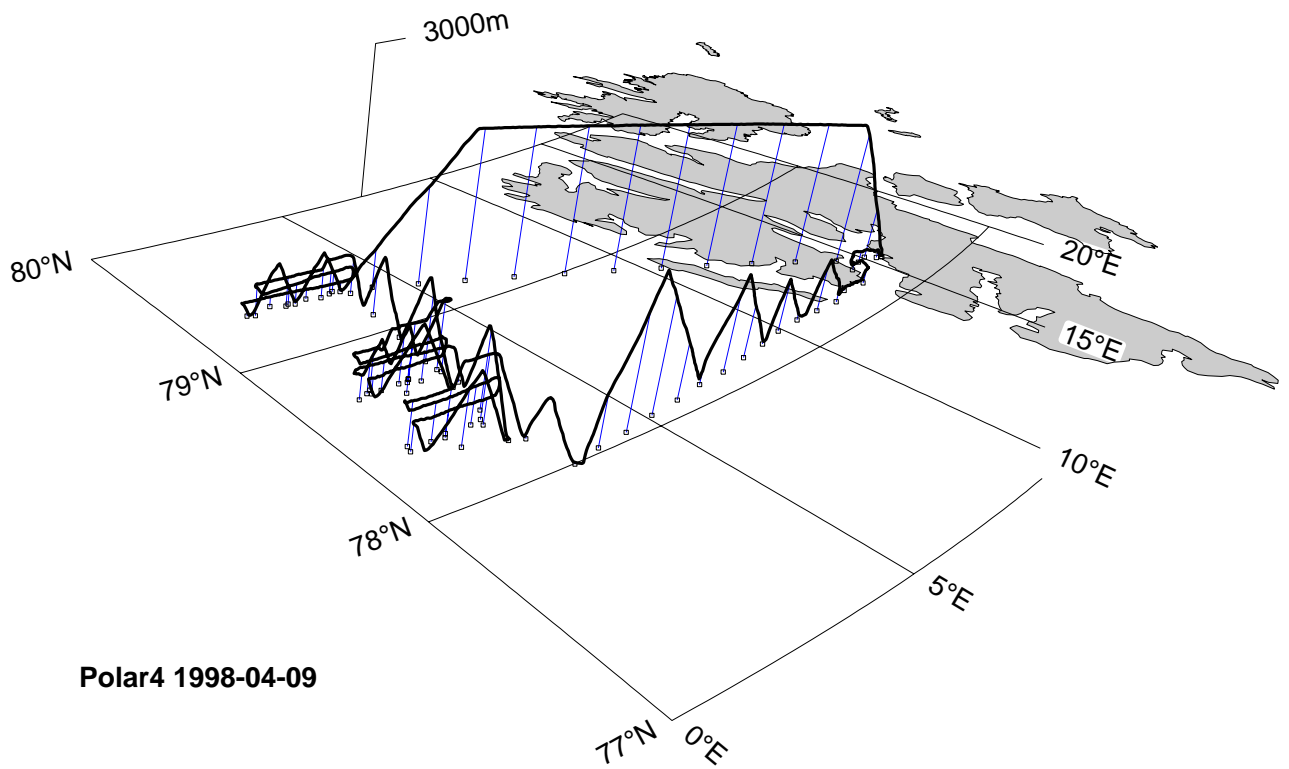
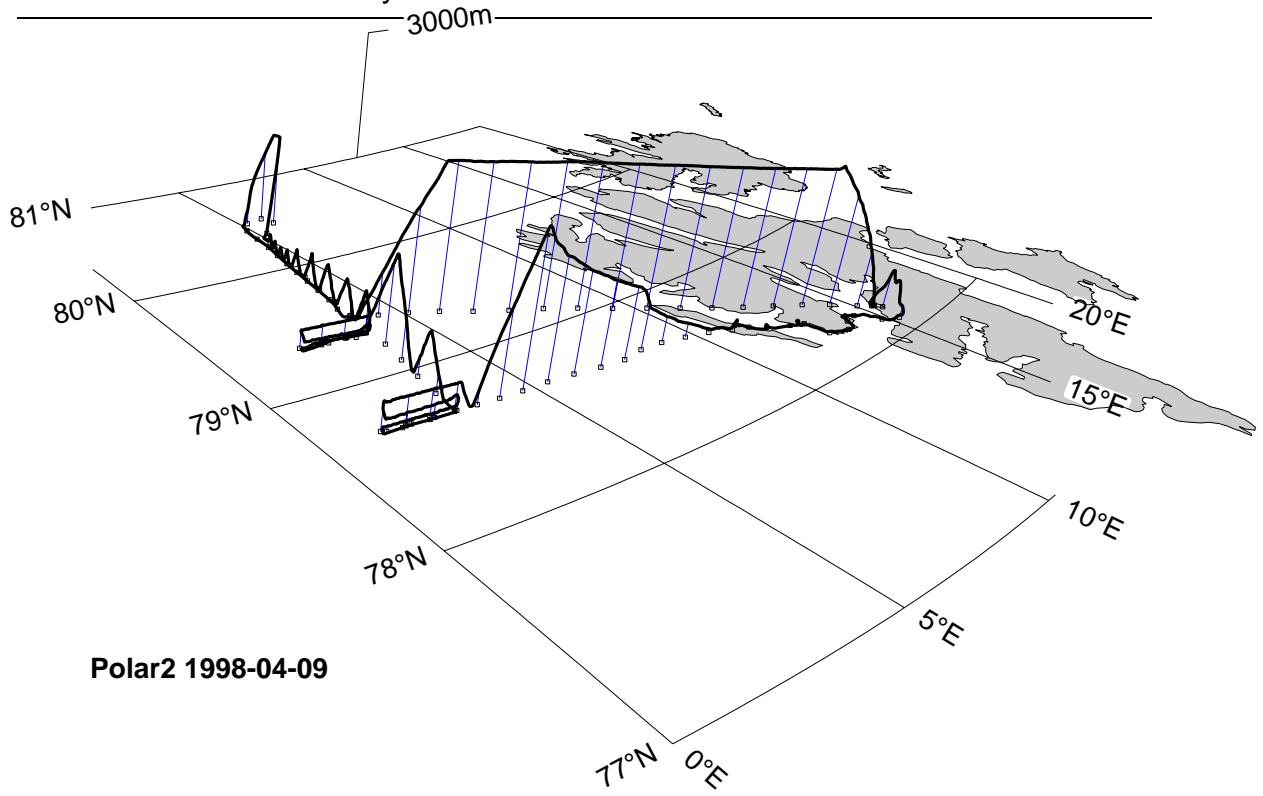
The low pressure system over the Barents Sea moved southwards leading to a more easterly flow component around Svalbard.

Again, both aircraft flew a coordinated mission in the developing convective boundary layer.

**Polar 2:** Northbound leg over the sea ice to  $80^{\circ}\text{N}, 5^{\circ}\text{E}$ , vertical sounding up to 2000 m height, southbound saw-tooth pattern and cross-flow legs at 50 km and 100 km distance south of the ice edge.

**Polar 4:** Three stacks of cross-flow legs at 50 km, 100 km and 150 km distance south of the ice edge. Saw-tooth pattern between the cross legs and to  $78^{\circ}\text{N}$ .



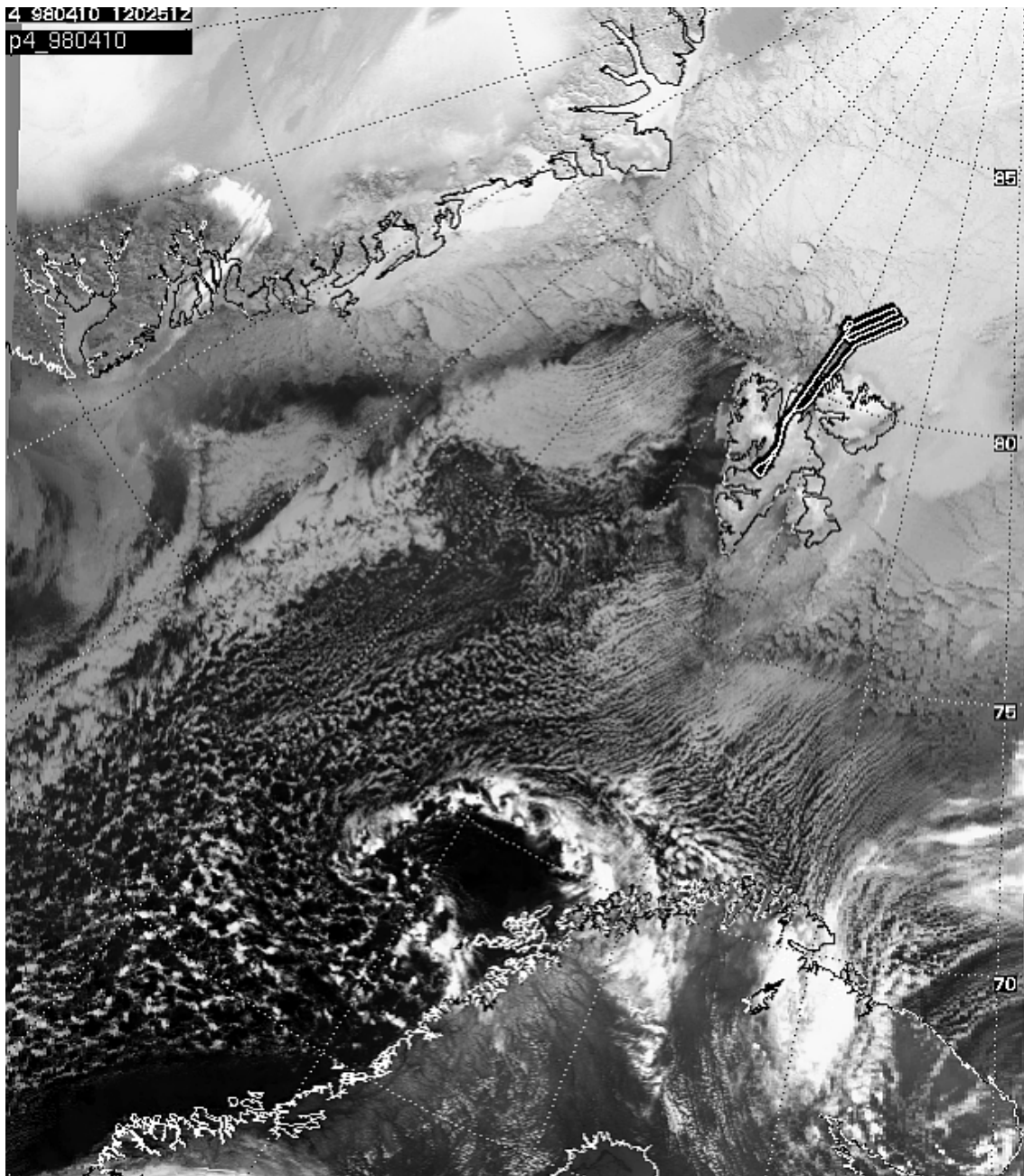


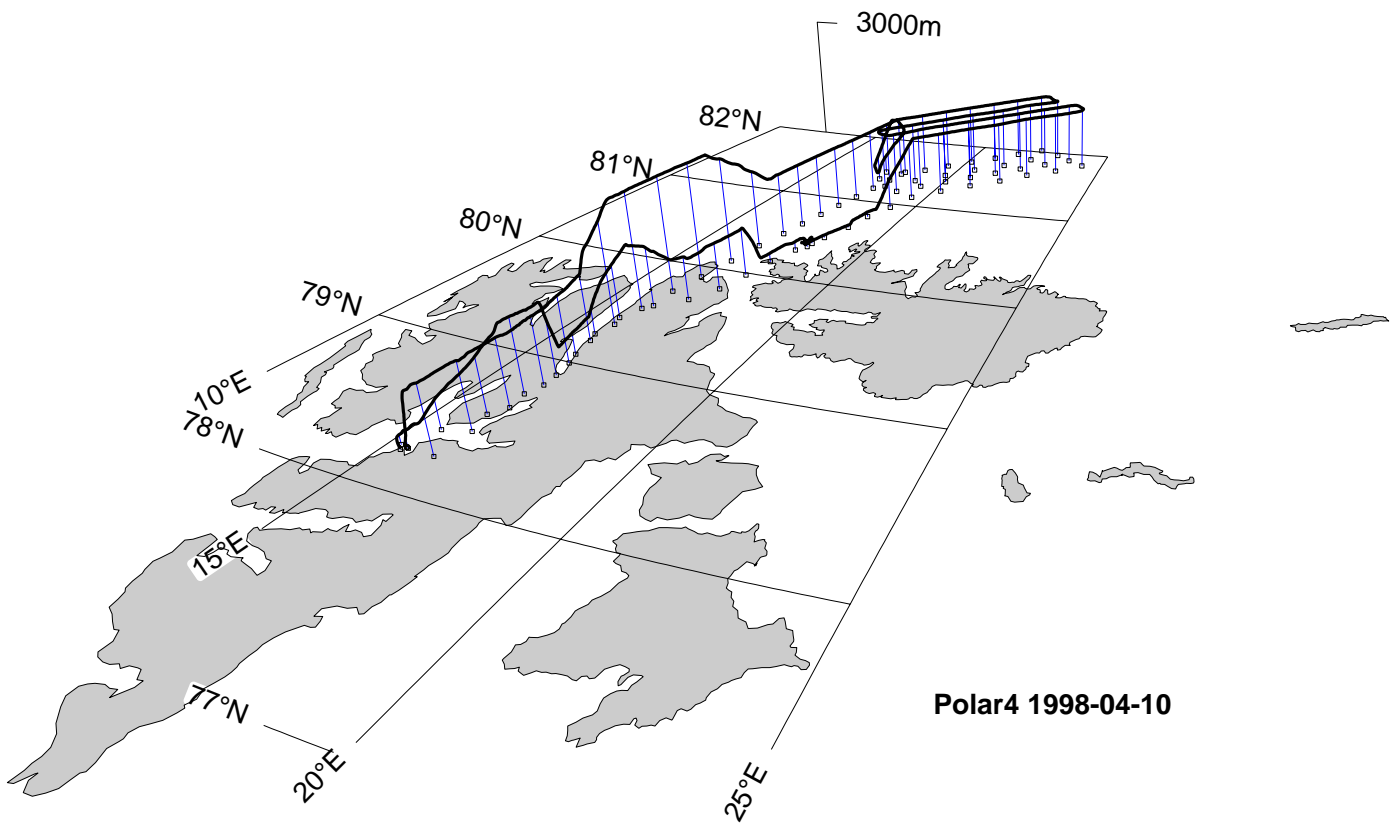
**10 April 1998**

A large low-pressure system at the northern coast of Norway and high pressure over Greenland forced north-easterly winds in the region of the measurements, north of Svalbard. Low clouds only formed over the water.

**Polar 2:** No flight.

**Polar 4:** In the last mission of the field campaign Polar 4 flew a remote sensing pattern at a height of 1500 m.





### 3.3. Ground based measurements at Ny-Ålesund

Ground based measurements at Ny-Ålesund were conducted from 15 March to 16 April, 1998. Until the end of March the atmospheric conditions were quite variable, the wind speed mostly exceeded 10 m/s, and several snow storms occurred. From March 31 until the end of the field work, good weather conditions and low wind speed prevailed. Due to the unfavourable weather during the first period logistical difficulties in installing the instrumentation and launching the tethered balloon occurred. For this reason the measurements started only on March 19.

#### 3.3.1. Sodar and tethersonde

From the Sodar the following raw data are available:

- Instantaneous data. These data (1 day = 200 Mb) were digitally recorded in real time to be processed off-line.
- Radial velocity along the axes of the three antennas (ch1-ch2-ch3). Each antenna is associated with one channel (ch1, ch2, ch3, corresponding to the beam along the Y, X and Z axes, respectively).

The processed data will provide:

- vertical profiles of the horizontal and vertical velocity components
- the variance of the vertical velocity at various height levels
- facsimile representation for the 3 channels

The Sodar data are available most of the time during the field experiment (Table 3.3). A lack of data is generally due to low signal to noise ratio occurring in presence of very strong winds, or during snow storms. For the same reason the height range of the measurements decreased since the signal became too weak. The absence of the signal may also be attributed to very low thermal fluctuations. In Figure 3.2 a scatter plot of the maximum height for each 10 minute sounding is given as a function of time. From the tethersonde, vertical profiles of temperature, humidity, wind speed and direction are available.

#### 3.3.2. Sonic anemometer and radiation

The sonic anemometer data cover the period from March 19 to April 14. Some technical problems on March 22, April 1, April 2, April 3 generated some gaps in the data set. The radiation data set reaches from March 19 to April 14 without any data loss. It is worthwhile to mention that the field experiment, limited to the Sodar system measurements, was extended in the frame of an LSF (Large Scale Facility) support until September 15.

**Table 3.3:** Inventory of available Sodar and thetersonde data during the ARTIST field experiment (19 March-16 April). Note that the time is given in local standard time (LST, UTC + 1 hour).

Date	SODAR DATA (Time)	TETHERSONDE LAUNCH (Time)
19 March	10:00-24:00	
20	00:00-24:00	16:15
21	00:00-24:00	09:45-14:15-16:55
22	06:00-24:00	
23	00:00-24:00	
24	18:00-24:00	07:14
25	00:00-24:00	
26	00:00-09:00 12:00-24:00	
27	00:00-24:00	
28	00:00-18:00	
29	NO DATA	
30	12:00-24:00	
31	00:00-24:00	12:41-13:47-15:10-17:58-19:07-19:12-21:28
1 April	00:00-24:00	06:30-09:09-12:17
2	00:00-24:00	10:18-12:50-14:51-17:04-18:56
3	00:00-24:00	08:40-09:50-13:14-17:52
4	00:00-24:00	
5	00:00-24:00	
6	00:00-24:00	05:50-09:50-13:23-17:45-18:41-19:57
7	00:00-24:00	07:54-10:01-11:15-11:50-12:55-15:42
8	00:00-24:00	17:54
9	00:00-24:00	07:00-09:07-13:40-15:49-21:00
10	00:00-21:00	07:26-10:48-14:55
11	11:00-24:00	05:45-09:04-10:40-14:17-16:26-21:08
12	00:00-24:00	08:20-09:19-09:56-15:17-19:15
13	00:00-24:00	07:06-09:53-10:27-13:41-19:52
14	00:00-07:30 10:00-24:00	10:12-10:52-13:51
15	00:00-13:00 14:00-24:00	
16	00:00-18:00 21:00-24:00	

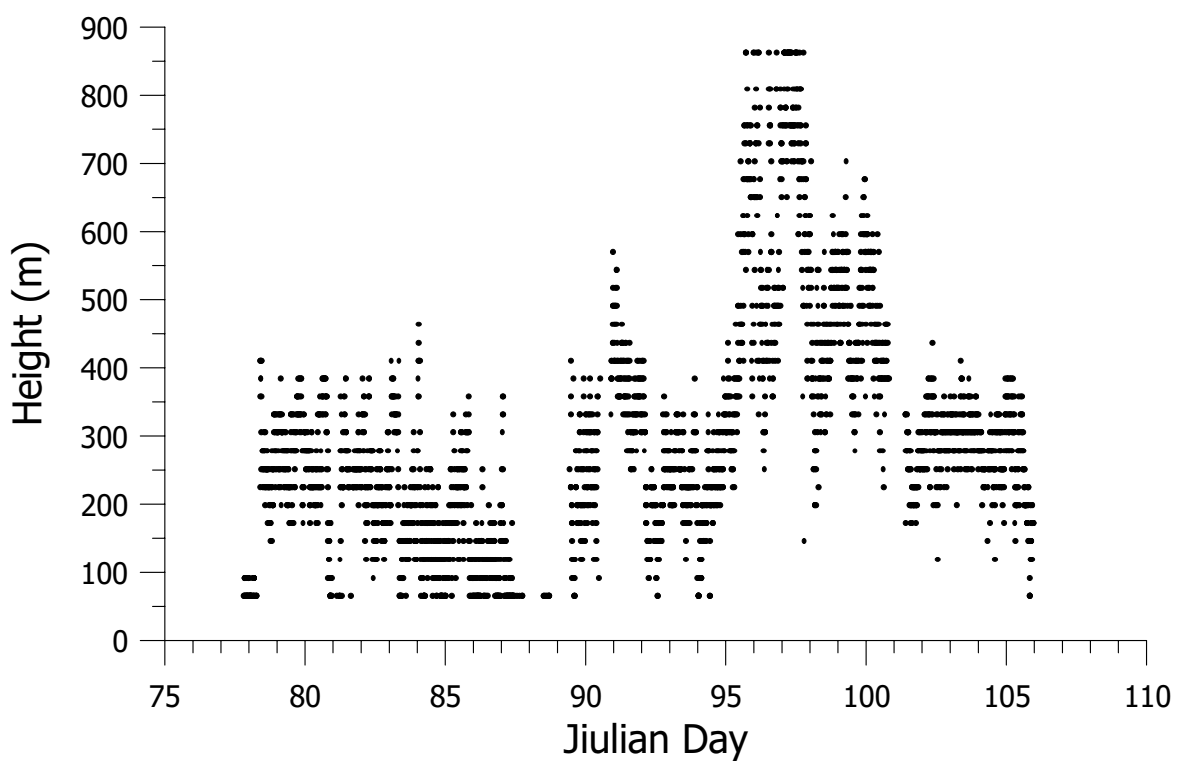


**Figure 3.2:** Height of each sounding as a function of the Julian day. Each data point refers to a 10-minutes average.

## 4. Examples of Measurements and Preliminary Results

### 4.1. Surface pressure and temperature from drifting buoys

At the beginning of the aircraft campaign an ice buoy was deployed by Polar 4 on 5 March at about 82°N 12°E. An additional four buoys, released from the research vessel Polarstern in 1996 in the Laptev sea, were drifting in the north of Fram Strait. The trajectories of these buoys during the campaign are shown in Figure 4.1.

Despite the large distance between the five buoys (the northernmost buoy is about 450 km apart from the ARTIST buoy), the drift of all buoys is strongly correlated. This correlation is also present in the temperature and pressure time series, shown in Figure 4.2. It shows a minimum temperature of  $-45^{\circ}\text{C}$  on 10 March. This

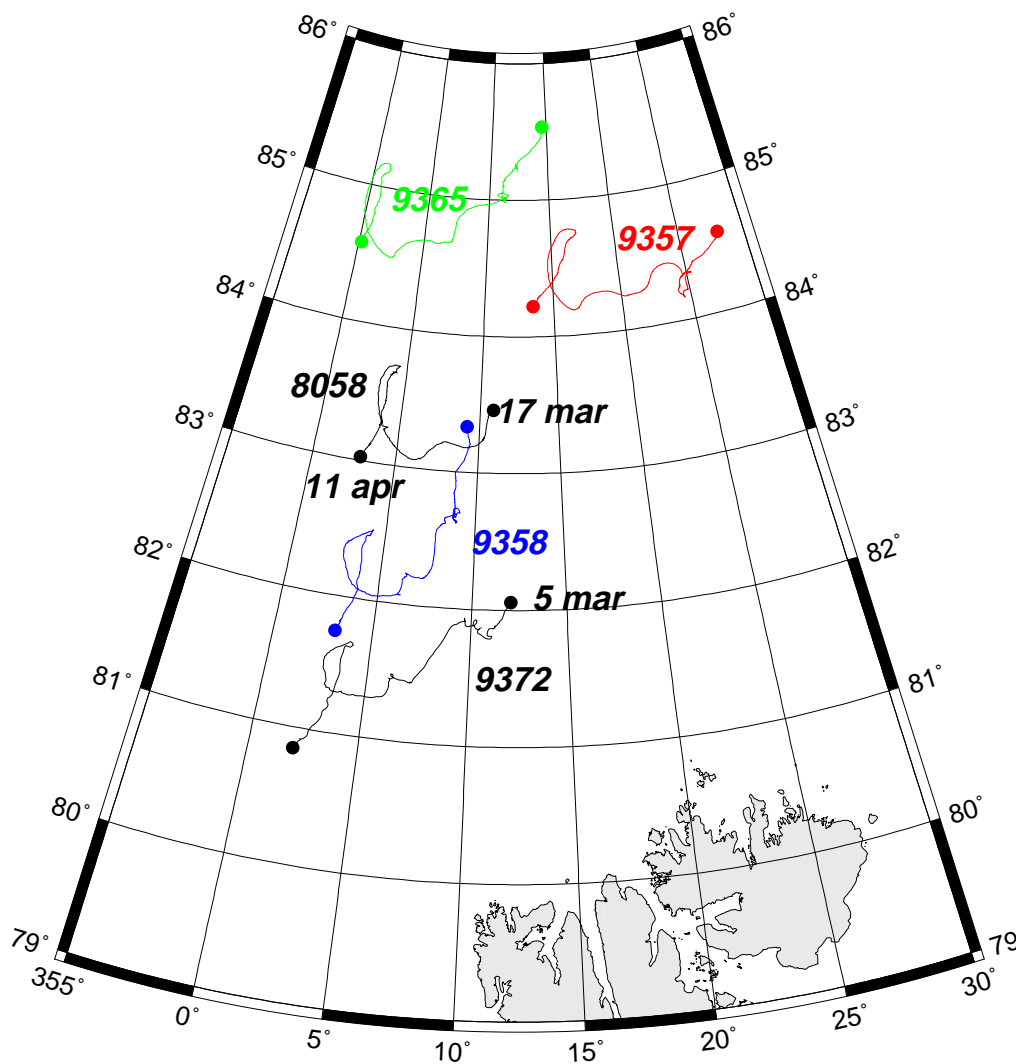


**Figure 4.1:** Trajectories of buoys drifting from north east to south west during ARTIST. The tracks are plotted from 1 March to 11 April, except for Buoy 9372, deployed by Polar 4 on 5 March, and buoy 8058 which lost data before 17 March.

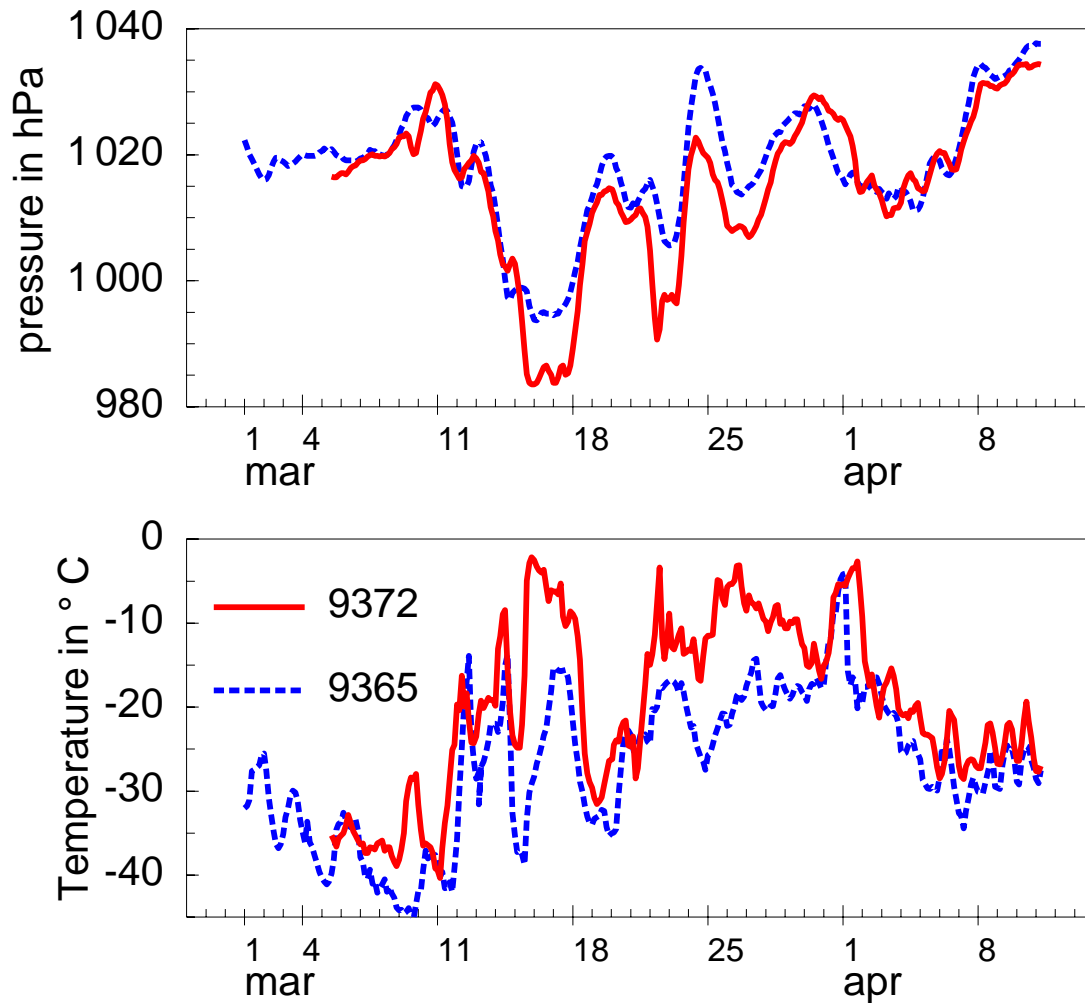


**Figure 4.2:** Time series of pressure and temperature observed by the ARTIST (9372) buoy and the northernmost buoy (9365).

extremely cold period at the beginning of ARTIST was followed by more moderate temperatures.

Figure 4.3 shows the trajectory of the ARTIST buoy in more detail. It is obvious that 4 periods with strong off-ice flow existed whereas a more or less zonal flow regime prevailed between 10 and 17 March, between 21 and 23 March and between 24 and 28 March. There was one period (between 28 March and 2 April) with strong on-ice flow. Figure 4.4. shows the warming due to this on-ice flow at the southernmost buoy for two days and at the northernmost buoy for one day (31 March). One can clearly see that the cold air outbreak which started at the ARTIST buoy at 2 April is present at the northernmost buoy about 24 hours earlier. This cold-air outbreak forced the ice to drift southward until the last day of the experiment.

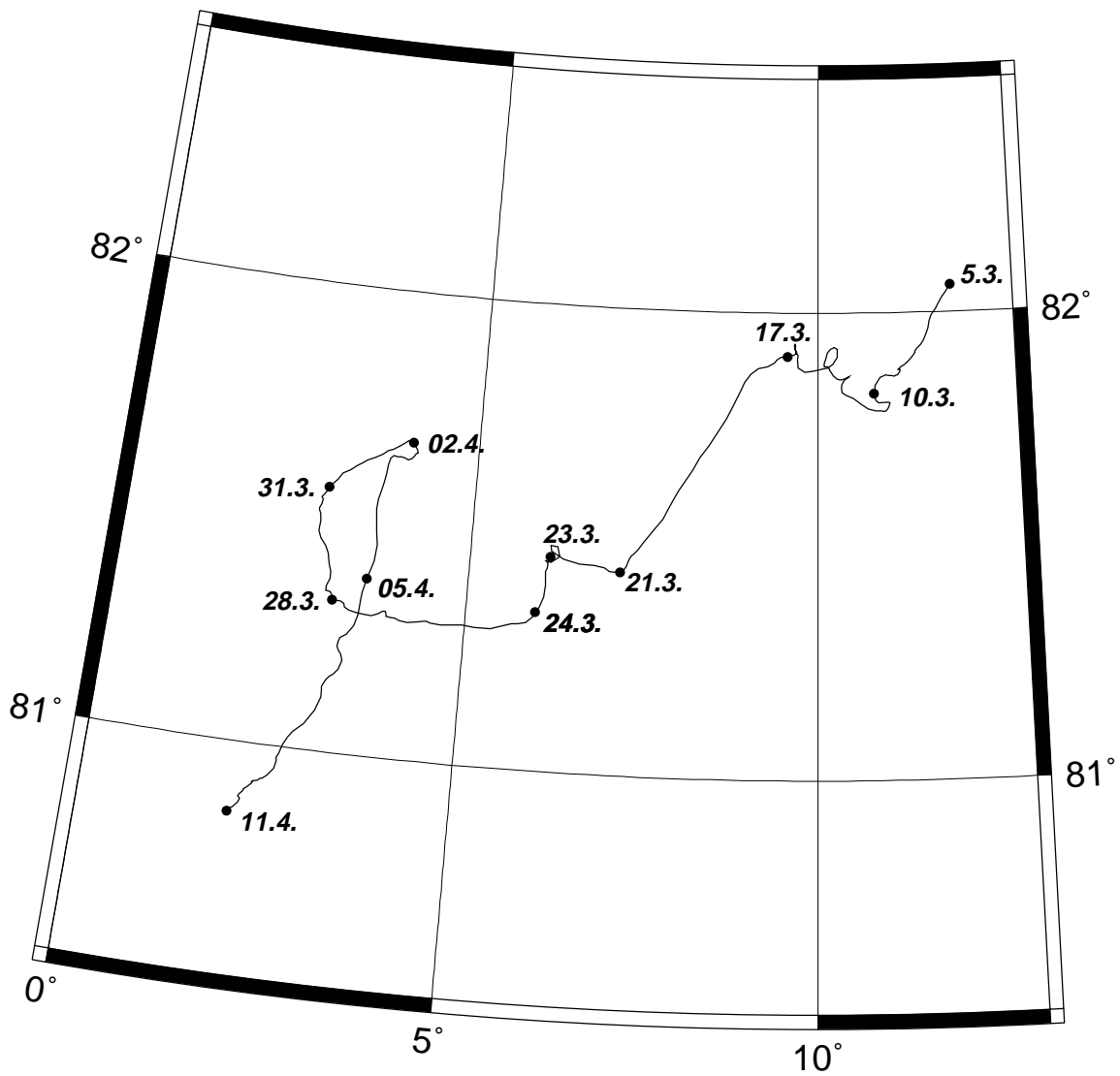
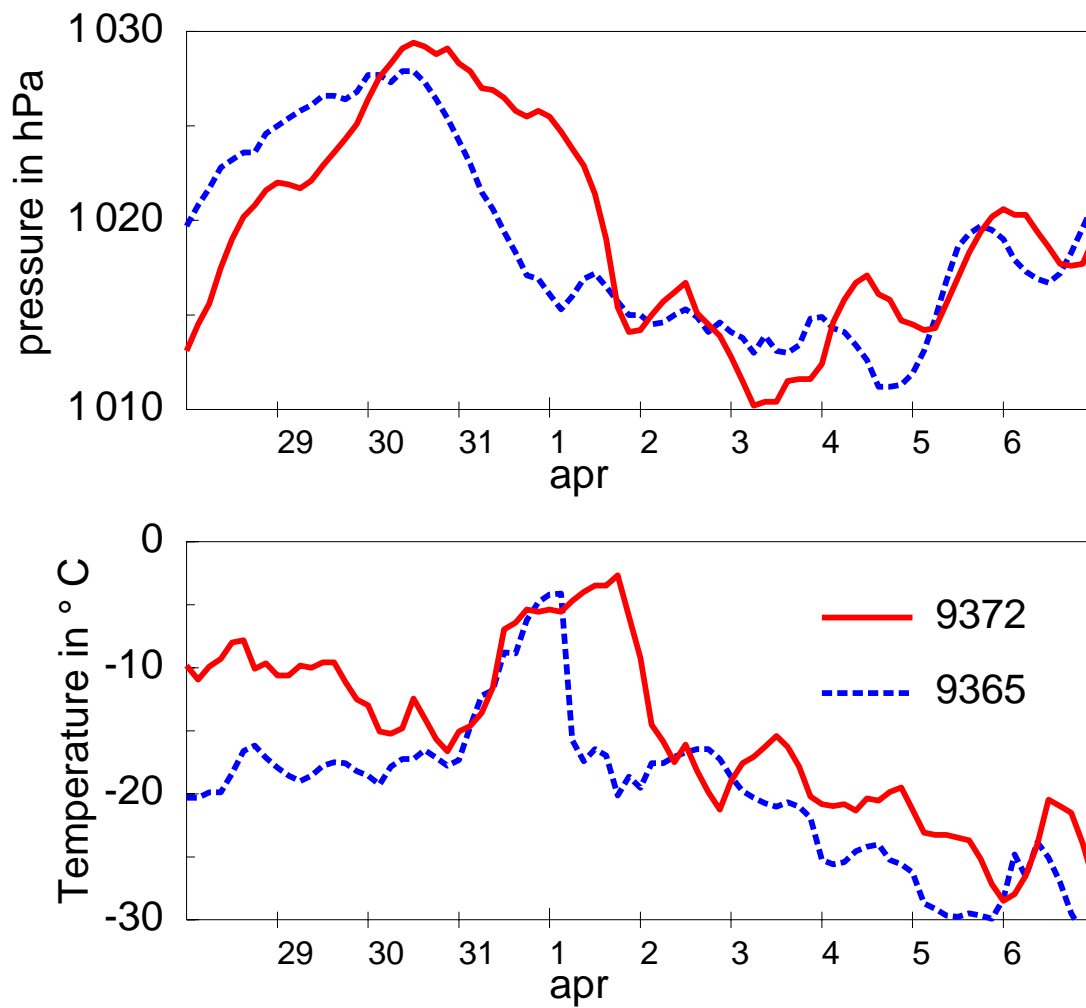


Figure 4.3: Trajectory of the ARTIST buoy 9372.



**Figure 4.4:** Time series of pressure and temperature observed by the ARTIST buoy and the northernmost buoy.

## 4.2. Validation of radiation measurements

### 4.2.1. Alignment error and aircraft movement correction

After calibration and inertia correction, the airborne hemispheric radiation measurements need to be corrected for aircraft movement and tilting with respect to the inertial platform. In order to find these tilting angles, a square box pattern had been flown on 16 March at 6000 m altitude in clear sky condition. The box was aligned with one side parallel to the direction of the sun, its size was 25 km by 25 km, and it was encircled within 20 min. The measurements of the upward looking pyranometer on these 4 legs are shown in Figure 4.5. The left graph shows the pyranometer signal versus  $\cos\beta/\cos\theta$ ,  $\beta$  is the angle between the instruments zenith and the sun and  $\theta$  is the sun zenith angle. At  $\cos\beta/\cos\theta=1$  the radiometer signal equals  $E_{\text{dir}} + E_{\text{diff}}$ . For different angles (due to small scale aircraft movements) it depends linearly on  $\cos\beta/\cos\theta$  and equals the diffuse radiation at  $\cos\beta/\cos\theta=0$ . Further details on the radiation measurement by aircraft can be found in Freese (1999). On the leg with the aircraft heading away from the sun the instrument was briefly shaded by the ruder. Notice that the minimum of this leg coincides with the value of the diffuse radiation calculated by exploiting

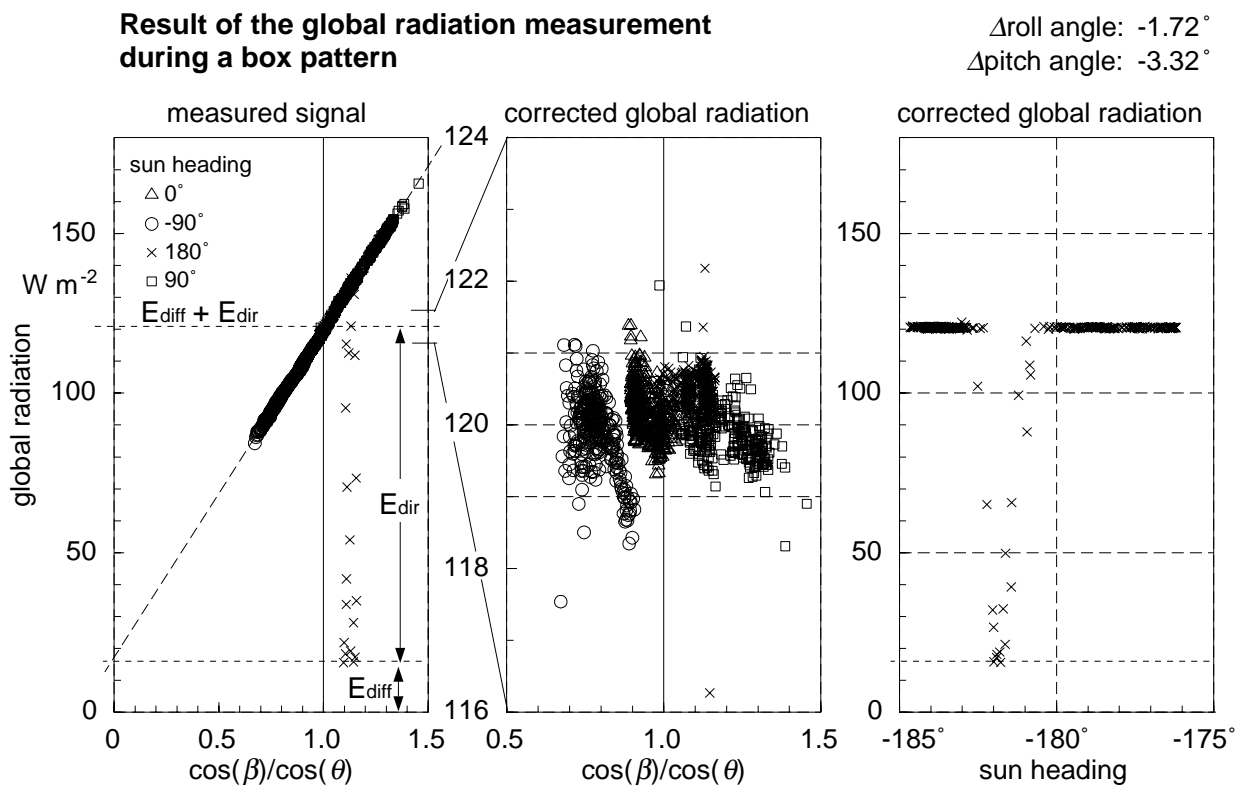


**Figure 4.5:** Global radiation measurements obtained by the upward looking pyranometer on Polar 4 on 16 March at 6000 m altitude. Different symbols indicate the heading of the aircraft with respect to the sun. The direct and the diffuse radiation are indicated by  $E_{\text{dir}}$  and  $E_{\text{diff}}$ , respectively. The left graph shows the measured signal (corrected for tilting versus the inertial system only), the centre and right graphs shows the signal corrected also for aircraft movement.

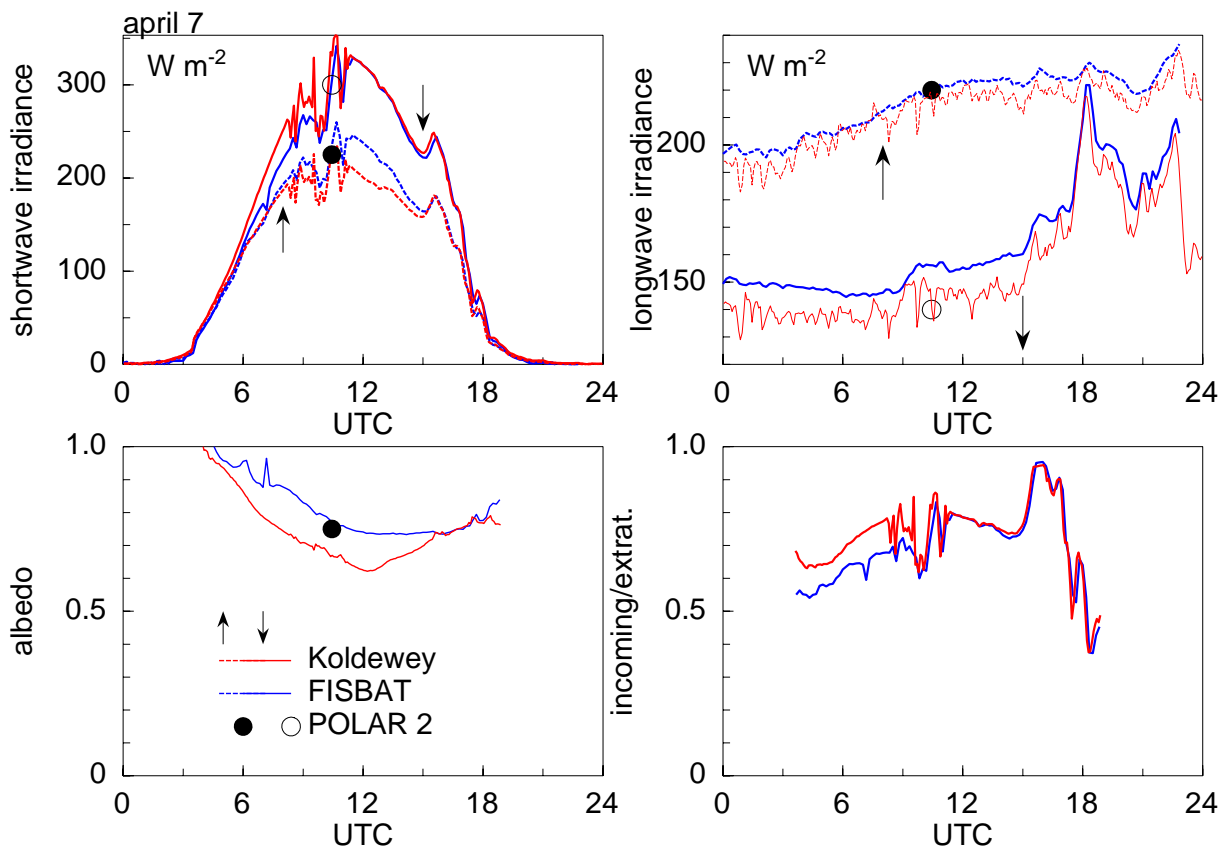


**Figure 4.6:** Radiation measurements at Ny-Ålesund from the FISBAT and Koldewey stations and from a pass by Polar 2 on 7 April. **upper left:** incoming (↓) and outgoing (↑) short wave radiation. **upper right:** incoming (↓) and outgoing (↑) long wave radiation. **lower right:** incoming short wave radiation normalised by the extraterrestrial value. **lower left:** short wave albedo.

the small scale aircraft movements.

The offset angles can be found by minimising the difference of the averages over each of the four legs of the box. The result is  $\Delta\phi = -1.72^\circ$  and  $\Delta\theta = -3.32^\circ$ .

#### 4.2.2. Comparison of airborne and ground based measurements

On 7 April Polar2 flew a pass close to the ground station at Ny-Ålesund. The day started cloud free, but at 17:00UTC a cloud layer moved in. In addition to the measurements of FISBAT, data of the Koldewey station at Ny-Ålesund are also available. Radiation measurements from the three sources are shown in Figure 4.6. The short wave irradiance measurements agree satisfactorily. In the morning, the FISBAT data are slightly smaller than those of Koldewey, which may be due to shading by obstacles. In the afternoon, the reflected short wave radiation of Koldewey is smaller. Differences in the incoming long wave data and to a smaller extent also in the outgoing long wave data seem to be due to systematic calibration effects, which still need to be investigated.

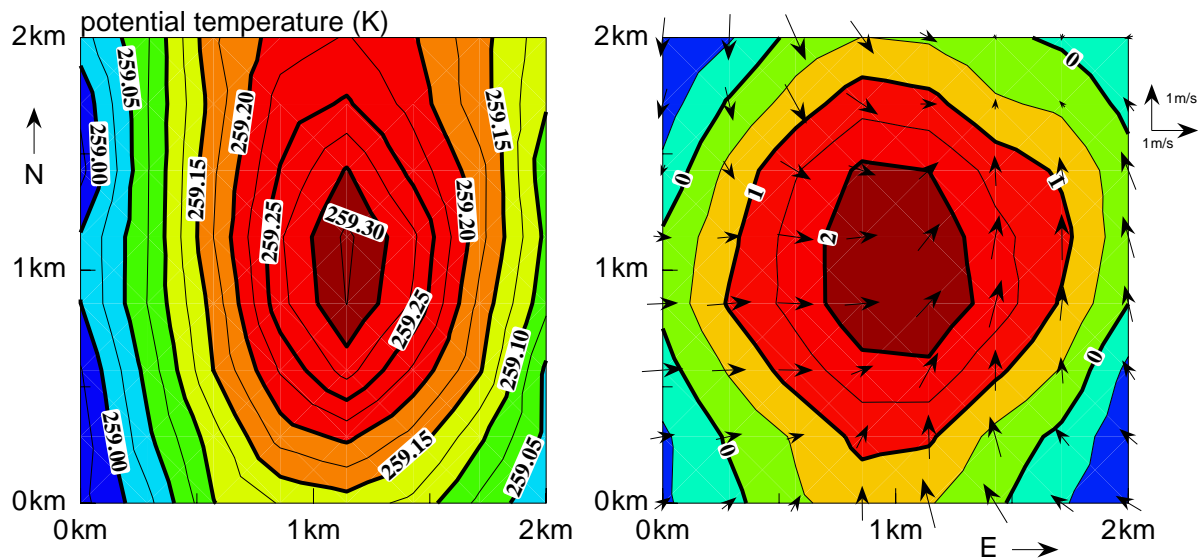


**Figure 4.7:** Potential temperature (left graph), deviation from the mean horizontal wind (right graph, arrows, scale on right margin in m/s) and vertical wind velocity (right graph, contours in m/s) in an average convective cell on 8 April. The abscissa represents the east-west direction, the ordinate north-south. The mean wind vector was oriented north-south.

### 4.3. Convective cell structure, 8 April 1998

On April 8 in strong organised convection over the ocean off Svalbard, both aircraft circled a square pattern of 20 by 20 nm size at two heights (400 m and 500 m) and in two angular orientations. The first flight level was located in the lower third of the cloud, the second level in the upper third. The cloud coverage was 6/8 cumuli.

Convective cells were identified by a conditioning sampling technique. A low pass filter with a cut-off at 1.3 km was applied to the vertical wind velocity. Sections of 2 km length centred around maximum values exceeding 1 m/s were selected as indicator for convective cells. These sections were normalised in length and the data were averaged over all sections thus identified. From the legs flown in eight different orientations a 2-dimensional composite was assembled by a tomography method. The results are shown in Figures 4.7 and 4.8.

Since the potential temperature is closely correlated with the vertical wind velocity, the cell contributes remarkably to the vertical sensible heat flux. The downward long wave radiation has its largest values also in the centre, where the cloud particle formation is highest. In contrast, the upward long wave radiation is strongest near the cloud margins where the radiation from the warm ocean makes a considerable contribution. The downward short wave radiation is asymmetric, since the cell side directed towards the sun receives the largest amount of solar radiation and creates the largest scatter. The latter is responsible also for the distribution of the upward short wave flux.

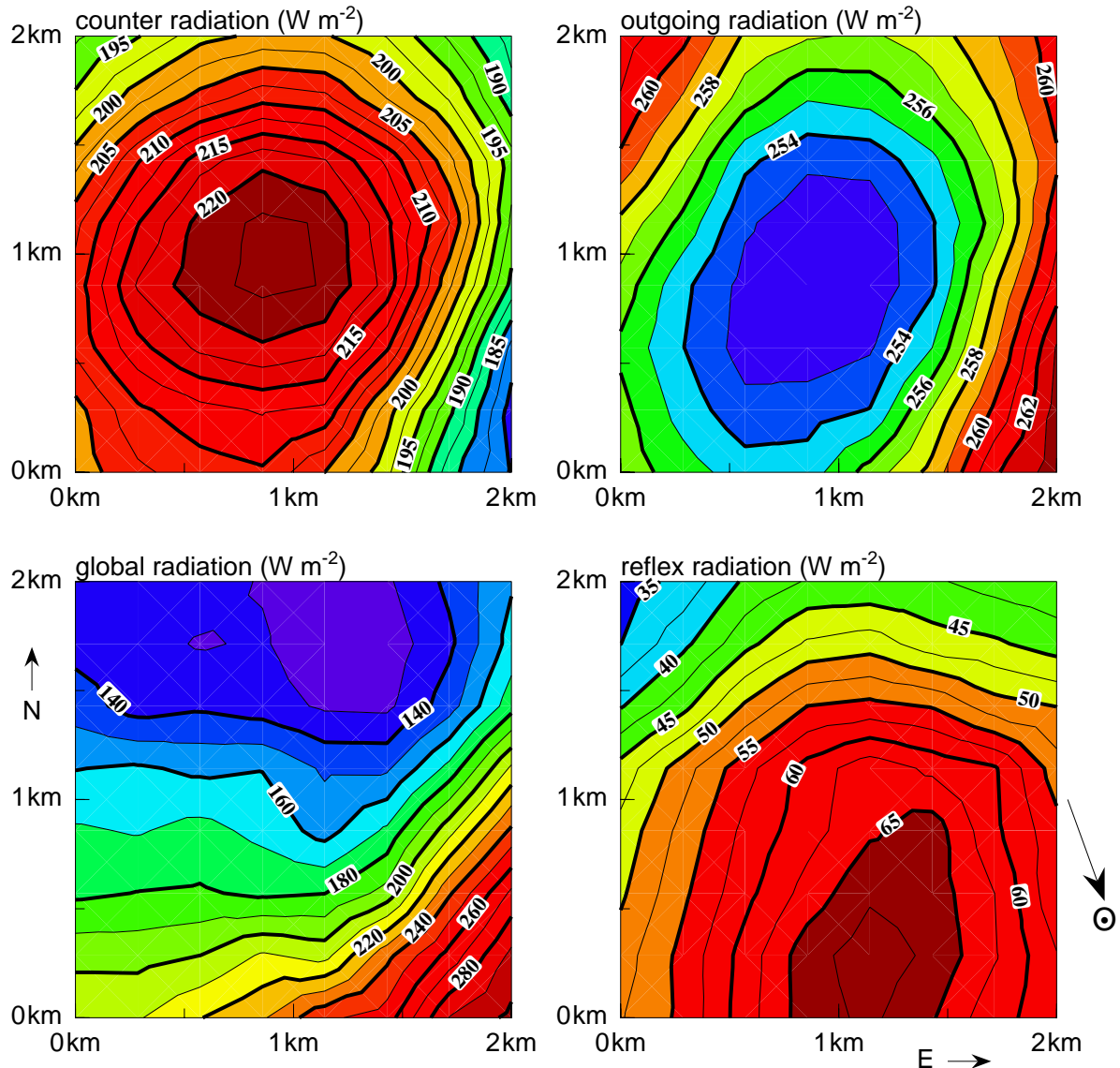


**Figure 4.8:** Radiation in the averaged convective cell. Upper graphs: long wave radiation, lower graphs: short wave radiation, left graphs: downward radiation, right graphs: upward radiation. The abscissa is oriented towards east, the ordinate towards north. The arrow at the lower right margin indicates the direction towards the sun.

#### 4.4. Cold air outbreak, 4 April 1998

Between a low pressure system east of Svalbard and high pressure over Greenland a typical cold air outbreak occurred over Fram Strait on April 4. Charts of the surface pressure, the 500 hpa level and the 850 hpa temperature are shown in Figure 4.9. The maps are plotted from data of the medium range weather forecast model (MRF) of the US National Center for Environmental Prediction (NCEP). A satellite picture and the flight path of this day are shown in the flight catalogue section (page 38).

Due to a strong wind of 15 m/s a 400 m thick dynamically driven mixed layer developed over the ice. It was capped by a sharp temperature inversion. The air temperature near the surface was  $-22^{\circ}\text{C}$ . Over the relatively warm water con-

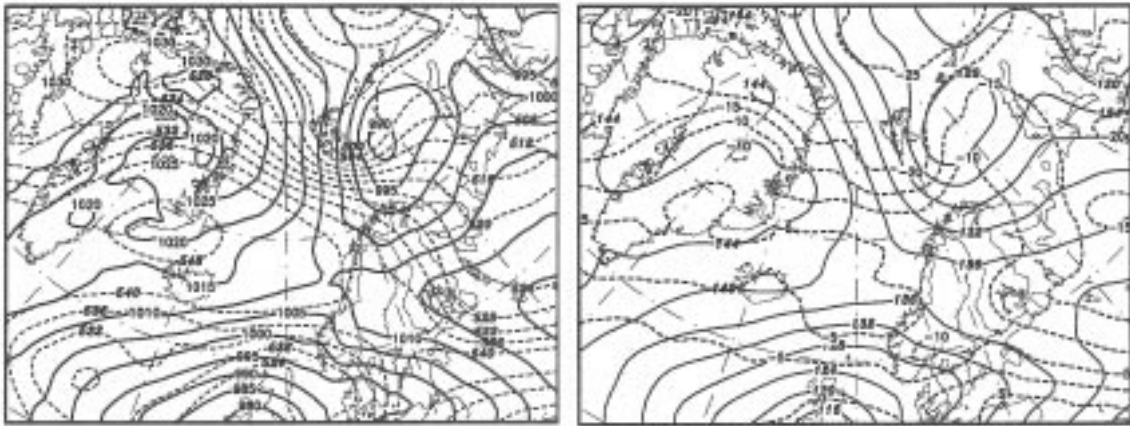


**Figure 4.9:** Surface pressure and 500 hpa level (left) and 850 hpa relative topography and temperature for 4 April 1998, 12 UTC plotted from the 24 h forecast data of the MRF run at NCEP.

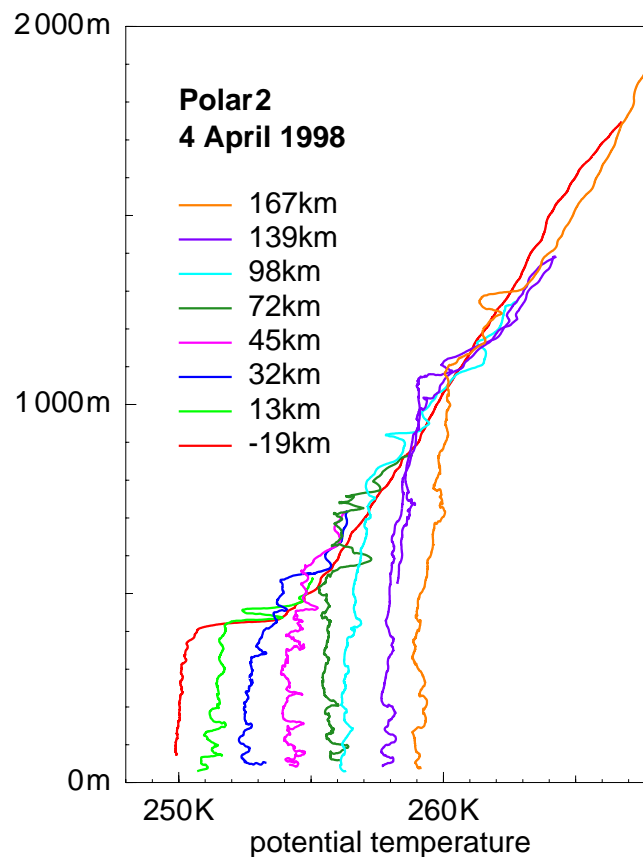


**Figure 4.10:** Vertical profiles of potential temperature measured by Polar 2 during the saw-tooth pattern on the southbound flight on 4 April 1998.

vection enhanced the vertical mixing and the surface evaporation enabled the formation of cloud streets. Profiles of the potential temperature show the heating and growth of the mixed layer (Figure 4.10).

At  $80^{\circ}35'30''N$  the southern limit of the nearly closed pack ice can be clearly seen in the surface temperature record (Figure 4.11). Fields of ice floes occur up to 20 km south of the edge of compact ice.

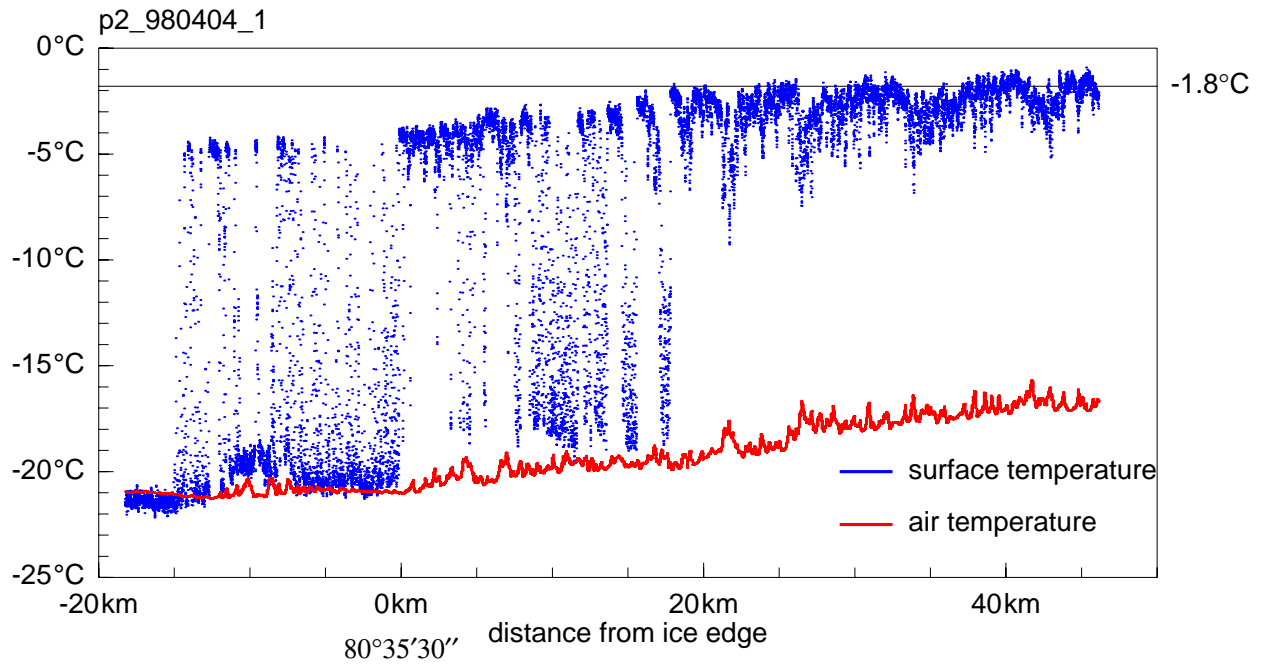


**Figure 4.11:** Surface temperature, measured by the KT4 radiation thermometer and near-surface air temperature, measured by a Pt100 thermometer. The freezing temperature of sea water ( $-1.8^{\circ}\text{C}$ ) is marked by a horizontal line.

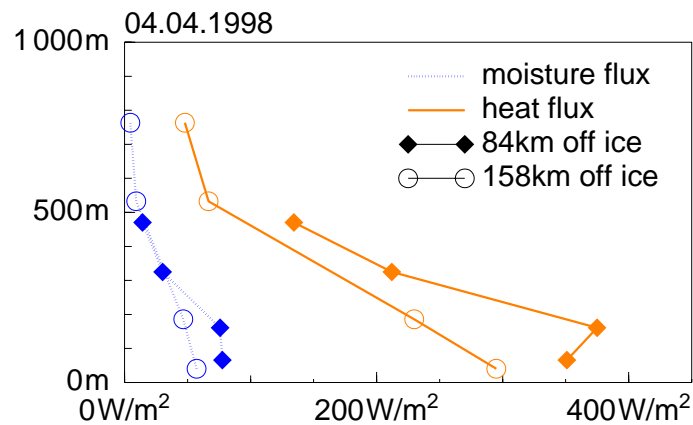


**Figure 4.12:** Vertical profiles of sensible and latent heat flux over water at two different distances from the ice edge.

The sensible heat flux dominated the convective mixing. At 84 km south of the ice edge it exceeded the latent heat flux by six times, at 158 km by four times. Profiles of these fluxes are shown in Figure 4.12.

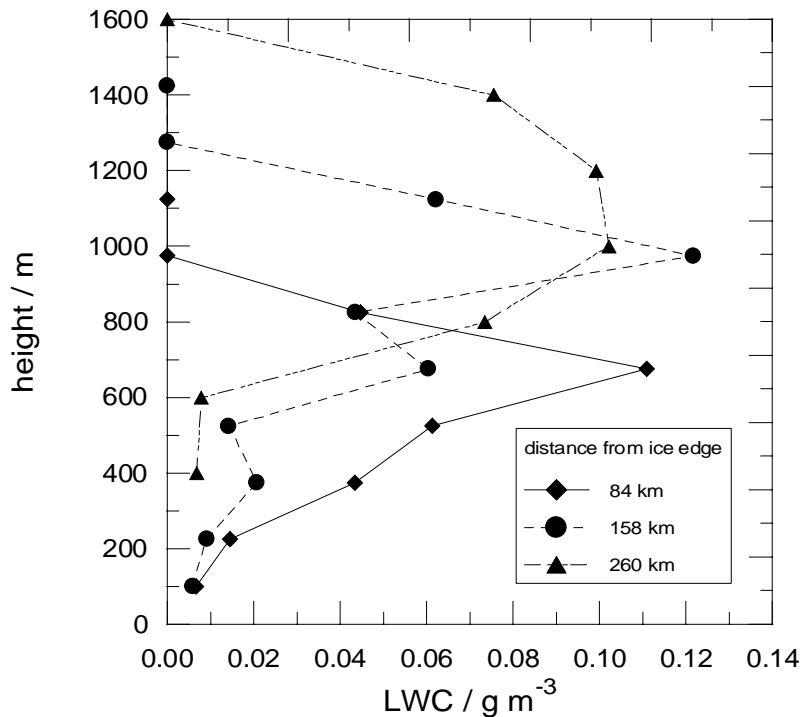


Figure 4.13: LWC profiles for case  $p$ .

#### 4.5. Cloud particles, 4 April 1998

During the cold air outbreak on 4 April, cloud particles were measured by the FSSP-100 (sizerange 2–47  $\mu\text{m}$ ) and the 2D-Greyprobe. Particle habit detection algorithms had been applied to the 2D-Greyprobe data to separate water droplets from ice crystals. Calculated microphysical values from all flight legs and all vertical soundings at constant distance from the ice edge were sorted into equally spaced height bins and averaged.

Figure 4.13 shows vertical profiles of the liquid water content (LWC) at 3 distances from the ice edge. Because of the sampling strategy, the presented values are layer averages, containing cloudy and cloud-free segments. Local LWC values inside the clouds have been higher than the averages. The LWC generally increases with height in the lower two thirds of the clouds and then decreased towards the cloud top due to entrainment of drier air. Precipitation leads to non-zero LWC values down to the sea surface. The maximum LWC is almost constant at about  $0.1 \text{ g m}^{-3}$  but the vertically integrated liquid water path (LWP) is increasing downstream from  $41.9 \text{ g m}^{-2}$  (84 km distance) to  $73.1 \text{ g m}^{-2}$  (260 km distance). The depth of the entrainment layer is rather pronounced and affects the upper 30% to 40% of the clouds. A droplet spectrum near cloud top (within the entrainment layer) is shown in Figure 4.14 (left). The peak of the droplet size is very narrow and a second maximum appears at about  $10 \mu\text{m}$ . Similar features in particle size spectra have been reported by Baker and Latham (1979) and Korolev (1995) as a result of cloud top entrainment.

In the lower third of the clouds, the size spectra of the liquid water drops often

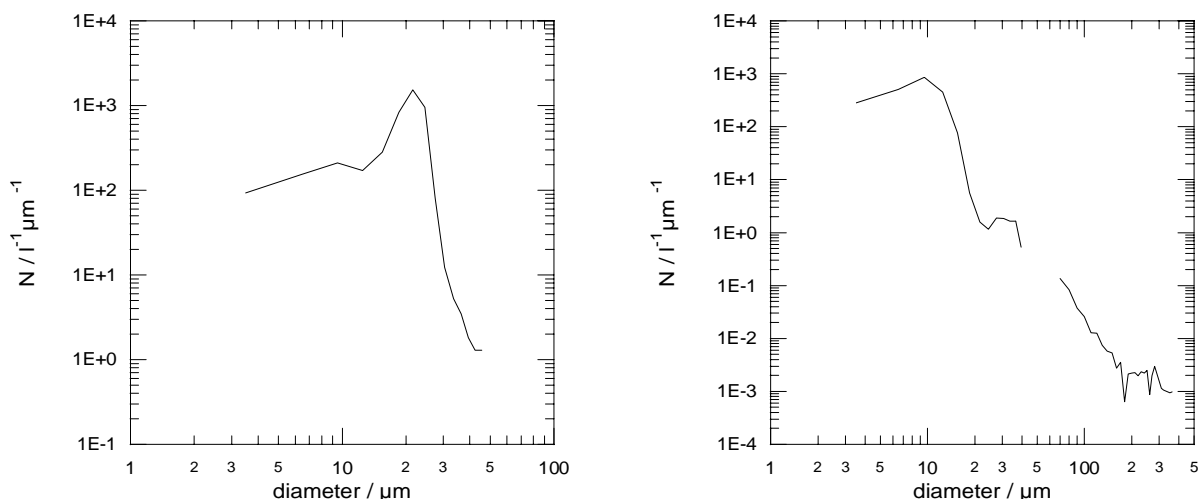


**Figure 4.14:** **left:** Cloud droplet spectrum for April 4 near cloud top (1125 m) at 158 km distance from the ice edge (FSSP-100 data). **right:** Size spectrum of liquid water drops at 260 km distance from the ice edge at 600 m height (near cloud base).

exhibit a trimodal shape (Figure 4.14, right). Beside the main maximum in the cloud droplet part of the spectrum (around 10 μm), there are two additional maxima in the embryonic drizzle drop size range (around 40 μm) and in the drizzle size range (around 300 μm, for definitions of "drizzle" and "embryonic drizzle drops", see e.g. Huschke, 1989). Generally, cloud droplets are smaller near cloud base (Fig. 4.14) and the distribution is much broader. While the terminal velocity for drizzle drops (1.1 m/s for a 300 μm drop) is larger than the updraft motions, the opposite is true for the embryonic drizzle drops (for parameterizations of terminal velocities see e.g. Considine and Curry, 1998). For a 50 μm drop, the terminal velocity is about 0.1 cm/s and therefore smaller than the vertical wind speed. Thus, turbulent transport of embryonic drizzle drops very likely plays an important role in the development of the related peak in the size distribution and should gain sufficient attention for future work.

In the cold air outbreak, mixed-phase clouds developed where ice particles co-existed with water drops as shown in Figure 4.15. The ice water content IWC generally decreases with height since glaciation usually takes place in the upper parts of the clouds where temperatures are lowest. While falling through the cloud, ice particles grow by riming, accretion and aggregation. The maximum IWC is in the order of 30 mg m<sup>-3</sup>. In the upper half of the cloud, the ice water fraction is less than 25% of the total water (LWC+IWC) but 75% near cloud base. The precipitation is predominantly snow. Because of the low ambient temperature and the low cloud base height, sublimation is not significant below the cloud. The integrated ice water path (IWP) increases from 18.6 gm<sup>-2</sup> (84 km distance from the ice edge) to 25.9 gm<sup>-2</sup> (260 km distance from the ice edge) due to increasing cloud thickness.

In mixed-phase clouds, growth of ice particles is favoured over growth of water particles as illustrated by the 2D-Greyprobe data for the lower part of the clouds at 84 km distance from the ice edge in Figure 4.16. As mentioned above, updraft

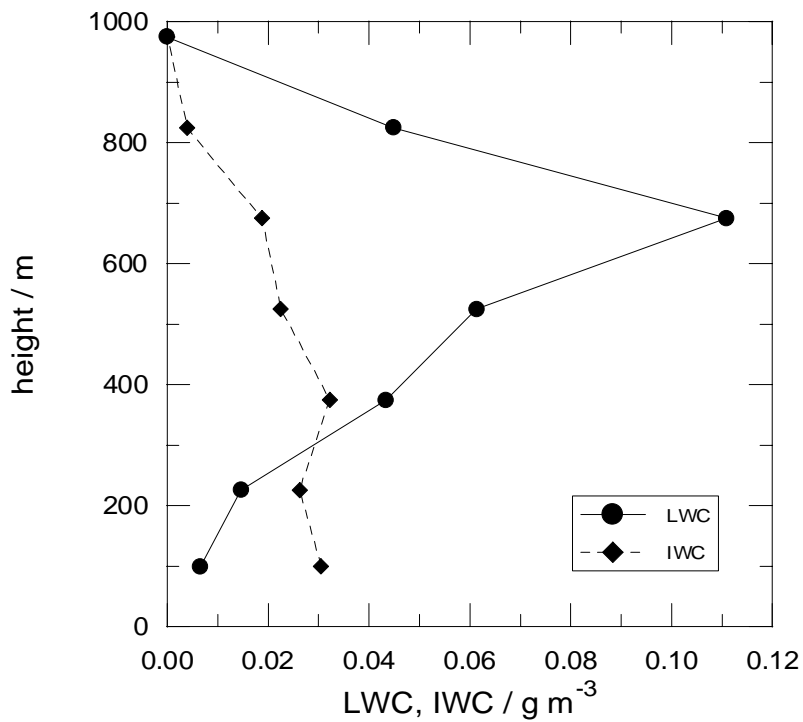


Figure 4.15: LWC/IWC profile for 4 April at 84 km distance from the ice edge.

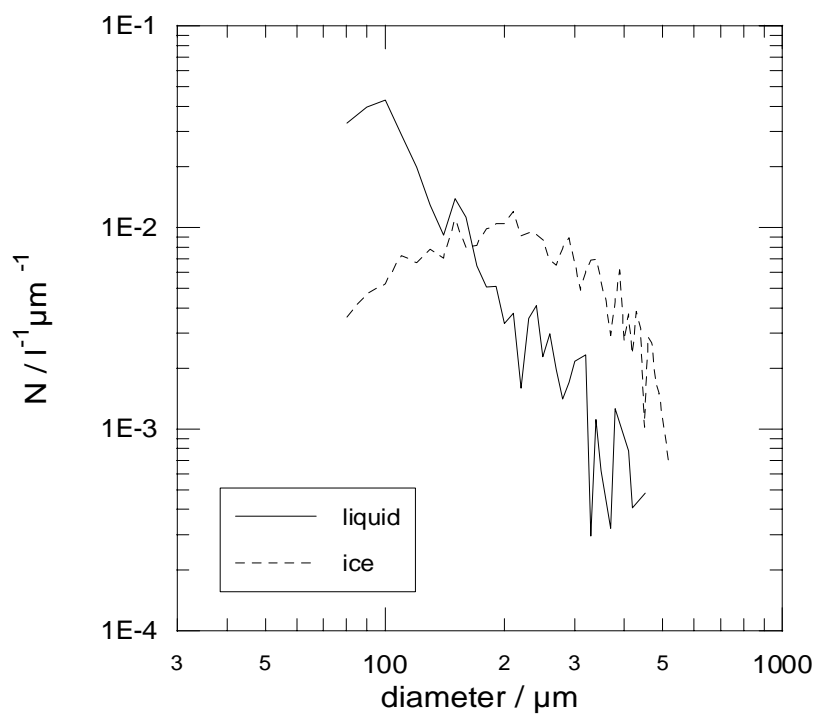
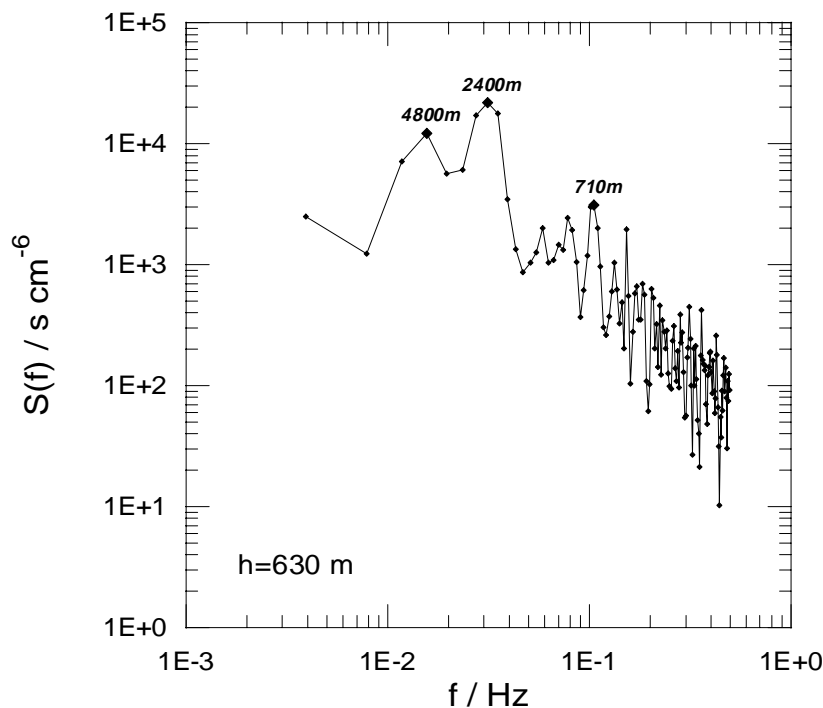


Figure 4.16: Combined liquid / ice particle spectra for case *p* (4 April) at 84 km distance from the ice edge on the basis of 2D-Greyprobe data. The height is 375 m.



**Figure 4.17:** Variance spectrum of particle concentration for 84 km distance from the ice edge.

motions are larger than terminal velocities for smaller particles. Therefore, particles smaller than about 100 to 200  $\mu\text{m}$  are either produced locally or are advected by updrafts, while larger particles stem from above. For the smaller particles, the number density of liquid drops is much higher than for ice particles, since glaciation processes are not very pronounced in the lower part of the cloud. Ice particle number densities of larger particles are about 5 times higher than those of liquid drops. This can be explained by the different growth mechanisms. Ice particles are growing preferential to water drops from the water vapour phase since the saturation vapour pressure over ice is lower than over water. Diffusional growth of water drops is therefore restricted in the presence of ice particles. Interactions of supercooled drops with ice crystals result in riming and ice build-up. Only collision between supercooled drops acts as a second growth process for liquid drops in mixed-phase clouds. Ice particles can grow from the water vapor phase, by aggregation, accretion and riming. This leads to the high number densities of larger ice particles in Figure 4.16 because liquid drops can be easily removed while falling through the cloud.

Three flight stacks have been aligned perpendicular to the cloud streets allowing the determination of characteristic wavelengths and aspect ratios of the PBL circulation. For this purpose, FSSP-100 1 Hz data were used to determine roll wavelengths. The variance spectrum of the FSSP-100 particle concentration values is shown in (Figure 4.17).

By comparing data of the three stacks, we can generally distinguish three main frequency peaks. The related wavelengths are displayed in Figure 4.18. The

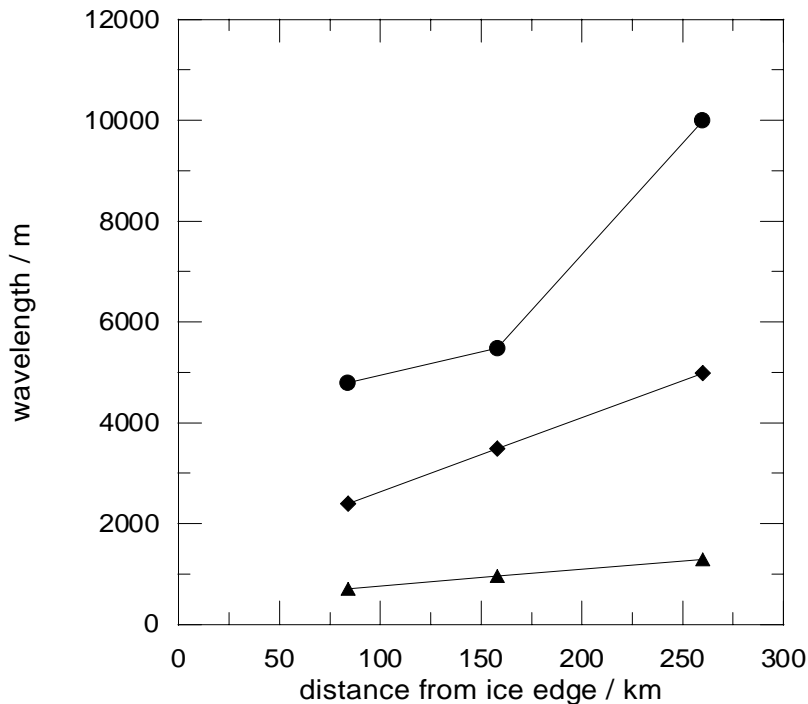


**Figure 4.18:** The three main wavelengths of the multiscale rolls on April 4. "a" denotes the aspect ratio of the cloud streets.

occurrence of multiple wavelengths has already been reported from earlier measurements, especially in Arctic cold air outbreaks (Brümmer et al., 1982; Hein and Brown, 1988; Martin and Bakan, 1991). The main wavelength related to the cloud streets (squares in Figure 4.18) increases from 2.4 km at 84 km off the ice edge to up to 5.0 km at 260 km.

Variations of microphysical parameters across the cloud streets have been determined by a conditional sampling method. Composites based on traverses of several cloud streets along one horizontal flight leg are shown in Figure 4.19 at 84 km distance from the ice edge and at 630 m height. The liquid water content, the average particle diameter and the particle concentration are all largest in the centre of the cloud streets.

#### 4.6. On-ice flow, 27 March 1998

The boundary layer structure during an on-ice flow situation was observed on 27 March 1998. In an easterly airstream of 5 to 10 m/s, a shallow near neutral boundary layer formed over the ice between Kong Karls Land and Nordaustlandet. Polar 2 flew several east and west bound traverses of 100 km length parallel to the wind direction in the boundary layer at 30 to 60 m above the ice. At the eastern and western turning points, vertical soundings were made up to 1000 m height.

The wind speed and direction in the boundary layer along the flight path are shown in Figure 4.20. The wind direction turned from south-east at the eastern end to

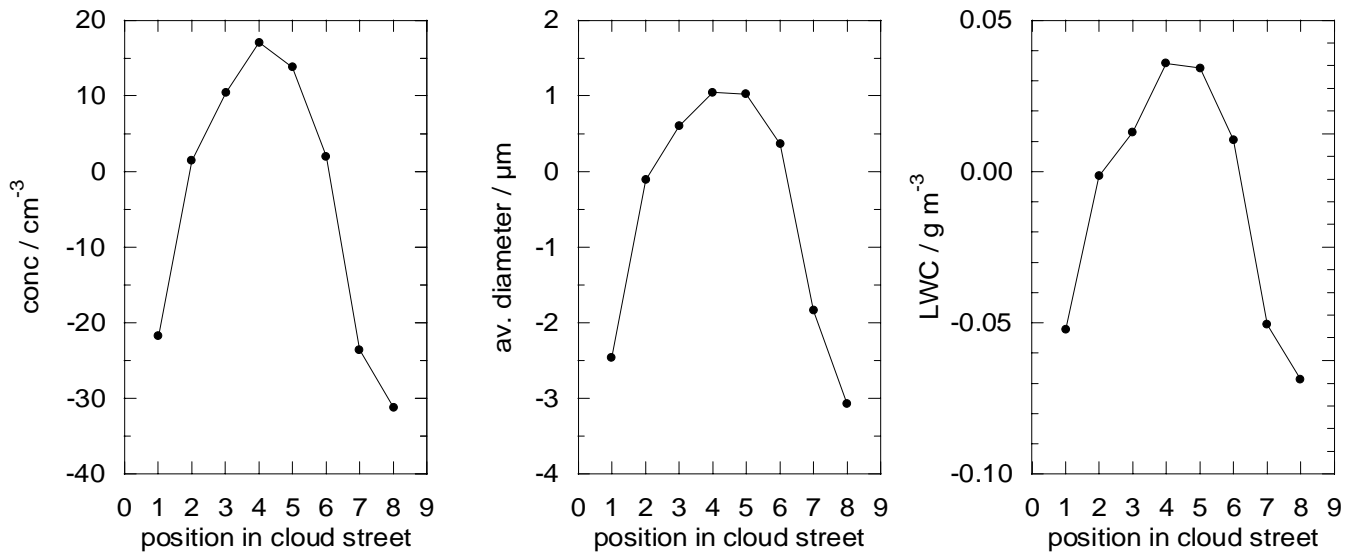


**Figure 4.19:** Variations of particle concentration, average diameter and LWC across an average cloud street in 84 km distance from the ice edge (630 m height). Shown are the deviations from the leg average values. Regarding the position in the cloud street, "1" denotes the western margin of the cloud, "8" the eastern margin.

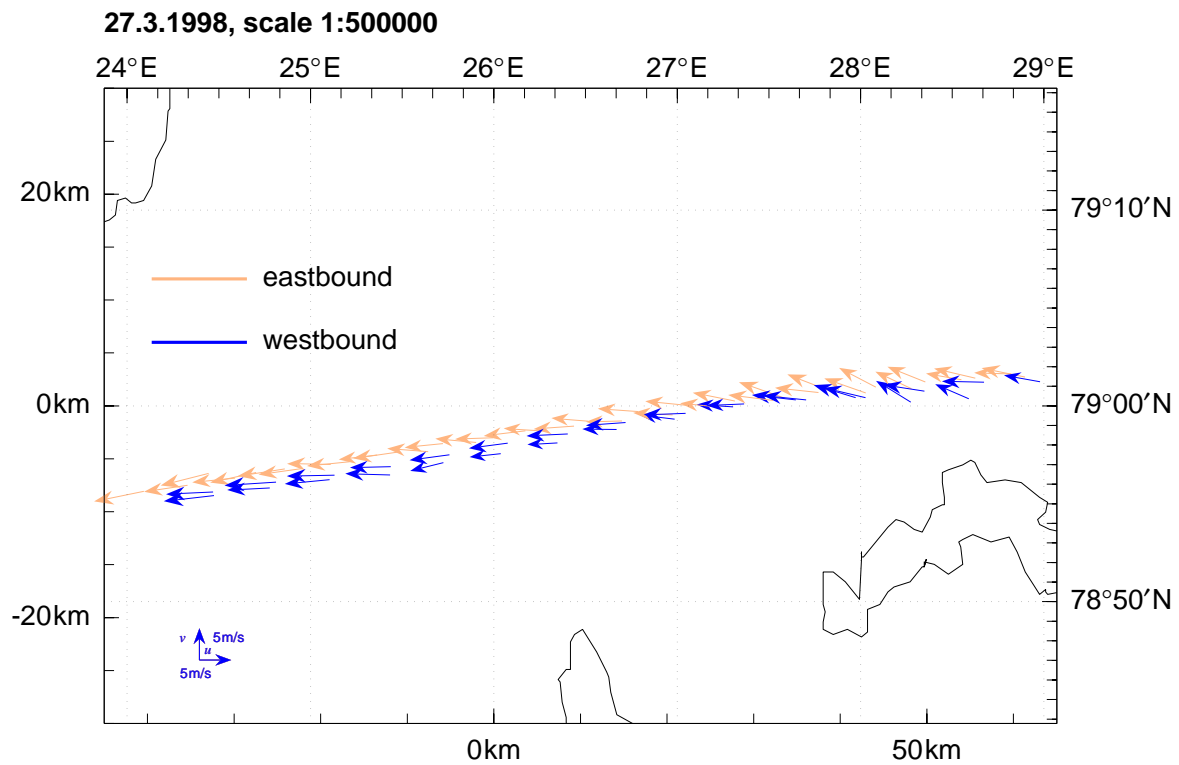


**Figure 4.20:** Horizontal wind vectors along the flight path at 27 March 1998.

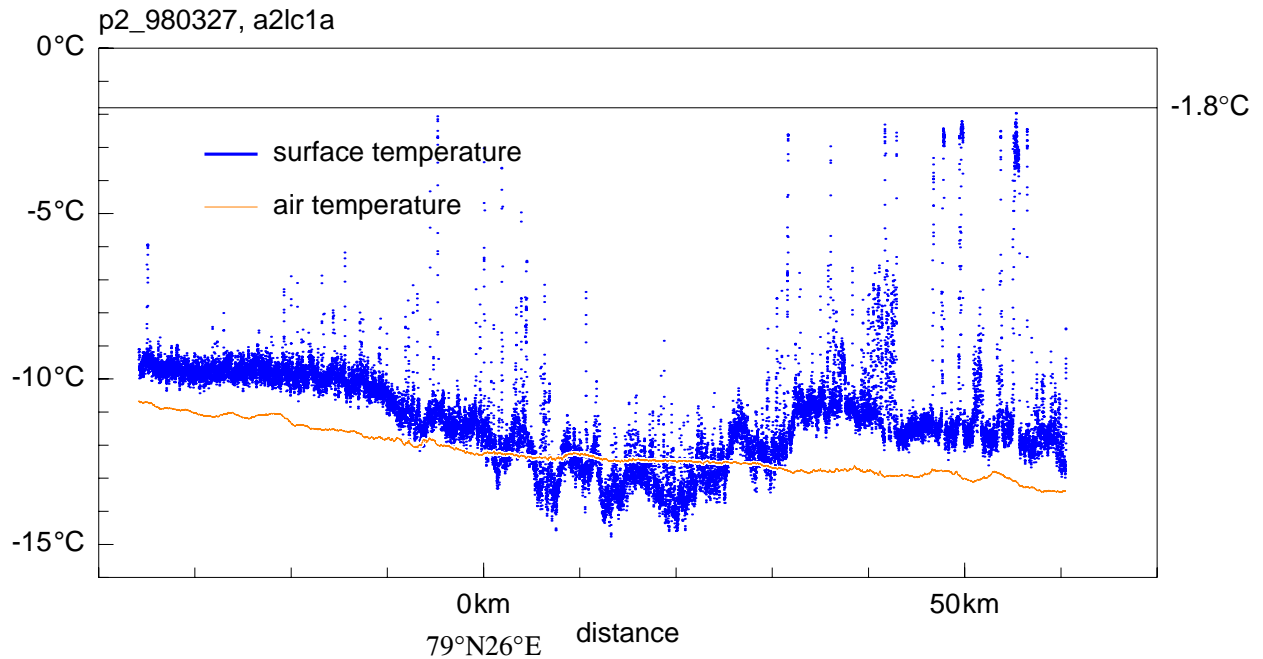


**Figure 4.21:** Surface temperature, measured by the KT4 radiation thermometer and near-surface air temperature, measured by a Pt100 thermometer.

an east-north-east at the western end. At both ends of the flight section the boundary layer was mixed by weak convection with the low level air temperature 1 to 2 degrees above the surface temperature. In the middle part the surface temperature was about 1 degree below the air temperature (Figure 4.21). This temperature distribution led to small positive heat fluxes at both ends and a small negative heat flux in the middle part of the flight path (Figure 4.22). The mixed layer increased from about 400 m thickness at the eastern end to 600 m at the western end (Figure 4.23). According to radiation measurements, cloud top cooling is a likely forcing mechanism for the downstream increase of the boundary layer.

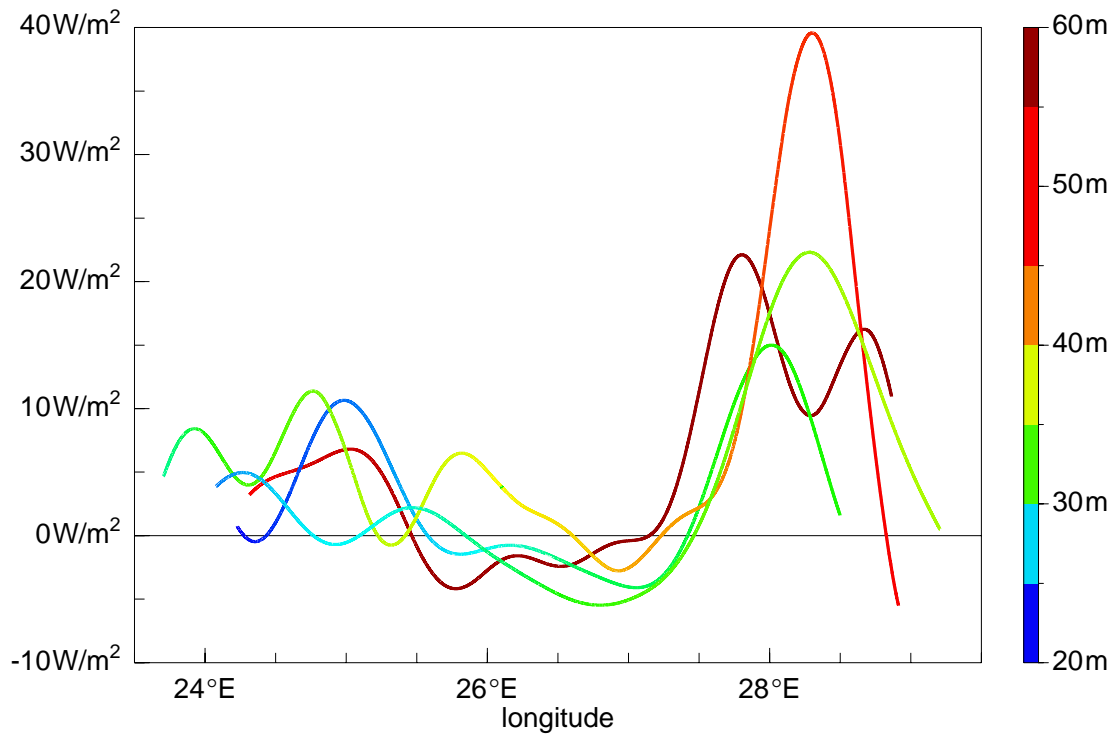


**Figure 4.22:** Turbulent heat flux along the flight path for 4 consecutive traverses. The turbulent flux is calculated for scales up to 3 km and low-pass filtered with a cut-off at 20 km. The height of the aircraft varied between 25 and 60 m above ground and is coded in the graph as a colour scale.

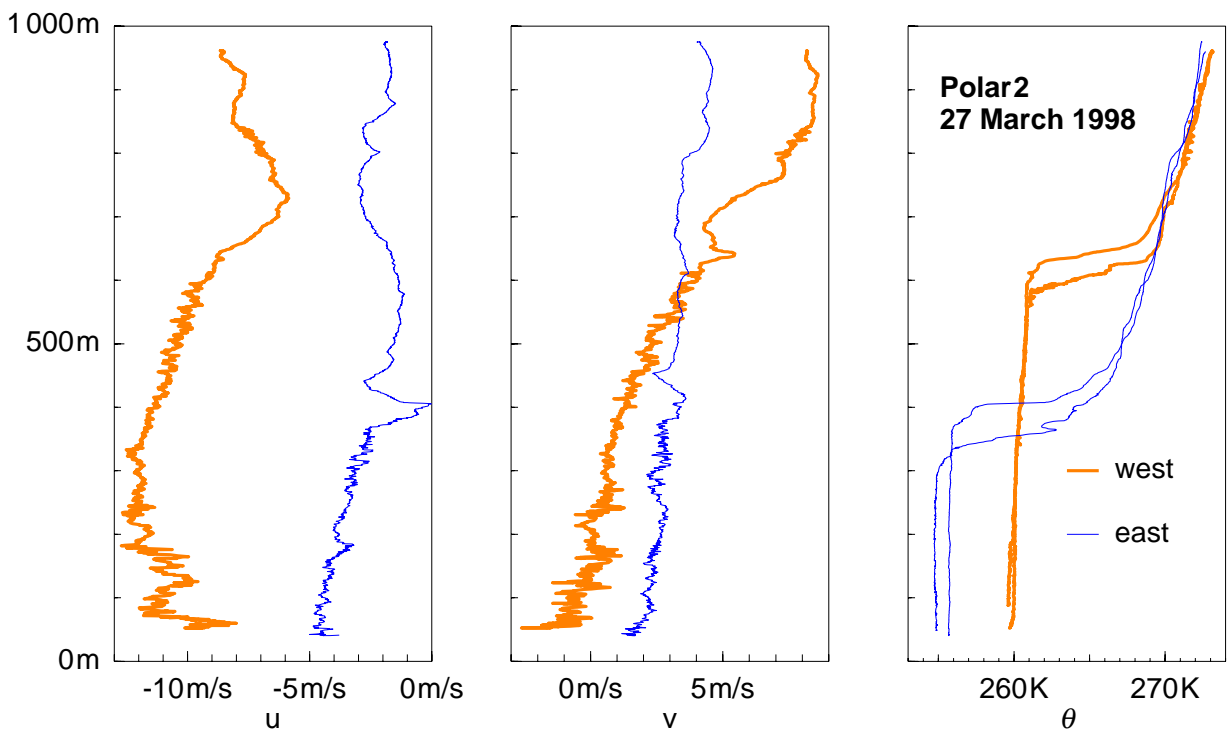


**Figure 4.23:** Vertical profiles of the horizontal wind components and the potential temperature at the western and eastern ends of the flight section.

#### 4.7. Microwave remote sensing of sea ice, 30 March 1998

Coordinated satellite (DMSP and ERS-2) underflights were carried out with Polar 4 over the sea ice regions near Svalbard. The new radiometers are sensitive at frequencies of 19.35 GHz and 37.0 GHz. Water and ice can be distinguished, since the difference between the vertically and horizontally polarised radiances is small for ice compared to open water.

Figure 4.24 shows two ERS-2 SAR scenes of the sea ice region during the aircraft underflight on March 30th 1998 and five photographs taken during this flight. The SAR images show a sharp ice edge at 81.65°N, 55°E.

Figure 4.25 shows a time series of the polarisation ratio  $P$  and gradient ratio  $G$  defined as

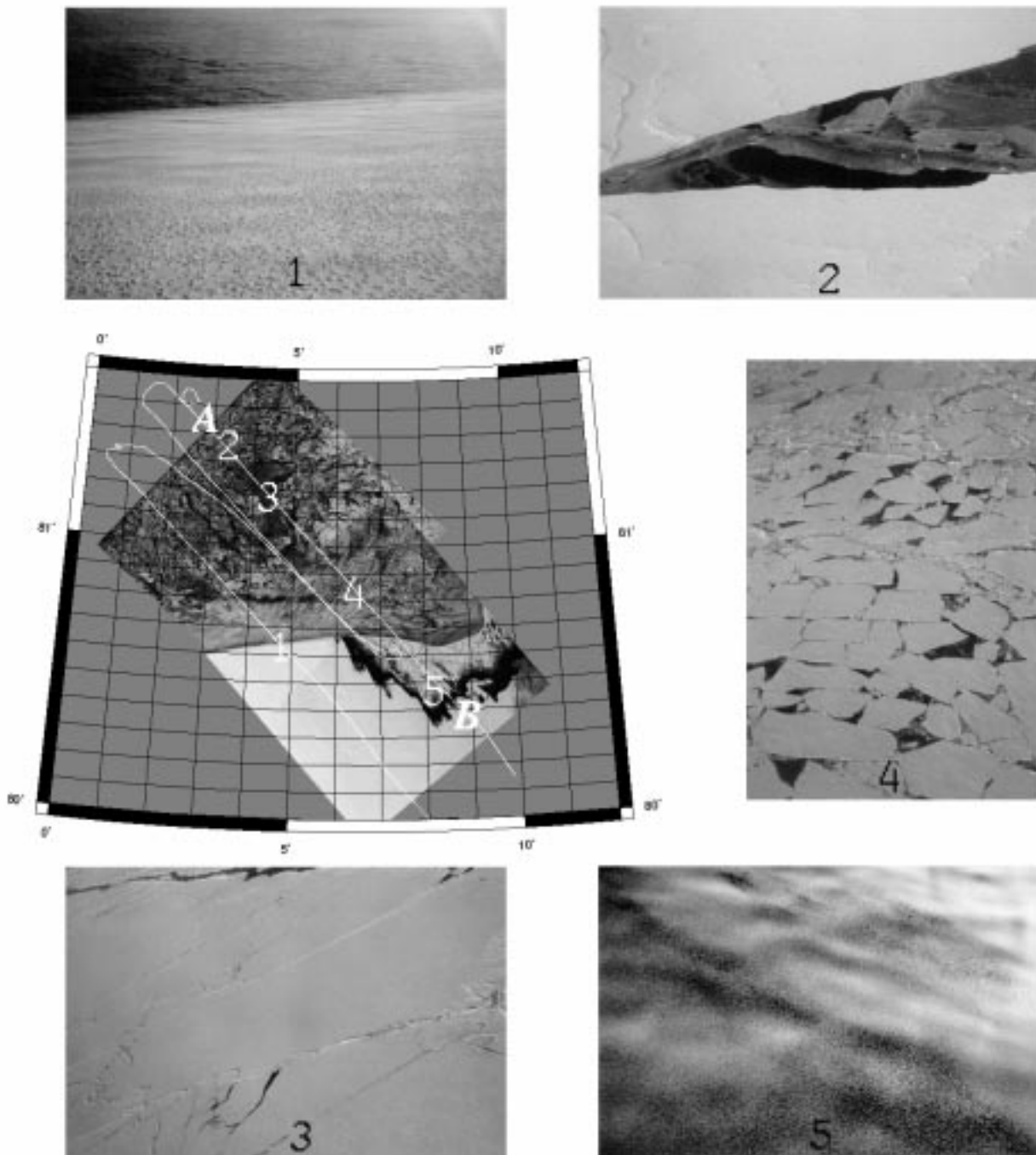
$$P = \frac{T(19V) - T(19H)}{T(19V) + T(19H)}$$

$$G = \frac{T(37V) - T(19V)}{T(37V) + T(19V)}$$

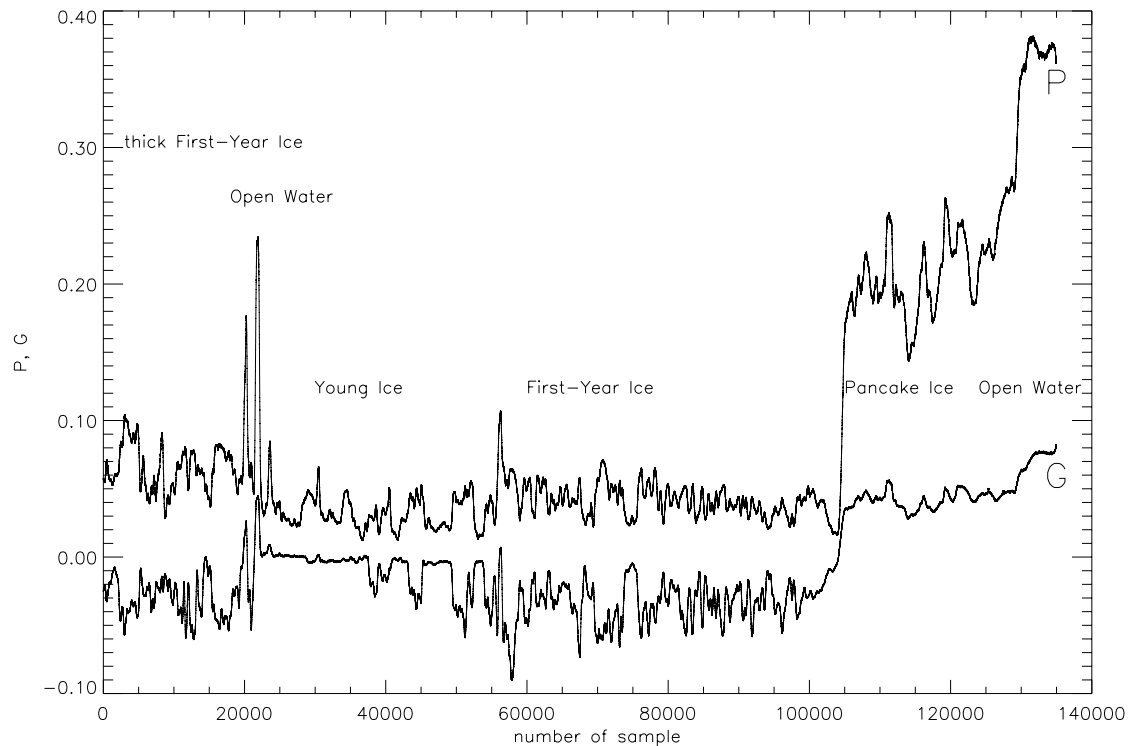
$T(f)$  denotes the measured brightness temperature at the frequency  $f$  and  $V$  and  $H$  indicate the vertical and horizontal polarization, respectively. The use of ratios of radiances reduces the dependence of the results on surface temperatures. The area was cloudless, therefore the influence of the atmosphere on the microwave signal emitted by the sea ice should be small. The flight leg corresponding to Figure 4.25 is indicated in Figure 4.24.

Figure 4.26 shows a scatter plot of the polarisation ratio  $P$  versus the gradient ratio  $G$ . Each point represents an average of 250 samples. The clusters refer to different surface types which have been classified by visual observations. A discrimination of first year and young ice seems to be difficult.

In order to derive the microwave emissivity of different sea ice types from satellite data, the physical temperature of the sea ice and the atmospheric conditions have to be considered. The surface temperature can be derived from thermal infrared sensors, e.g. AVHRR or OLS. The total water vapour content is available from the atmospheric sounder SSM/T2 (Miao, 1997). Information on different sea ice types could be obtained from presently classified ERS-2 SAR images (Bochert, 1996). The results can then be used for a better understanding of the spaceborn passive microwave signal, in terms of the higher resolved aircraft measurement and sea ice properties as observed with ERS-2 SAR.



**Figure 4.24:** Two ERS-2 SAR images (orbit 15380, frame 1935, 12:52 UTC and orbit 15384, frame 1647, 19:31 UTC on March 30th). The white line marks the flight track of Polar 4 (14:56 UTC to 17:56 UTC). Five photographs taken during this flight (at a level of about 600 m) show typical ice structures: **1:** ice edge **2:** first year ice and dark nilas **3:** grey ice **4:** thin first year ice broken by the swell **5:** small pancake ice.



**Figure 4.25:** Time series of the radiometer flight mission on March 30. The time series cover a period of 45 min (17:12 to 17:47 UTC), which is equivalent to a distance of 165 km (point A to B in Figure 4.24).

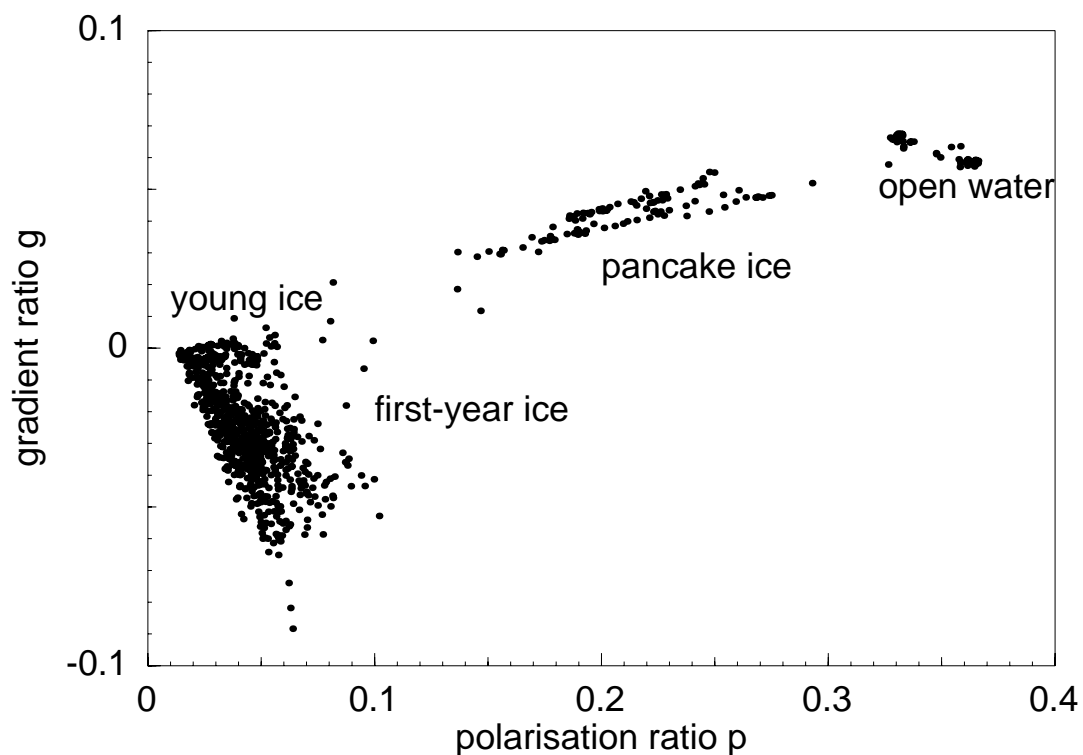


**Figure 4.26:** Scatter plot of the polarisation ratio  $P$  and the gradient ratio  $G$ .

#### 4.8. Low-level atmospheric structure and surface radiation at Ny-Ålesund

During the field experiment most of the time forced convection due to the presence of strong winds or stable stratified layers was observed at Ny-Ålesund. In Figure 4.27 the wind speed measured by the Sodar at a height of 90 m is shown. In Figure 4.28 wind speed as a function of the wind direction is given. Most of the time the wind was observed from SE and NW; from these two sectors also the strongest wind velocities occurred. The data presented here refer primarily to April 7 as an example. Similar graphs are available on a CD-ROM (the date and time being given in Table 3.3 for all the field experiment period).

##### 4.8.1. Sodar and tethersonde data

On 7 April, the meteorological situation was characterised by increasing pressure and temperature during the day, clear sky, low humidity and low wind speed. During all day the Sodar facsimile shows thermal stratifications with several layers superimposed (top of Figure 4.29) up to 900 meters. At the interface of each layer

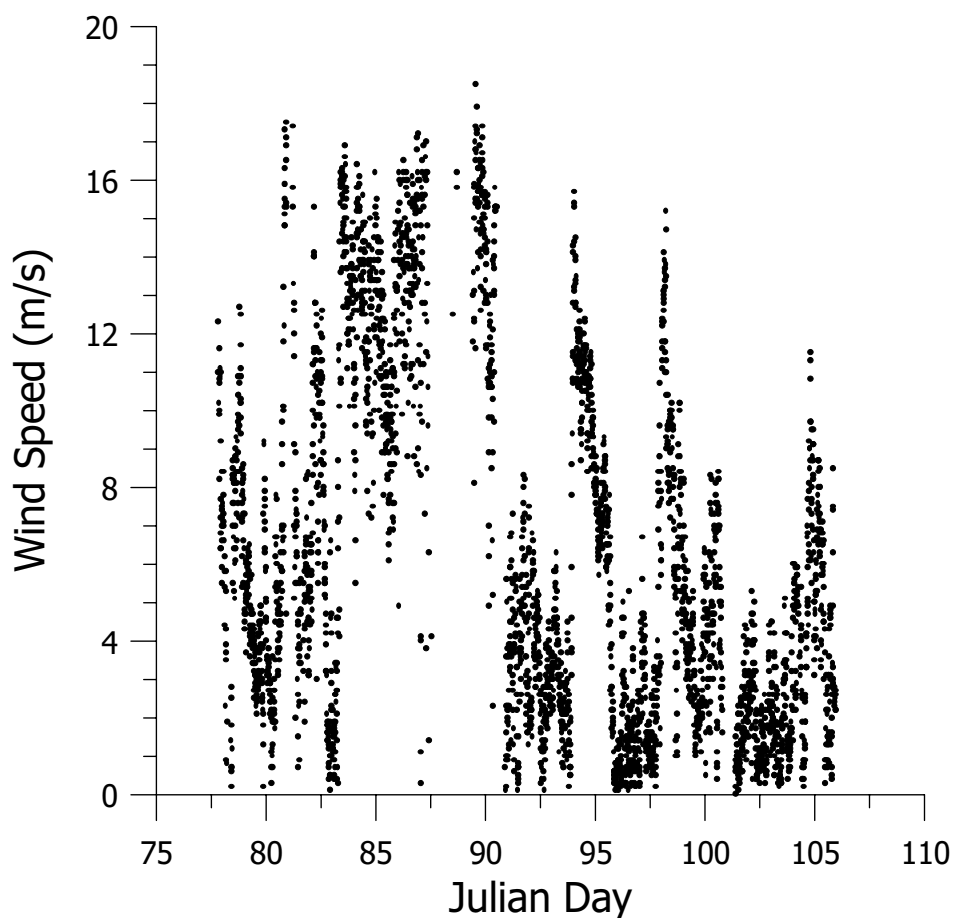


**Figure 4.27:** Wind speed measured by the Sodar at Ny-Ålesund at 90 m height. 15 March is julian day 74 and 16 April is julian day 106.

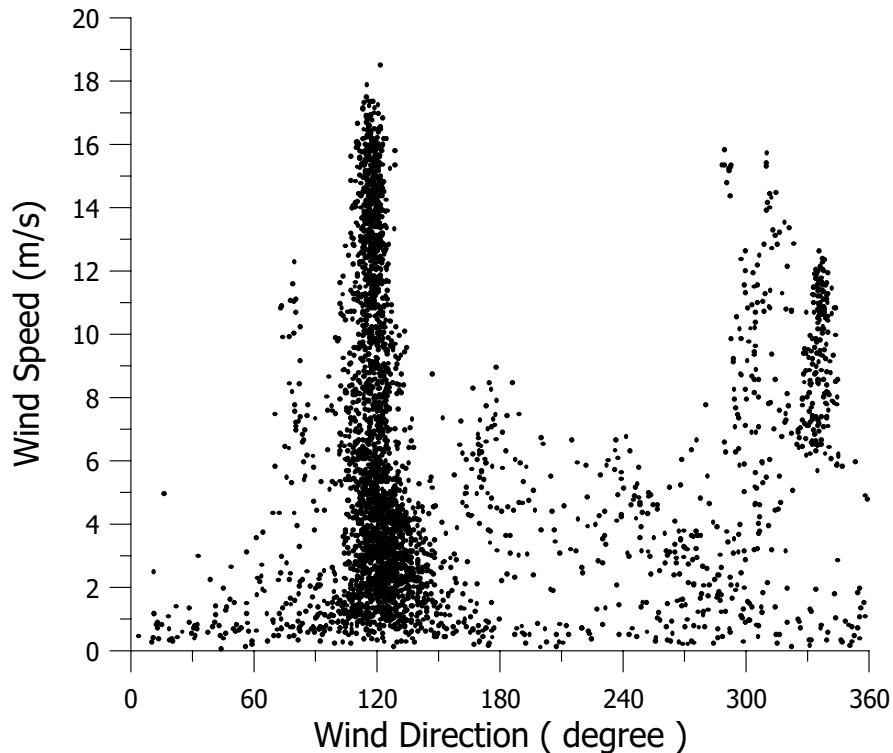


**Figure 4.28:** Wind speed versus wind direction scatter diagram measured by the Sodar.

oscillations due to mechanical instabilities are visible. The vertical velocity field is shown in the same graph (bottom of Figure 4.29). In this figure a vertical velocity of 2 m/s covers the distance between two range gates. The black band around 20:30 is due to the presence of strong noise in the near proximity of the Sodar; at this time some values are not available in the vertical velocity graph due to a low signal-to-noise ratio.

The time evolution of the horizontal wind velocity is shown in Figure 4.30. The normalisation of the wind vector (3 m/s corresponds to a vector of the same length given in the figure) as well as the direction is given in the same figure. A rotation of the wind from South-East to North-East occurs along the vertical, probably because of the orography with a minimum of the wind speed at 600 m. Stronger winds (10 m/s) as well mechanical mixing due to forced convection occur starting from 22:00 Solar Time.

In Figure 4.31 the humidity and temperature ascent profiles are shown (top of Figure 4.31) as well as the wind speed and direction ascent profiles (bottom of Figure 4.31) at 7:54, 10:01, 11:15, 11:50, 12:55 and 15:42, obtained with the tether sonde. A lapse rate in the temperature profile associated with a sharp decrease in the humidity is visible.

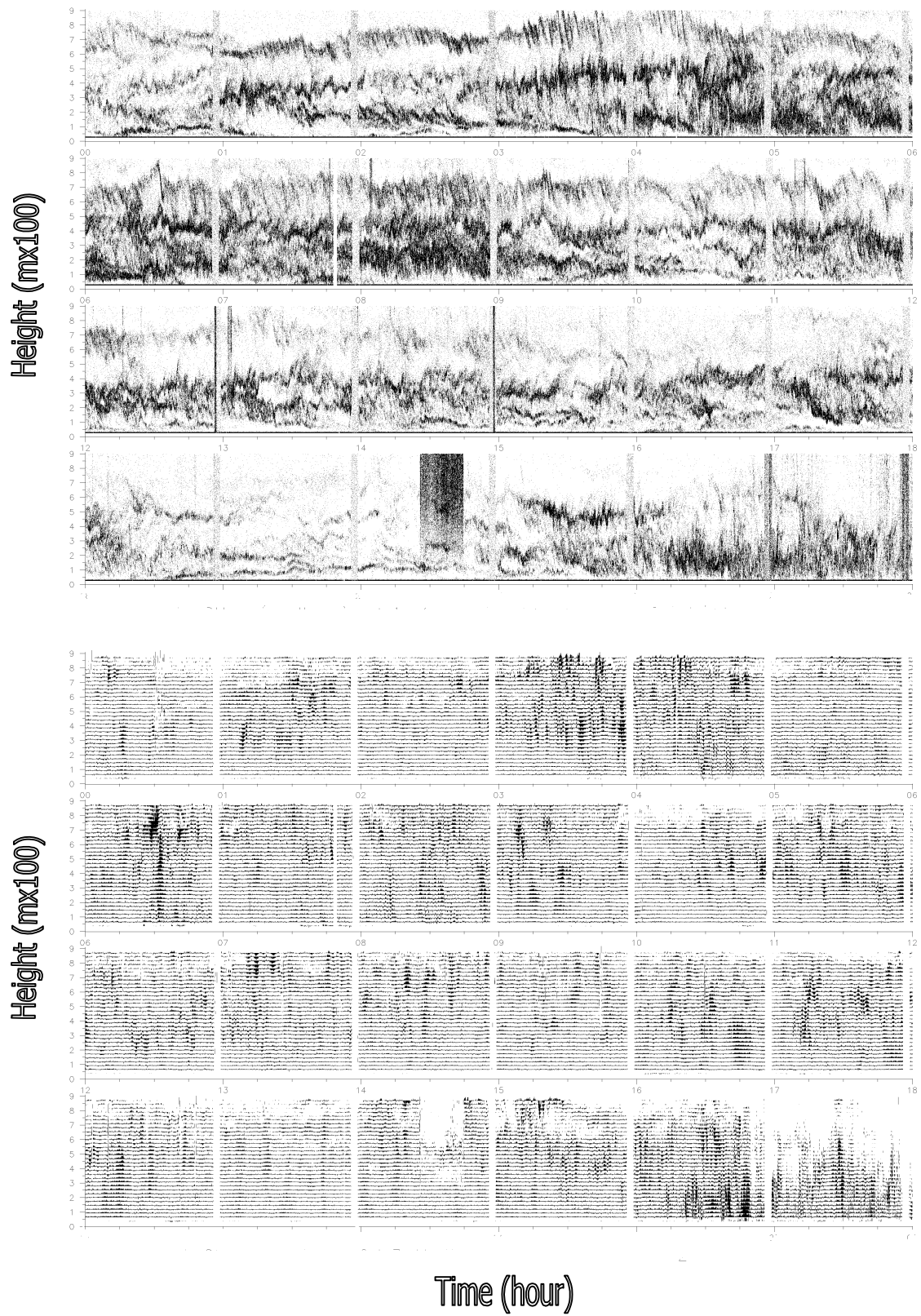


**Figure 4.29:** Sodar facsimile recorded at Ny-Ålesund on 7 April, 1998 (top figure), and vertical velocity (bottom figure) between 00:00 and 24:00 ST.

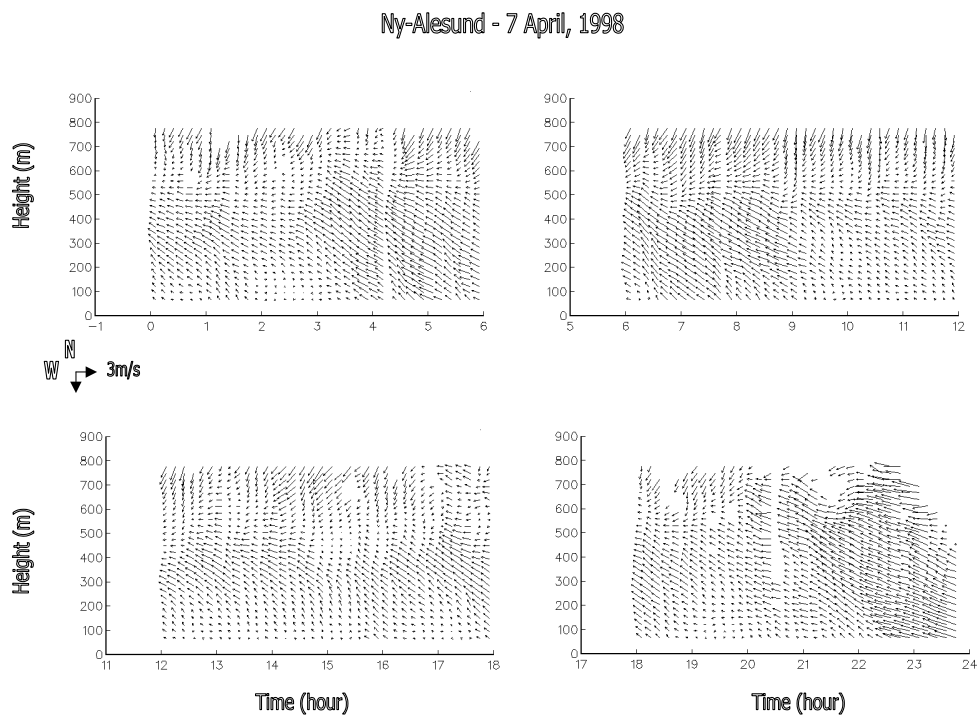


**Figure 4.30:** The wind field recorded at Ny-Ålesund on 7 April, 1998.

#### 4.8.2. Radiation Data

Some interesting patterns of the radiation fluxes are well evident in the preliminary analysis (Figure 4.32). The varying cloud coverage is distinctly reflected in the long and short wave radiation. As a consequence, the net-radiation at the surface even changes sign. While under almost clear sky condition the net radiation is negative during the day, under overcast conditions it is close to zero day and night. This behaviour will also be mirrored in the turbulent fluxes which will be available in due time.

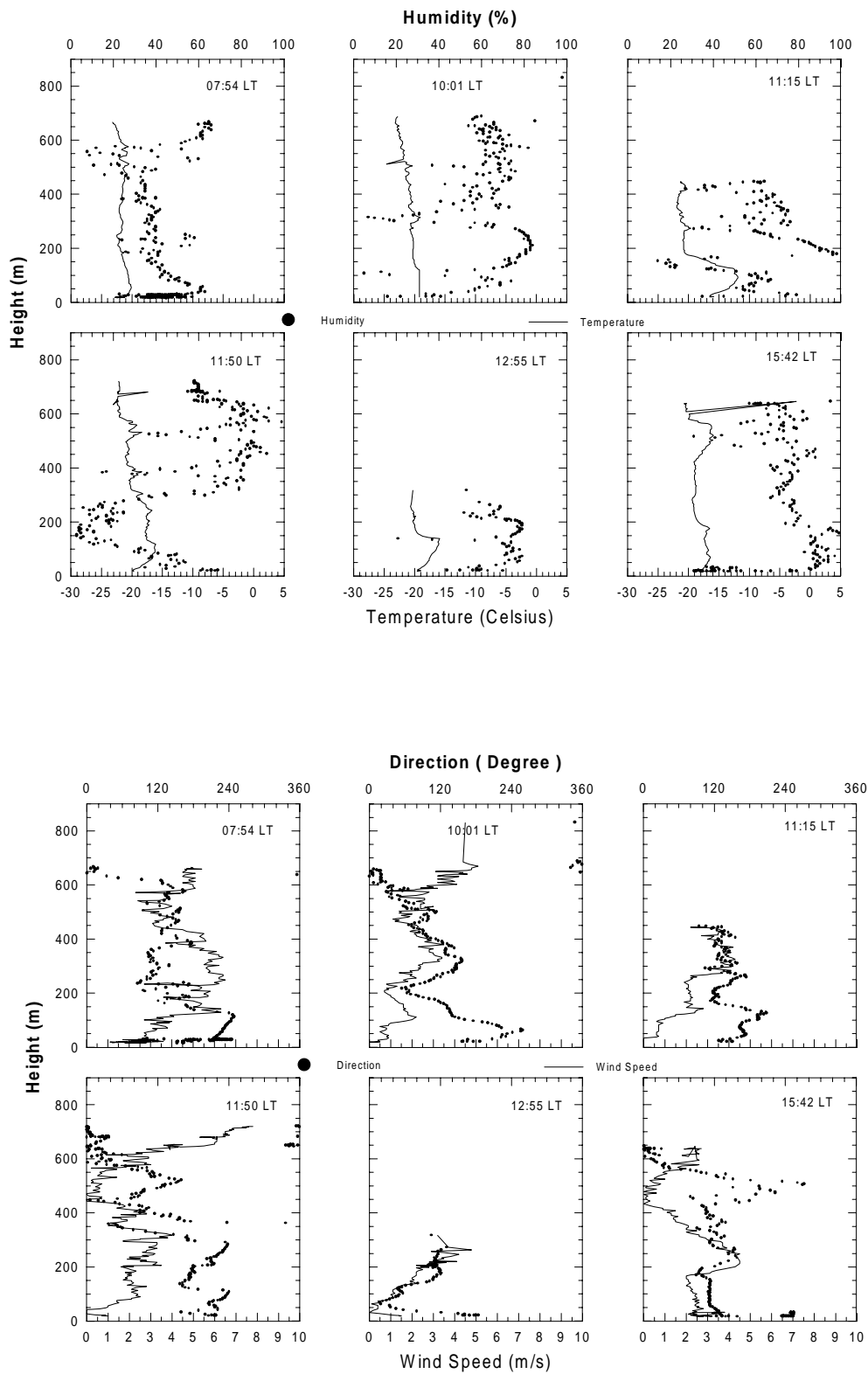


**Figure 4.31:** Tethersonde ascent profiles of humidity and temperature (top) wind and direction (bottom) recorded at Ny-Ålesund on 7 April, 1998.

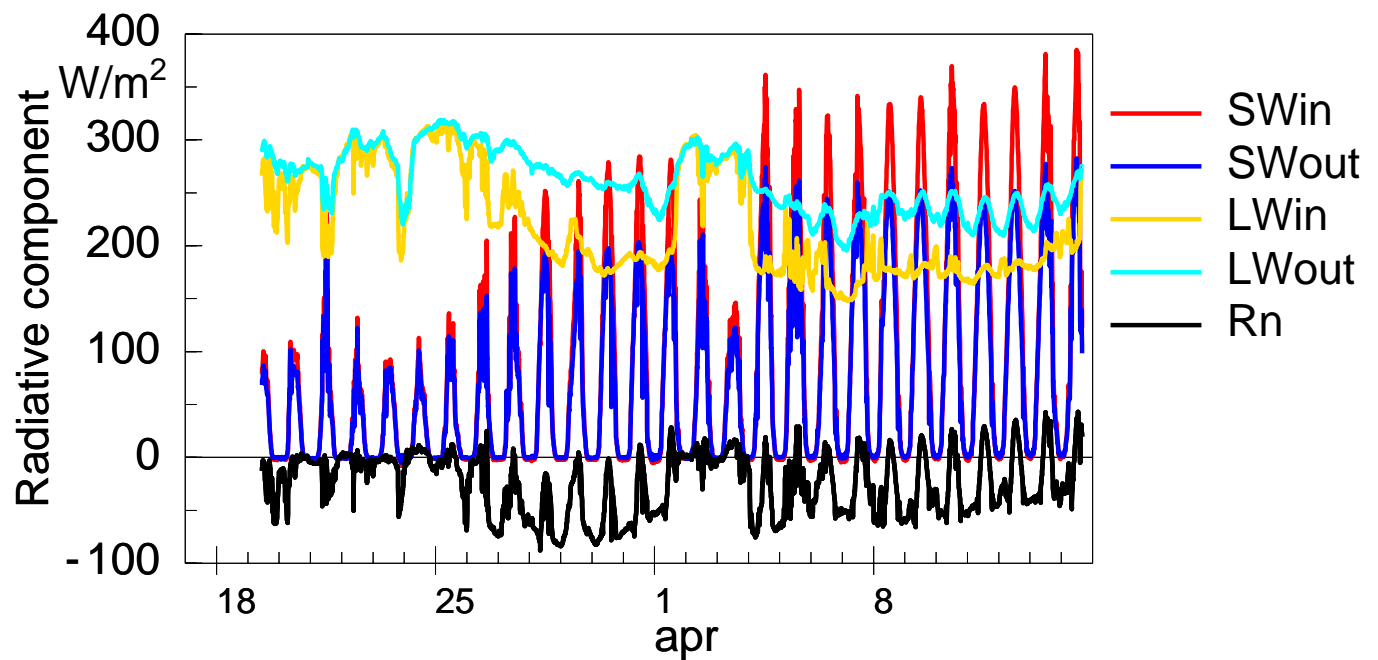


**Figure 4.32:** Radiation components collected during the entire ARTIST field experiment (SWin = short wave incoming, SWout = short wave outgoing, Lwin = long wave incoming, LWout = long wave outgoing, Rn = net radiation).

## 5. References

- Argentini, S., Mastrantonio G., Fiocco G. and Ocone R., 1992: Complexity of the wind field as observed by a Sodar system and by automatic weather stations on the Nansen Ice Sheet, Antarctica, during summer 1988- 89: two cases studies. *Tellus* **44 B**, 422–429.
- Argentini, S., Mastrantonio G., 1994: Barrier winds recorded during two summer campaigns and their interaction with the katabatic flows as observed by a triaxial Doppler Sodar. *Int. J. Remote Sensing*, **15**, 455–466.
- Baker, M. B. and J. Latham, 1979: The evolution of droplet spectra and the rate of droplet production of embryonic raindrops in small cumulus clouds. *J. Atmos. Sci.*, **36**, 1612–1615.
- Bochert, A., 1996: Klassifikation von Radarsatellitendaten zur Meereisererkennung mit Hilfe von Line-Scanner-Messungen. *Berichte zur Polarforschung*, **209**, Alfred-Wegener-Institut, Bremerhaven.
- Bochert, A. and Wamser, Ch., 1994: New Airborne Line Scanner Systems for High Resolution Sea Ice Observation. *The Global Atmosphere and Ocean System*, **2**, 247–251.
- Bochert, A. and Holzschuher, R., 1995: Einsatz des Color-Line-Scanners. Alfred-Wegener-Institut.
- Brümmer, B., H. Schlünzen and W. Bogel, 1982: Cloud streets during Kontur, *Hamburger Geophys. Einzelschr.*, **57**, 63–77.
- Considine, G. and J. A. Curry, 1998: Effects of entrainment and droplet sedimentation on the microphysical structure of stratus and stratocumulus clouds. *Quart. J. R. Met. Soc.*, **124**, 123–150.
- Freese, D., 1998: Solare und terrestrische Strahlungswechselwirkung zwischen arktischen Eisflächen und Wolken. Diss., Fachbereich Physik, Univ. Bremen.
- Hein, P. F. and R. A. Brown, 1988: Observations of longitudinal roll vortices during Arctic cold air outbreaks, *Boundary Layer Meteorol.*, **45**, 177–199.
- Huschke, R. E. (Ed.), 1989: Glossary of Meteorology, Amer. Meteorol. Soc., Boston, MA, USA, 179 pp.
- Kottmeier, C., 1996: User Handbook for the Polar 2 and Polar 4 research aircraft. Alfred-Wegener-Institut für Polar- und Meeresforschung, Bremerhaven.
- Kottmeier, C., Lüdeman, 1996: Meereisbojen 1986–1995 / Technische Dokumentation. *Berichte aus dem Fachbereich Physik*, **69**, AWI.
- Mastrantonio G., G. Fiocco, 1982: Accuracy of wind velocity determinations with Doppler Sodar. *J. Appl. Meteorol.*, **21**, 820–830.

- Korolev, A. V., 1995: The influence of supersaturation fluctuations on droplet size spectra formation, *J. Atmos. Sci.*, **52**, 3620–3634.
- Korolev, A. V., J. W. Strapp and G. A. Isaac, 1998: The Nevzorov airborne hot wire LWC/TWC probe: Principle of operation and performance characteristics, *J. Atmos. Oceanic Technol.*, in press.
- Martin, T. and S. Bakan, 1991: Airplane investigation of a case of convective cloud bands over the North Sea, *Boundary Layer Meteorol.*, **56**, 359–380.
- Miao, J., et al., 1997: Retrieval of total water vapor in polar regions using SSM/T2 channels. In Proc. IEEE Geosci. and Rem. Sens. Sym. 1997, Singapore.

## 6. Acknowledgements

Professor Christoph Kottmeier has initiated the ARTIST project and due to his efforts it achieved its mature state.

Thanks are due to the aircraft crew for their very careful operations. We also thank the Aerodata engineers for their commitment. At the Longyear airport Arne Tolas provided helpful weather information. We acknowledge the availability of the Norsk Polar Institutt's facilities.

For the Ny-Ålesund operation valuable help was provided by the personnel of the Kings Bay Cool Company.

This project is supported by the EU Climate and Environment Programme under the reference number PL970030. Additional support was provided by the Italian "Progetto Strategico Artico".